Studies of Higher Order Mode Couplers for the Upgraded Travelling Wave Acceleration System in the CERN SPS

Von der Fakultät für Elektrotechnik und Informationstechnik
der Rheinisch-Westfälischen Technischen Hochschule Aachen
zur Erlangung des akademischen Grades eines
Doktors der Ingenieurwissenschaften
genehmigte Dissertation

vorgelegt von

Patrick Krämer, M.Sc.

aus Lippstadt

Berichter: Univ.-Prof. Dr.-Ing. Dirk Heberling
Univ.-Prof. Dr. Jeremy Witzens, Ph.D.
Univ.-Prof. Dr.-Ing. Heino Henke, Technische Universität Berlin

Tag der mündlichen Prüfung: 03. Juli 2020

Diese Dissertation ist auf den Internetseiten der Universitätsbibliothek online verfügbar.

Bibliografische Information der Deutschen Nationalbibliothek
Die Deutsche Nationalbibliothek verzeichnet diese Publikation in der Deutschen Nationalbibliografie; detaillierte bibliografische Daten sind im Internet über https://portal.dnb.de abrufbar.

Patrick Krämer:

Studies of Higher Order Mode Couplers for the Upgraded Travelling Wave Acceleration System in the CERN SPS

1. Auflage, 2020

Gedruckt auf holz- und säurefreiem Papier, 100% chlorfrei gebleicht.

Apprimus Verlag, Aachen, 2020
Wissenschaftsverlag des Instituts für Industriekommunikation und Fachmedien
an der RWTH Aachen
Steinbachstr. 25, 52074 Aachen
Internet: www.apprimus-verlag.de, E-Mail: info@apprimus-verlag.de

Printed in Germany

ISBN 978-3-86359-886-0

D 82 (Diss. RWTH Aachen University, 2020)

Abstract

Future high energy particle physics research based on accelerators requires high beam intensity. Parasitic interaction of the charged particle beam with its environment can deteriorate the beam quality and limit the peak intensity for which safe machine operation can be ensured. The beam induces electromagnetic fields in the accelerator components surrounding it which in turn affect the particle motion and can lead to beam instabilities. This interaction is typically described by the concept of beam coupling impedance.

At CERN, the Large Hadron Collider is at the end of an accelerator chain in which particles are accelerated to ever higher energies in transferring the beam from one accelerator to the next. This pre-accelerator chain is presently upgraded to ensure delivery of the demanding high intensity proton beam required by the Large Hadron Collider in the future. The Super Proton Synchrotron is the last pre-accelerator in the chain and utilises a travelling wave system operating at a fundamental frequency of 200 MHz for acceleration to a proton energy of 450 GeV. The travelling wave structures of this broadband acceleration system are cylindrical waveguides periodically loaded with drift-tubes and stems. One main obstacle for higher beam intensity in the Super Proton Synchrotron is presently a multi-bunch instability which is triggered by higher order standing wave modes around 630 MHz in the accelerating structures. The beam coupling impedance of these modes is already heavily damped by resistive higher order mode couplers, but particle-tracking simulations suggest that additional impedance mitigation by a factor of three in the ideal case can cure the instability for the beam intensity required in the future.

The goal of this thesis is to properly identify and characterise the deteriorating higher order modes and to significantly improve on the present impedance mitigation of these modes. The improvement is achieved most notably by a revision of the existing HOM coupler and a newly developed mitigation technique that consists of subtle changes in the accelerating structure by the introduction of posts which are resonant at 630 MHz. The practical feasibility of the proposed improvements is imperative and the impact on the fundamental accelerating mode must stay within acceptable limits. In this regard, a broad understanding of the acceleration system, which was implemented more than four decades ago, is required and is therefore also developed throughout this thesis. The proposed solutions for achieving the increased damping are developed by theoretical analysis together with electromagnetic simulations and their performance is validated by RF measurements. Measurements are also used to quantify in unprecedented detail the impact of the numerous higher order mode mitigation devices on the available fundamental accelerating voltage. Thus, this thesis represents a significant contribution to the future operation of the Super Proton Synchrotron and to the numerous efforts that ensure the long-term physics performance of the Large Hadron Collider and its experiments at CERN.

Kurzfassung

Für zukünftige Forschungsvorhaben in der Hochenergiephysik mithilfe von Teilchenbeschleunigern werden hohe Strahlintensitäten benötigt. Parasitäre Wechselwirkungen zwischen dem geladenen Teilchenstrahl und den einzelnen Komponenten der Beschleuniger können die Qualität des Strahls verschlechtern und die maximal erreichbare Intensität, für die ein sicherer Betrieb des Beschleunigers gewährleistet werden kann, limitieren. Der Strahl induziert elektromagnetische Felder in den Beschleunigerkomponenten, die wiederum auf die Flugbahn der Teilchen rückwirken und zu Strahl-Instabilitäten führen können. Diese Wechselwirkungen werden üblicherweise durch das Konzept der Strahl-Kopplungs-Impedanz beschrieben.

Der Large Hadron Collider am CERN steht am Ende einer Kette von Vorbeschleunigern, in der die Energie der Teilchen schrittweise erhöht wird. Diese Vorbeschleuniger werden derzeit umgebaut, um die Bereitstellung des zukünftig benötigten Teilchenstrahls hoher Intensität gewährleisten zu können. Das Super Proton Synchrotron ist das letzte Glied in der Vorbeschleunigerkette und verwendet zur Teilchenbeschleunigung ein Wanderwellensystem, das bei einer Frequenz von 200 MHz betrieben wird und Protonen auf eine Energie von 450 GeV beschleunigt. Die Wanderwellenstrukturen dieses breitbandigen Beschleunigungssystems bestehen aus Rundhohlleitern, die mit Driftröhren und zylindrischen Stämmen periodisch belastet sind. Der Strahl besteht üblicherweise aus einer hohen Anzahl an Teilchenpaketen, in denen jeweils um die hundert Billionen Teilchen gebündelt sind. Das größte Hindernis für die höhere Strahlintensität im Super Proton Synchrotron ist zurzeit eine Instabilität, die durch die Interaktion aufeinander folgender Teilchenpakete hervorgerufen wird und deren Ursprung in den induzierten elektromagnetischen Feldern höherer Moden um 630 MHz in den Wanderwellenstrukturen liegt. Diese Strahl-Kopplungs-Impedanz wird durch Stehwellen hervorgerufen und konnte durch vorhandene Koaxialkoppler bereits erheblich gedämpft werden. Simulationen von Teilchen-Flugbahnen legen jedoch nahe, dass eine zusätzliche Impedanz-Reduktion idealerweise um einen weiteren Faktor drei dieser Stehwellen benötigt wird, um die Instabilität bei der zukünftig gewünschten Intensität zu verhindern.

Das Ziel dieser Dissertation ist es, die in Frage kommenden höheren Moden genau zu identifizieren, zu charakterisieren und die bereits vorhandene Dämpfung dieser Moden erheblich zu verbessern. Die Dämpfungsverbesserung wird vor allem durch eine Optimierung des existierenden Kopplers und eine neuartige Unterdrückung der höheren Moden durch den Einsatz resonanter Stifte erreicht. Die Realisierbarkeit der vorgeschlagenen Lösungen in der Praxis muss dabei gewährleistet werden und eine möglicherweise negative Beeinflussung der beschleunigenden Fundamental-Mode muss in akzeptablen Grenzen bleiben. Das dabei erforderliche breite Verständnis des vor fünf Jahrzehnten entwickelten Beschleunigungssystems wird im Laufe der Dissertation ebenfalls erarbeitet. Die vorgeschlagenen Lösungen für das Erreichen der höheren Dämpfung wer-

den aus Theorie und Simulation entwickelt und ihre Wirksamkeit mit Hilfe von HF-Messungen bestätigt. Mittels dieser Messungen wird auch der Einfluss der Koppler auf die von dem System erzeugte Beschleunigungsspannung in nie dagewesenem Detail quantifiziert. Die vorliegende Dissertation liefert somit einen bedeutsamen Beitrag für den zukünftigen Betrieb des Super Proton Synchrotron und für die zahlreichen weiteren Anstrengungen, die die Leistungsfähigkeit des Large Hadron Colliders und dessen Experimente am CERN zukünftig sicherstellen.

Acknowledgements

First and foremost, my heartfelt gratitude goes to Christine Völlinger at CERN for offering me this unique doctorate opportunity and for her continuous supervision over the last years. Her advice and guidance as well as her authenticity and reliability gave me the support I required to push through discouragements and external odds. Thank you also for providing me with the opportunity to attend numerous conferences, workshops and CERN schools to further extend my technical and personal horizons.

I thank Prof. Dirk Heberling for taking charge of my supervision at RWTH Aachen University and for his sincere advice throughout these last years. His foresight and experience in both technical and organisational aspects of a doctorate eased my work immensely. I also thank him for his patience with the recurring CERN bureaucracy and for all his organisational efforts regarding my doctoral defence. I am also very grateful to Prof. Heino Henke for kindly accepting to evaluate my thesis as well as for his technical input and for inviting me to TU Berlin to present my research work. Furthermore, I thank Prof. Jeremy Witzens and all members of the jury for reporting on my dissertation.

I give a big thanks to my present and former colleagues of the BE-RF-BR section at CERN: Most notably to Aaron Farricker, Branko Popovic and Thomas Kaltenbacher for our countless technical discussions and their helpful advice. I equally thank Joël Repond and Alexandre Lasheen for their explanations on the SPS beam dynamics and for their patience while letting me practice my French with them. My sincere gratitude goes also to Thomas Bohl for his willingness to share his vast technical and personal experience with me on numerous occasions.

I am also grateful to Eric Montesinos and the whole team of BE-RF-PM for preparing the SPS accelerating structures numerous times for RF measurements. I address an equally big 'thank you' to the development team of ACE3P at SLAC with in particular Oleksiy Kononenko for their support on the simulation code. At last, but not least, I want to apologise to my family and friends whom I have often neglected over these last years. I will make amends.

This work has been sponsored by the Wolfgang Gentner Programme of the German Federal Ministry of Education and Research (grant no. 05E15CHA) and used resources of the National Energy Research Scientific Computing Center, a DOE Office of Science User Facility supported by the Office of Science of the U.S. Department of Energy under Contract No. DE-AC02-05CH11231.

Geneva, October 2019 Patrick Krämer

Contents

Abstract

Kurzfassung

Acknowledgements

Acronyms iii

1. Introduction 1
1.1. Particle Acceleration in Periodic Structures 2
1.2. Particle Acceleration in Synchrotrons 12
1.3. The CERN Accelerator Complex 15
1.4. High-Luminosity LHC and LHC Injector Upgrade Projects 18
1.5. Thesis Motivation, Goals and Organisation 22

2. Wakefields and Impedances 25
2.1. Longitudinal Wake Function and Wake Potential 25
2.2. Longitudinal Beam Coupling Impedance 27
2.3. Impedance of Standing Wave Resonators 28
2.4. Impedances of Travelling Wave Structures 32

3. The SPS 200 MHz Parallel Stem Acceleration System 37
3.1. Choice of Travelling Wave Operation for Particle Acceleration 37
3.2. Multi-Stem Drift Tube Structures and Transverse Stem (TS) Resonances 39
3.3. System Overview 42
3.3.1. Brief Overview on Present HOM couplers 45
3.4. Unit-Cell Simulations 46
3.4.1. Dispersion in the 200 MHz FPB and TS_{11}-Mode Field Profiles 46
3.4.2. Impedance Calculation in the FPB of 33-, 44- and 55-Cells 48
3.4.3. TS_{31}-HOM Dispersion Around 630 MHz 50
3.5. Tuning 53
3.5.1. Frequency Dependence on Pressure and Temperature 55
3.6. Matching 55
3.6.1. Consequences of RF Generator and Load Mismatch 55
3.6.2. A Direct Matching Technique for Travelling-Wave Operation 57
3.7. Preface to EM Simulations with CST and ACE3P 59
3.7.1. Wakefield Simulation of Longitudinal Beam Coupling Impedance 60

3.7.2. Implementation of a Lossy Perfectly Matched Layer for the Simulation of Resistive Loads . . . 63
3.8. Simulation of the 33-Cell Structure . . . 65
3.8.1. Matching of the FPB and Calculation of Its Peak Forward Impedance . . 65
3.8.2. Beam Coupling Impedance of the TS_{11} FPB . . . 69
3.8.3. Beam Coupling Impedance of HOMs and Performance Analysis of the TS_{31} HOM Damping Scheme Used Until Long Shutdown 2 . . . 69

4. Improvement of TS_{31} HOM Mitigation in the Future 33-Cell Structures 73
4.1. Analysis of TS_{31} HOMs in 11- and 33-Cells . . . 73
4.2. Additional HOM Couplers for Increased Damping of TS_{31} Modes . . . 78
4.3. Improved HOM Coupler for Increased Damping of High-R/Q TS_{31} Modes . . . 80
4.4. Constraints on HOM Impedance Mitigation . . . 89
4.5. Resonant Posts for HOM Impedance Mitigation . . . 91
4.5.1. Multi-Physics Considerations of Resonant Posts . . . 96

5. RF Measurements on the Parallel Stem Structure 103
5.1. Resonant Perturbation Measurements of Axial Electric Field . . . 103
5.1.1. Perturbation Theory . . . 103
5.1.2. Some Practical Considerations . . . 104
5.2. Verification of Simulation Models and Evaluation of the Three Available 11-Cell Spare Sections . . . 106
5.3. Verification of 25 Ω-Equivalent Complex Impedance Loads . . . 109
5.4. Verification of Resonant Posts . . . 114
5.5. Measurement of Transit Time Factor of Travelling Wave Structures . . . 115
5.5.1. Theory . . . 116
5.5.2. Application to the TWSs in Use Until Long Shutdown 2 in the SPS . . . 117
5.6. Impact of HOM Couplers and Resonant Posts on the Accelerating Passband . . . 119

6. Conclusions and Outlook 123

A. Some Details on Travelling Wave Structures 125

B. Equivalent Circuit and Dispersion Relation for Multi-Stem Drift Tube Structures 129

C. Electromagnetic Field Profiles of Modes of Interest 133

D. Performance of 25 Ω-Equivalent Complex Impedance Loads on 44-Cells 137

E. Temperature Distribution in the SPS TWS for an Input Power of 1.6 MW 139

Bibliography 141

List of author's publications 149

Acronyms

ABC absorbing boundary condition

ACE3P Advanced Computational Electromagnetic 3D Parallel Simulation Suite

BLonD Beam Longitudinal Dynamics code

CERN European Organisation for Nuclear Research

CST Microwave & Particle Studio suite of Computer Simulation Technology company

EM electromagnetic

FDTD finite-difference time-domain

FEM finite-element method

FPB fundamental passband

FPC fundamental power coupler

HL-LHC High-Luminosity LHC

HOM higher order mode

LHC Large Hadron Collider

LINAC linear accelerator

LIU LHC injectors upgrade

LS long shutdown

NERSC National Energy Research Scientific Computing Center

OFHC oxygen-free high-conductivity

PML perfectly matched layer

PS Proton Synchrotron

PSB Proton Synchrotron Booster

RF radio-frequency

SCM simultaneous complex conjugate matching

SPS Super Proton Synchrotron

TE transverse electric

TM transverse magnetic

TS transverse stem

TTF transit time factor

TWS travelling wave structure

VNA Vector Network Analyser

VPP vacuum pumping port

1. Introduction

Particle physics research aims at understanding the fundamental constituents of matter and the natural processes behind radiation. For such studies, ordinary optical microscopes are insufficient as their resolution is limited by the wavelength of visible light. Electron microscopes therefore use a beam of accelerated electrons which have wavelengths shorter by several orders of magnitude. The electron beam is shot on a material sample to achieve resolutions of a fraction of a nanometre. Equally important as the resolution is the creation of new, often short-lived particles, and the required energy to obtain these follows directly from Einstein's equation $E = mc^2$. This is why particle accelerators and colliders such as the Large Hadron Collider (LHC) operated by CERN are used in particle physics. Here, the properties of composite particles like e.g. protons accelerated to high kinetic energy are probed by a second beam in collisions leading not only to extraordinary resolution but also to the creation of new particles of interest. The hadrons decompose into their constituents which are then observed in particle detectors. The collisions create conditions which prevailed only in a very short time after the 'big bang' which makes the experiments also interesting for astrophysics. The collision energy thereby determines which nuclear physics events of interest will occur. The energy spread in hadron collisions is large, which is why hadron colliders are primarily used to discover new physics events and its energy should therefore be as high as possible. Elementary particle (e.g. electron or positron) colliders can be used to make more precise measurements in a well defined energy range.

The highest achievable energy of circular proton accelerators is nowadays limited by the magnetic field strength of superconducting dipole magnets used to keep the particles on their circular trajectory. Until stronger magnet technology is available, this limitation could only be circumvented by increasing the machine radius thereby effectively decreasing the required magnetic bending strength. Fundamental particle research led to the discovery of radioactivity and subsequently alpha, beta, gamma and X rays as well as many new particles that are the fundamental building blocks of nature. Today, the applications for particle accelerators are manifold. Not only are they used in particle physics, but e.g. also in oncotherapy or for ion implantation during manufacture of semiconductors.

The acronym CERN is derived from the french name 'Conseil Européen pour la Recherche Nucléaire' (European Council for Nuclear Research). This provisional council was established in 1952 by 12 European countries with the task to build a fundamental physics research laboratory in Europe [1]. As European research lay idle after the second world war, a further intent was to unite European scientists and to share the ever rising costs for nuclear physics research. The laboratory was finally founded in 1954 under the name European Organization for Nuclear Research and although the council was dissolved, the acronym CERN was kept as the name for the laboratory.

A suburb north-west of Geneva, Switzerland was chosen for the main site of the organisation. The primary purpose of the laboratory is the study of the basic constituents of matter and the forces acting between them. Over the years numerous scientific achievements were accomplished at CERN like the discovery of rare pion decays in 1958, the W and Z bosons in 1983 and the Higgs boson in 2012 but also the invention of the World Wide Web in the late 1980s.

1.1. Particle Acceleration in Periodic Structures

Charged particles obey Lorentz' force law in electromagnetic fields. Accordingly, magnetic fields can be used only for deflection of moving particles whereas for acceleration or deceleration electric fields are used. The first particle accelerators used constant electric fields between two electrodes. The achievable particle energy in this type of accelerator is directly proportional to the maximum voltage that can be applied to the electrodes. It is limited to only a few MV due to corona formation at the electrodes leading to voltage breakdown [2].

This problem was first overcome by applying a high frequency alternating voltage that can be described as $V(t) = V_{max} \sin(\omega t)$ of a single source between several electrodes arranged in series. However, an overall more complicated accelerator design is needed to prevent the particles from being decelerated during the negative half-wave of the radio-frequency (RF) system, see Fig. 1.1. The vacuum vessel around the beam path, mandatory in all particle accelerators to avoid collisions with residual gas molecules, is not shown. The first particle accelerator ever to use this principle was constructed by the Norwegian PhD student R. Wideröe at RWTH Aachen University in 1927 [3]. Subsequent electrodes, so-called drift tubes, through which the particles travel are

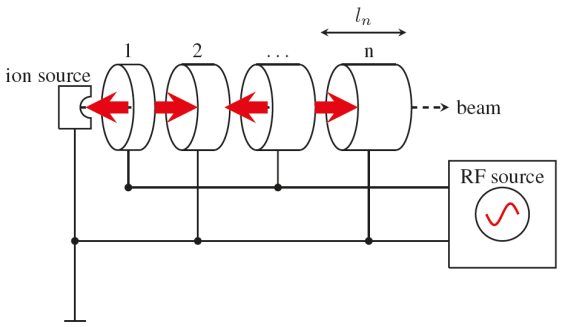

Figure 1.1.: Principle and electric field profile of Wideröe's RF linear accelerator [3, 4].

connected to opposite polarities of an RF source. While a particle moves from one gap between two consecutive drift tubes to the next, the polarity of the RF source changes, so that particles always see an accelerating field in the gaps. High power RF sources are usually quite bandlimited. Assuming therefore a constant frequency for the RF source, the drift tube lengths need to increase

with larger particle velocity so that the particles stay shielded during the decelerating half-wave of the accelerating voltage. After the n-th drift tube the particles of charge q reach the energy

$$U_n = nqV_{max}\sin(\Phi_s), \tag{1.1}$$

where Φ_s is the average phase of the RF voltage the particles undergo during their transit of the gaps [2]. The important point is that to reach the energy U_n no larger voltage than V_{max} is required so that the problem of voltage breakdown like in electrostatic accelerators can be avoided. It is therefore in principle possible to achieve arbitrarily high particle energies with such RF linear accelerators (LINACs) of sufficient length.

As a secondary effect of acceleration with RF fields, a constant stream of particles is chopped into several particle packages, so-called bunches. Consider Fig. 1.2 in which the time-dependence of the RF voltage in the gaps between two consecutive drift tubes is shown. Counter intuitively, the

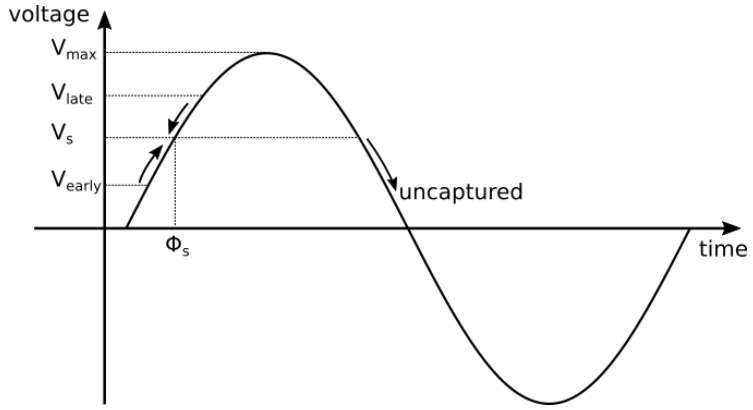

Figure 1.2.: Time dependence of accelerating voltage between two drift tubes demonstrating automatic longitudinal phase focusing of particles accelerated on the rising edge.

voltage should not be phased in such a way that an ideal particle - the synchronous particle with the design velocity of the accelerator - sees the crest of the voltage V_{max} during its traversal of each gap. In this case already small, in practice unavoidable deviations from the nominal time of arrival in a gap would result in particle velocities that do not match the design velocity in subsequent gaps. As an example, consider a particle arriving slightly later compared to the synchronous one at the crest of the RF voltage. This particle experiences a smaller accelerating voltage and will arrive even later in the next gap. Such particles will therefore be out of synchronism with the RF accelerating field and not be accelerated to maximum energy. On the other hand, an off-crest acceleration at a design phase Φ_s on the rising edge of the RF voltage as shown in Fig. 1.2 leads to an automatic re-synchronisation of the particle arriving later in the gap. This principle is also denoted by phase focusing. In this case, the late particle is subject to a larger voltage in the gap in comparison to the ideal particle arriving at the synchronous phase. A particle that underwent a too large voltage

in the preceding gaps and which therefore arrives early sees a smaller voltage leading overall to a bunching of the particles around the synchronous phase[1].

The maximum particle energy achievable in a Wideröe LINAC is in practice limited by the two following effects. The distance between gaps and the drift tube lengths must increase with energy to keep the particles synchronous with the RF source. The maximum possible dimensions of the machine would therefore always set the top energy limit. At first glance this problem could be circumvented by the use of higher frequencies. However, as the accelerator is not enclosed by an electric boundary, the drift tubes would act like antennas as soon as their dimensions are on the order of the RF wavelength. The power of the RF source would therefore be radiated instead of used for acceleration leading to a poor efficiency of the accelerator [4].

This problem was solved by L. Alvarez who enclosed the Wideröe LINAC by a conducting cylinder as outlined in Fig. 1.3 [5]. On the downside, now also resonant effects in the surrounding

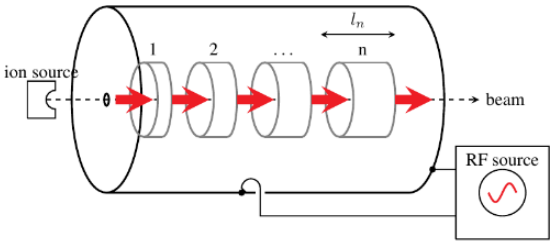

Figure 1.3.: Principle and electric field profile of an Alvarez LINAC [4, 5].

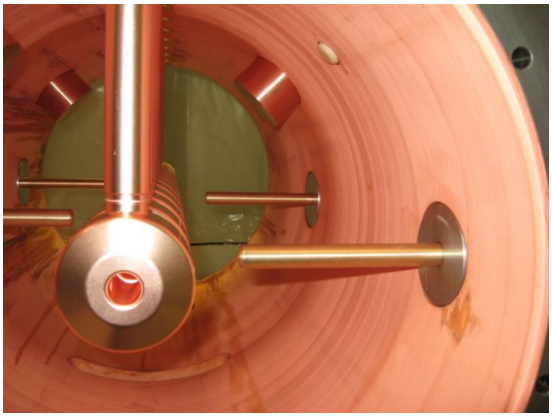

Figure 1.4.: Prototype of the Alvarez drift tube LINAC of CERN's LINAC 4 [6]. The drift tubes are suspended at the top by stems. Horizontal post-couplers for field stabilization [7] and tuning plungers are also shown.

cylinder have to be taken into account making the design more difficult. The resonant frequency of each gap now depends on the diameter of the outer cylinder and drift tubes as well as the distance between them. While for the Wideröe LINAC the RF phase of the accelerating electric field changes from gap to gap by π, the fields in the Alvarez LINAC all point in the forward direction corresponding to zero phase shift, consider Figs. 1.1 and 1.3. This is the resonance with the lowest frequency possible in the cylinder and it is called the 0-mode. So, for synchronism with the RF source, the phase needs to progress by 2π while the particles travel from one gap to the next.

[1]For acceleration above transition energy (refer to footnote[3]) in a circular accelerator the synchronous phase must be chosen on the falling edge of the time-dependence to ensure longitudinal phase focusing.

The Alvarez LINAC proved that particle acceleration is possible with resonant RF cavities and this still is the main principle of particle acceleration today. An example for a recent Alvarez structure is the drift tube LINAC of CERN's LINAC 4 inaugurated in May 2017 which is shown in Fig. 1.4. To gain some insight into the design and behaviour of such accelerating structures, some fundamental theory is discussed in the following. For brevity, the treatment is constrained to the case of high energy accelerators with quasi-constant particle velocities and therefore structures with exact periodicity.

Let us first look at wave propagation in the unloaded, circular cylinder itself surrounding an Alvarez type structure. This corresponds to wave propagation in an unperturbed waveguide with constant circular cross-section. The dispersion relation for a lossless cylindrical waveguide reads [8, 9]

$$\omega^2 = c^2 \, (k_z^2 + k_c^2). \tag{1.2}$$

Here, k_z is the wavenumber of a mode at angular frequency ω propagating in z-direction in the cylindrical guide with cutoff wavenumber k_c for this mode and c the speed of light in free space. The guide wavelength λ_g is defined as

$$\lambda_g = \frac{2\pi}{k_z} = \frac{\lambda}{\sqrt{1 - \left(\frac{\lambda}{\lambda_c}\right)^2}} \tag{1.3}$$

where λ is the free space wavelength and λ_c the cutoff wavelength. At the cutoff frequency the wavelength in the guide becomes infinitely long and wave propagation is not possible. For very high frequencies the guide wavelength approaches the free space wavelength. The phase velocity v_p of the wave is defined as

$$v_p = \frac{\omega}{k_z}. \tag{1.4}$$

The cutoff frequency of a specific type of mode depends on its field profile as well as the radius of the circular guide and can be calculated analytically for circular waveguides [9]. It is very useful to visualise Eq. (1.2) in the so-called Brillouin or dispersion diagram as in Fig. 1.5. The slope of a straight line drawn from the origin ($k_z = 0, \omega = 0$) to any point on the hyperbola corresponds to the phase velocity of the wave with that specific frequency and wavenumber. The phase velocity of a non-dispersive wave in free space with $v_p = c$ is represented by the bisecting line also called 'light-line'. Note that in a uniform waveguide the phase velocity $v_p = \frac{c}{\sqrt{1-\omega_c^2/\omega^2}}$ is always larger than the speed of light in free space c. However, only modes in the slow wave region below the bisecting line would be useful for particle acceleration. At the cutoff frequency of the mode its wavelength and phase velocity tend towards infinity. The group velocity v_g defined as

$$v_g = \frac{d\omega}{dk_z} \tag{1.5}$$

is zero at cutoff. This means that there is no power transport by the wave at this frequency. Below cutoff the mode decays exponentially and no wave propagation is possible in the guide.

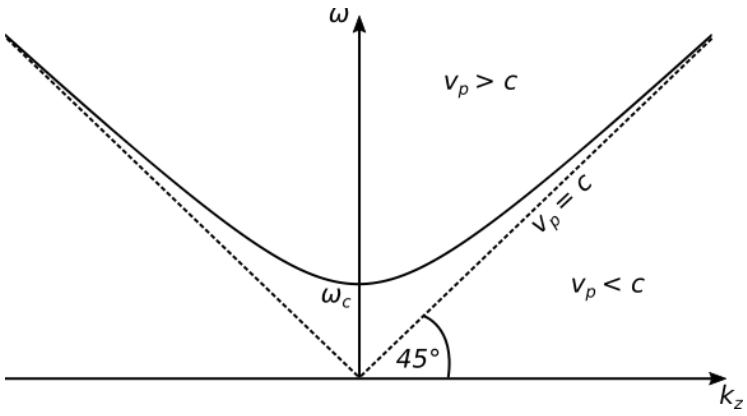

Figure 1.5.: Dispersion diagram for wave propagation in a cylindrical, uniform waveguide for a single mode.

Because the phase velocity in a waveguide is always larger than the speed of light it cannot be used for acceleration as the wave cannot remain synchronous with the particle beam. We will see in the following that by periodically loading a waveguide with electrically reactive obstacles, the phase velocity can be reduced to arbitrarily low values. Physically, this can be explained by the superposition of reflections from the obstacles [10]. In addition to the Alvarez drift tube LINAC, typical examples for periodic structures are the disc loaded structures outlined in Fig. 1.6.

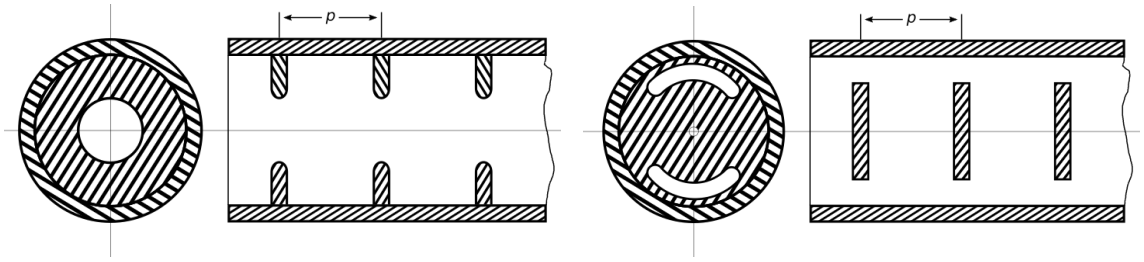

(a) Iris coupled structure.

(b) Slot coupled structure.

Figure 1.6.: Cross-sections of disc loaded periodic structures with periodicity p.

The basis for the study of wave propagation in periodic structures is Floquet's theorem [11]:

In an infinite periodic structure, the fields of a given mode at two different cross-sections separated by one period differ merely by a constant, in general complex factor.

Above theorem results from the fact that when a periodic system of infinite length is displaced along its longitudinal axis z by an integer multiple of periods it coincides with the original structure. We designate the spatial period of the periodically loaded waveguide by p and write the constant factor

in the form $e^{-\gamma_0 p}$ with $\gamma_0 = \alpha_0 + jk_0$. Then, a quite simple function which has Floquet's property is $e^{-\gamma_0 z}$ and the relation between complex electromagnetic (EM) field amplitudes on the two cross sections at z and $z + p$ at distance r from the z-axis is

$$E(r, z + p) = E(r, z)e^{-\gamma_0 p}. \tag{1.6}$$

This is the mathematical formulation of Floquet's theorem. The field distribution function on the transverse cross section $F(r, z)$ must be dependent on z so that we can write the time harmonic field at frequency ω as

$$E(r, z, t) = F(r, z)e^{-\gamma_0 z}e^{j\omega t}. \tag{1.7}$$

$F(r, z)$ has to be a periodic function of z with period p to fulfil Floquet's theorem. Such a periodic function can be expanded into a Fourier series of the form [12]

$$F(r, z) = \sum_{n=-\infty}^{\infty} E_n(r) \exp\left(-jn\frac{2\pi}{p}z\right). \tag{1.8}$$

For a lossless structure in which $\gamma_0 = jk_0$ the field expression in Eq. (1.7) becomes

$$E(r, z, t) = e^{j\omega t} \sum_{n=-\infty}^{\infty} E_n(r)e^{-jk_n z} \tag{1.9}$$

where

$$k_n = k_0 + \frac{2\pi n}{p}. \tag{1.10}$$

Thus, the electric and magnetic fields in a periodically loaded waveguide can be written as a sum of exponentials with appropriate coefficients $E_n(r)$. The n-th travelling-wave of above series is called the n-th space harmonic with a corresponding phase velocity

$$v_{p,n} = \frac{\omega}{k_n} = \frac{\omega}{k_0 + \frac{2\pi n}{p}} \tag{1.11}$$

and choosing n sufficiently large one can obtain an arbitrarily low phase velocity. The group velocity of the n-th space harmonic is

$$v_{g,n} = \frac{d\omega}{dk_n} = \frac{d\omega}{d(k_0 + \frac{2\pi n}{p})} = \frac{d\omega}{dk_0} = v_{g,0}. \tag{1.12}$$

Note that all space harmonics of one mode have the same group velocity but different phase velocities. We can conclude that for a mode to satisfy the periodic boundary conditions of the structure it must consist of the superposition of an infinite number of travelling-wave space harmonics. However, only a single space harmonic, the one with a phase velocity equal to the particle velocity, is useful for particle acceleration. Each harmonic in the Fourier series will have a finite amplitude and will therefore store energy which results in losses in case the accelerator walls have finite conductivity. This is unwanted for particle acceleration so that the accelerator as well as its type of excitation must be designed so that the synchronous space harmonic has an amplitude as large as

possible in comparison to the other space harmonics [10]. The space harmonic $n = 0$ is called the fundamental harmonic.

For the case that γ_0 is purely real, each space harmonic decreases with increasing z, resulting in an evanescent wave. Such waves are inappropriate for particle acceleration and lead to intervals in ω called stopbands, where no wave propagation is possible.

The effect of obstacles like the discs in Fig. 1.6 on the dispersion characteristic of a periodically loaded waveguide was described in great detail by J. Slater [10]. The change of frequency compared to the unperturbed waveguide is negligible over a large range of k_0. Around the frequency ω_π for which $k_0 = \pi/p$ however, the irises are spaced roughly by half a guide wavelength. The reflected waves from successive irises will therefore interfere constructively and bend the dispersion curve of the uniform waveguide as shown in Fig. 1.7a. In fact, the wave with a π-phase shift per period can

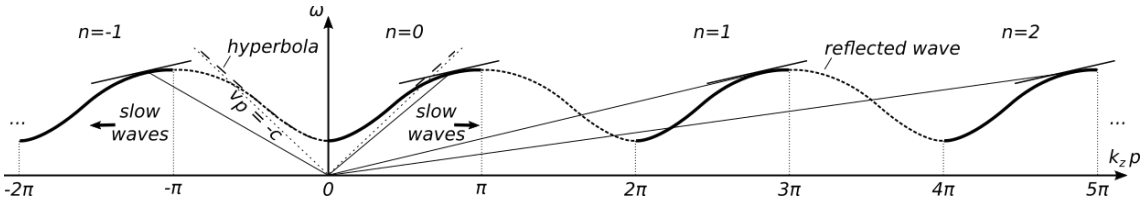

(a) Forward fundamental.

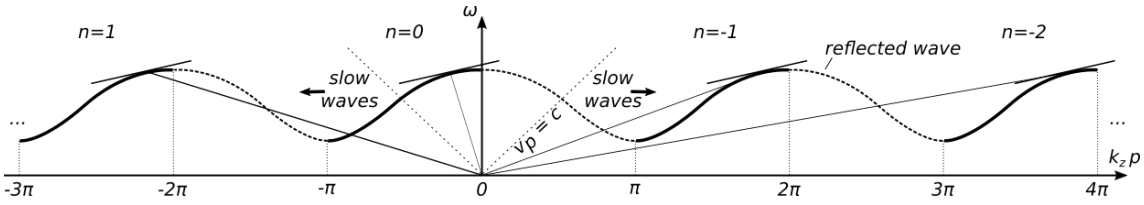

(b) Backward fundamental.

Figure 1.7.: Illustration of dispersion characteristics in periodically loaded waveguides.

not travel through an infinite periodic structure as the reflected wave equals the incident wave. Their superposition results in a standing wave with zero group velocity corresponding to zero slope in the dispersion diagram at $k_z p = \pi$, confirm in Fig. 1.7a. The passband of the mode is therefore bound by its cutoff frequency $\omega_c = \omega_0$ and the π-mode frequency ω_π. In addition, due to the periodic loading of the waveguide and as Eq. (1.10) suggests, the dispersion characteristic of the mode is now periodic. It is constituted by the infinite number of space harmonics with same group but different phase velocity. This is illustrated in Fig. 1.7a as well and waves with group velocity in $-z$-direction are shown dashed. The diagram shows a mode for which phase and group velocity of the fundamental harmonic are of the same sign. For such a mode all space harmonics with positive n are forward waves and all harmonics with negative n are backward waves. For backward waves phase and group velocities run in opposite directions. Depending on the type of periodic obstacles, also modes with a fundamental harmonic of the backward type can exist. The dispersion characteristic of such a backward wave type mode is outlined in Fig. 1.7b. Following

again Eq. (1.10), all space harmonics with positive n are now backward waves as the phase shift per period p is negative.

In uniform as well as in periodically loaded waveguides an unlimited amount of modes is able to propagate at ever higher frequencies. Each one of these will lead to a passband and in the case of the loaded waveguide not all of them must be completely uncoupled from each other. Especially at higher frequencies different modes get mixed up to describe the disturbance in the loaded guide [10]. For passbands that are separated by stopbands from other modes the periodically loaded waveguide has a bandpass characteristic.

The picture described above of a waveguide periodically loaded by obstacles lead to a qualitative description of its dispersion characteristic. However, periodic structures can also be viewed as a chain of coupled resonators and this leads to a more quantitative insight into the various phenomena [13]. The disc loaded structures in Fig. 1.6 for example can be considered as an array of pillbox cavities coupled through the irises or slots respectively. Let us describe the resonators as a periodic chain of identical electrical cells as shown in Fig. 1.8, each with a series impedance Z and a shunt admittance Y. The admittance Y can hereby be attributed to the periodic obstacle. We

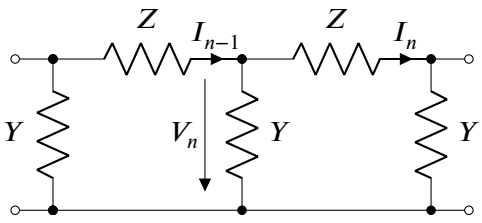

Figure 1.8.: Periodic chain of electrical cells.

use Kirchhoff's current and voltage laws to set up equations for the voltage V_n and current I_n of the nth cell

$$\begin{aligned} I_{n-1} - I_n &= YV_n \\ I_n - I_{n+1} &= YV_{n+1} \\ V_n - V_{n+1} &= ZI_n \end{aligned}$$

leading to

$$\frac{I_{n-1}}{Y} - I_n\left(Z + \frac{2}{Y}\right) + \frac{I_{n+1}}{Y} = 0. \tag{1.13}$$

when eliminating the voltage. We denote the phase advance of a wave per period as $\varphi = k_z p$ and use Floquet's theorem to write $I_n = I_{n-1}e^{-j\varphi}$ and $I_{n+1} = I_n e^{-j\varphi}$ for a forward travelling wave. When substituting into Eq. (1.13) we obtain the dispersion relation [13]

$$\cos\varphi = 1 + \frac{YZ}{2} \tag{1.14}$$

for arbitrary choices of Z and Y. The passband is confined by $-1 \leq \cos\varphi \leq 1$ with $\varphi = 0$ and π respectively. In the following we apply this equivalent circuit model to the cases of electrically,

magnetically and resonantly coupled cavities. In all cases we can define an inter-cell coupling factor k as a measure of the electromagnetic energy being induced in the second cavity by the stored energy in the first cavity, and vice versa.

The fundamental TM_{01}-mode in the iris loaded structure in Fig. 1.6a for example can be modelled by an electrically coupled circuit. Successive cells couple through the irises via the strong electric field on axis. We describe this mode with the equivalent circuit in Fig. 1.9a where we chose $Z = j\omega L_1(1 - \omega_0^2/\omega^2)$ with $\omega_0^2 = 1/L_1C_1$ and $Y = j\omega C_2$. We then solve Eq. (1.14) for ω to obtain

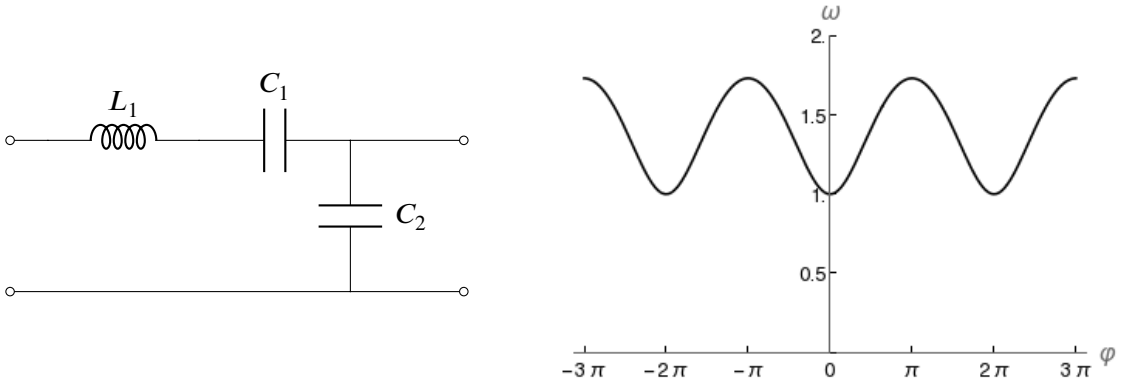

(a) Periodic array of electrically coupled circuits.

(b) Dispersion characteristic for $\omega_0 = 1$.

Figure 1.9.: Equivalent circuit model for electrically coupled resonators.

the dispersion relation

$$\omega = \omega_0\sqrt{1 + 2C_1/C_2(1 - \cos\varphi)} \tag{1.15}$$

which is visualised in Fig. 1.9b. We observe that the electrical coupling results in a forward fundamental harmonic with $\omega_\pi > \omega_0$. The 0-mode with $\varphi = 0$ corresponds to the cell resonance ω_0. As a measure of the strength of the coupling, we define the coupling factor to $k = 2C_1/C_2$ for $C_1 \ll C2$. For the case that $C_2 \to \infty$ the cell coupling vanishes and the cells become independent resonators. This would correspond to a vanishing iris diameter in Fig. 1.6a.

We repeat above treatment for the case of magnetically coupled resonators. A typical example is the disc loaded structure with peripheral slots, see Fig. 1.6b. The coupling is now inductive and modelled by $Y = 1/j\omega L_2$ as shown in Fig. 1.10a. The dispersion relation is obtained to

$$\omega = \frac{\omega_0}{\sqrt{1 + 2L_2/L_1(1 - \cos\varphi)}} \tag{1.16}$$

and plotted in Fig. 1.10b. The cell coupling is defined as $k = 2L_2/L_1$ in this case for $L_2 \ll L_1$. We note that the fundamental harmonic is now of the backward wave type and $\omega_\pi < \omega_0$.

Consider now the combination of the two structures in Fig. 1.6 with slotted discs having irises of considerable diameter. Here coupling takes place both electrically and magnetically and resonant effects can lead to interesting phenomena. Our equivalent circuit model now takes the form of

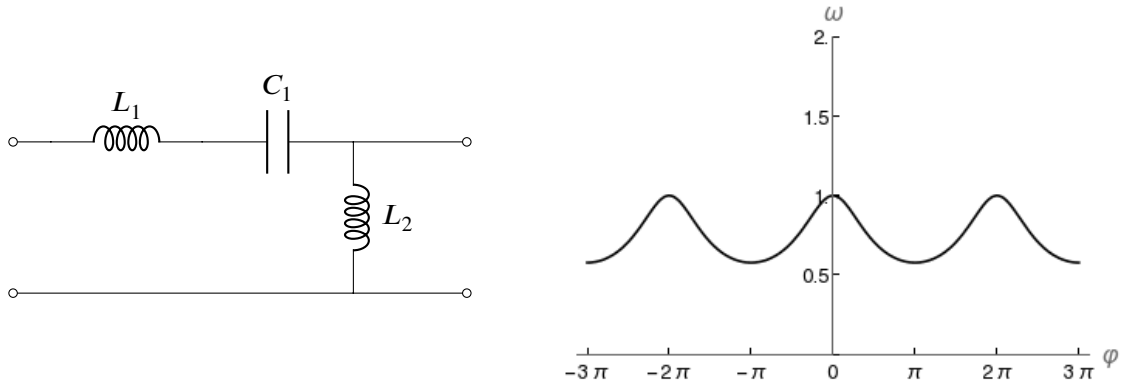

(a) Periodic array of magnetically coupled circuits.

(b) Dispersion characteristic for $\omega_0 = 1$.

Figure 1.10.: Equivalent circuit model for magnetically coupled resonators.

Fig. 1.11a with the resonant admittance $Y = j\omega C_2(1 - {}^{\omega_2^2}/_{\omega^2})$ as the coupling element and where $\omega_2^2 = {}^{1}/_{L_2C_2}$. We obtain the dispersion relation [13]

$$\omega = \sqrt{b \pm \sqrt{b^2 - \omega_0^2\omega_2^2}} \tag{1.17}$$

with

$$b = \left(\frac{\omega_0^2 + \omega_2^2}{2}\right)(1 + k^2(1 - \cos\varphi)),$$
$$k^2 = {}^{2}/_{[L_1C_2(\omega_0^2+\omega_2^2)]}.$$

It now consists of two branches, one for each of the two resonators in the single cell of the structure. For $\omega_0 \neq \omega_2$ a stopband exists between the passbands of the two resonators and the dispersion relation is symmetric with respect to an interchange of ω_0 and ω_2. By considering Figs. 1.11b to 1.11d we observe that the slopes near the 0-modes steepen when ω_0 and ω_2 approach each other. For the case of the so-called confluence of the passbands displayed in Fig. 1.11d the two branches run into each other with non-zero slope.

This shaping of the dispersion curve is used in standing wave accelerating structures of e.g. the Alvarez type. By also periodically deploying a stem [14] or post [7] configuration, refer to Fig. 1.4 for instance, the accelerating transverse magnetic $(\mathrm{TM})_{01}$ passband is coupled to a stem- or post-passband respectively. The increased group velocity at the 0-mode results in larger power flow and mode separation leading to better field stability and less susceptibility to manufacturing tolerances and beam loading. Overall this reduces the energy spread of the beam. The acceleration structure extensively treated throughout this thesis features stems as resonant coupling elements and part of the theory presented here can be readily applied. The stems are however not merely employed to achieve confluence, but are rather the accelerating element of the structure.

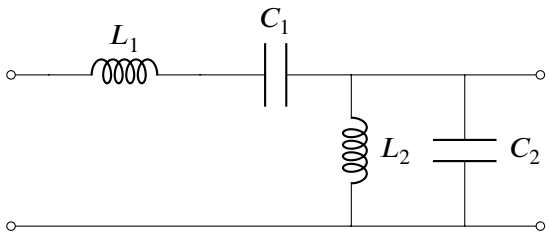

(a) Periodic array of resonantly coupled circuits.

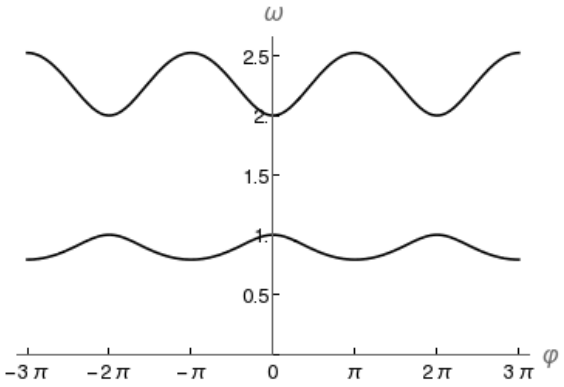

(b) Dispersion curves for $\omega_0 = 1$, $\omega_2 = 2$, $k = 0.2$.

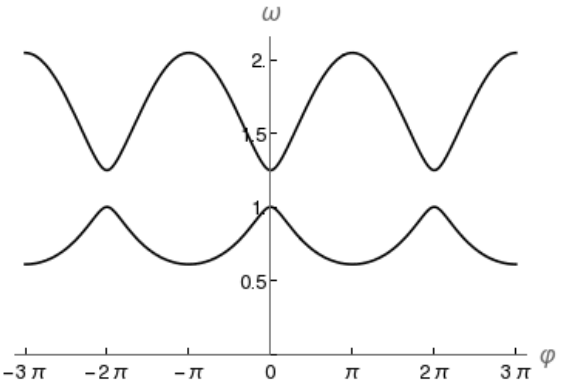

(c) Dispersion curves for $\omega_0 = 1$, $\omega_2 = 1.25$, $k = 0.4$.

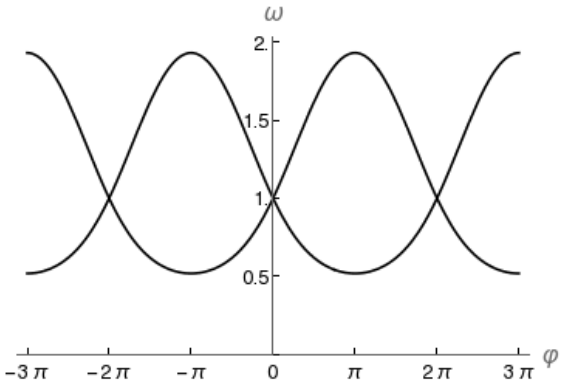

(d) Dispersion curves for $\omega_0 = \omega_2 = 1$, $k = 0.5$.

Figure 1.11.: Equivalent circuit model for resonantly coupled resonators with coupling factor k.

1.2. Particle Acceleration in Synchrotrons

To bring protons up to highly relativistic energies, LINACs were soon found to be inefficient. This is mostly due to the fact that each electrode or accelerating device can only be used once for the acceleration of a particular particle and that therefore the length and the cost of the LINAC increase linearly with its final energy. In a machine in which particles travel on circular orbits the accelerator elements can be used repeatedly supposing that the accelerating device can be adapted adequately from turn to turn in the case that the particle velocity still increases. This idea culminated in the development of the synchrotron and its basic building blocks are shown in Fig. 1.12. Dipole magnets bend the particles around the quasi-circular orbit of constant radius. The synchrotron needs as a minimum only a single, relatively short accelerating section potentially with an adjustable RF frequency. Acceleration is then achieved by a choreographed interplay between dipole magnets and RF system. The magnet current is increased forcing the particles on a slightly shorter orbit. The RF system then supplies additional energy to the particles shifting them back towards their nom-

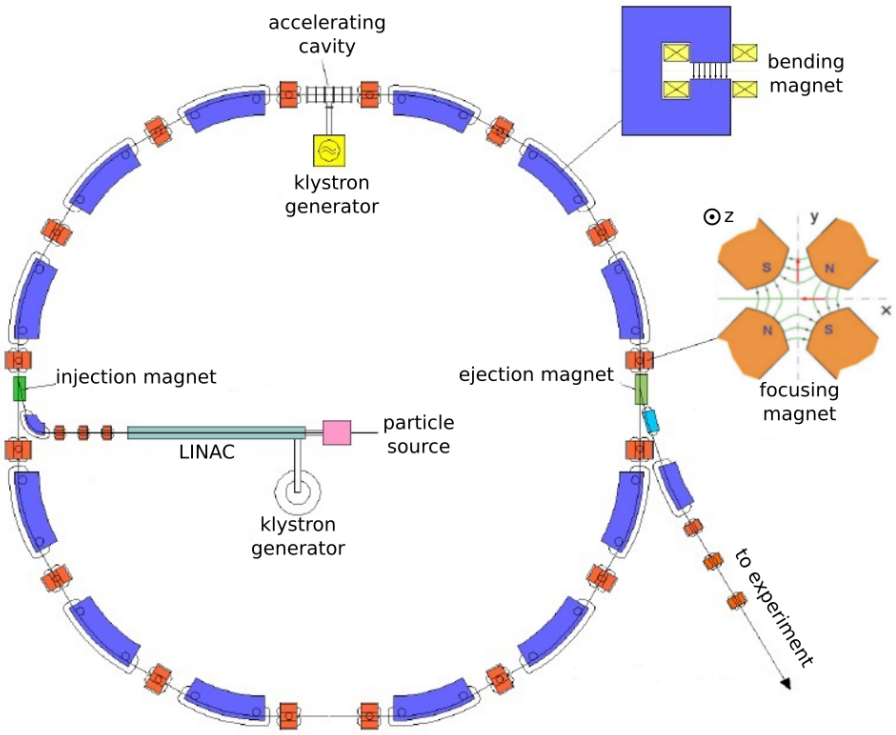

Figure 1.12.: Basic building blocks of a synchrotron, adapted from [2, 15].

inal orbit in the aperture, e.g. the centre of the vacuum chamber. The magnet current is ramped in synchronism with the particle energy, hence the name synchrotron.

To cope with machine imperfections and the repelling space charge forces within the particle bunches, the focusing effect of quadrupole magnets is used to confine the beam to the narrow aperture of the vacuum chamber in the horizontal and vertical planes. Figure 1.12 shows a quadrupole focusing particles with momentum in direction $-z$ and a horizontal offset from the magnet axis. The restoring force increases linearly with the offset. Particles with a vertical offset however undergo further defocusing. This concurrent focusing and defocusing in the two transverse planes is an intrinsic behaviour of quadrupoles. A quadrupole focusing in the vertical plane can however easily be obtained by rotating the horizontally focusing quadrupole by 90° or by changing its pole currents. In a synchrotron, horizontally focusing and defocusing quadrupoles are interleaved and spaced by their focal length resulting in an oscillatory motion of the beam also in the two transverse planes while moving around the synchrotron. Higher order multipole magnets like sextu-, octo- and decapoles are also used in a synchrotron, e.g. to correct chromaticity[2] and field imperfections in dipoles and quadrupoles. Together, due to their functionality like optical lenses these magnets are called the optics of the machine.

[2]the momentum dependent focusing strength in quadrupoles [16]

The longitudinal phase focusing introduced in Fig. 1.2 for linear accelerators also applies to synchrotrons (below transition energy[3]) for which the drift tube is basically the whole accelerator circumference. The particles will perform synchrotron oscillations around the synchronous particle, which undergoes the exact same accelerating voltage every turn, with the oscillation amplitude depending on the initial phase and energy. The synchrotron oscillation period is usually much slower than in the transverse planes and on the order of several turns. These energy-phase oscillations can be visualised in the so-called longitudinal phase space illustrated in Fig. 1.13. The

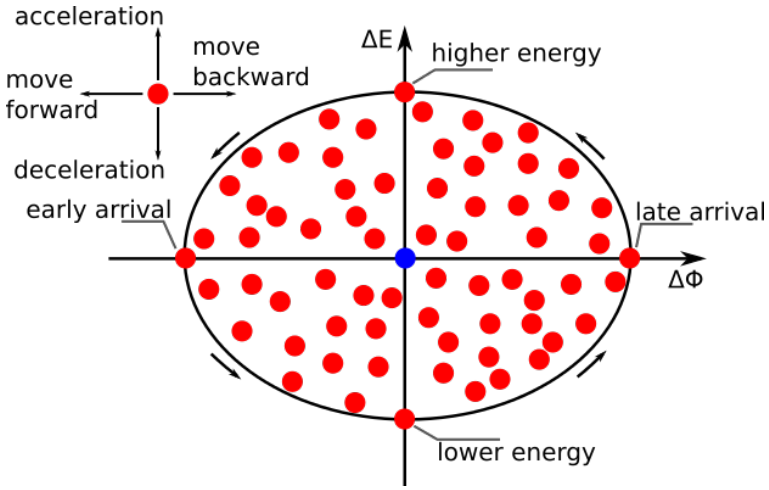

Figure 1.13.: Longitudinal particle motion visualized in phase space ($\Delta\Phi, \Delta E$). The phase space area surrounding all particles is called the emittance of the beam. The immobile synchronous particle is shown in blue.

phase space area that includes all particles is called the longitudinal emittance which is an important beam quality parameter. If the longitudinal emittance is too large for the RF system to capture all particles, see also Fig. 1.2, particles with a too large energy or phase deviation become uncontrollable and are lost in the machine.

As a synchrotron can not accelerate particles with zero velocity, a pre-accelerator, typically a LINAC, which already accelerates the beam to several tens of MeV is placed before the synchrotron in the accelerator chain. The particle beam with an emittance acceptable by the synchrotron is then transferred from the LINAC to the synchrotron via a transfer line and an injection magnet, see Fig. 1.12. This magnet, also called kicker, deflects the beam onto the orbit of the synchrotron via a transverse magnetic field. After the magnet ramp the beam is extracted from the machine via another kicker and send towards an experiment or a following accelerator or collider. In practice,

[3]The revolution period of a particle in a synchrotron depends on its velocity and energy. In the non-relativistic regime, a larger particle energy results foremost in an increased velocity and therefore reduced revolution period. In the ultra-relativistic regime, a larger particle energy results foremost in an increased orbit length and a larger revolution period. At the transition energy, the variation of velocity is exactly compensated by the variation of trajectory. In some synchrotrons the transition energy is crossed and a rapid phase jump in the RF system is required to accelerate the beam on the falling edge of the RF voltage above transition.

additional equipment like e.g. beam position and beam quality monitors and other beam instrumentation not shown in Fig. 1.12 are also located in the particle orbit.

All these accelerator devices inevitably lead to cross-sectional changes in the vacuum chamber that act as cavity-like structures along the beam path. A bunch of charged particles passing through a cavity will loose some energy to it (beam loading effect[4]) and excite EM fields, the so-called wakefields. The frequency distribution of these wakefields can be described by the concept of beam coupling impedance which is defined by the individual structure geometry and material, for details see Chapter 2. The excited frequency spectrum depends on the bunch length with shorter bunches having a larger frequency content. Depending on the loss mechanism and the resulting decay time of the EM fields in the structure and the repetition rate of the bunches, subsequent bunches will be influenced by the wakefields of a preceding bunch. In synchrotrons, in which the same particles will pass through the accelerator for thousands of turns, this can lead to a resonant build-up of the fields and a deteriorating impact on the beam stability. Depending on the decay time of the perturbing fields in such resonator-like devices, the particle motion is affected within the same bunch (single bunch effects), subsequent bunches (multi-bunch effects) and the same bunches over several turns (multi-turn effects). Therefore, the beam quality will suffer due to the beam coupling impedance of the synchrotron which eventually leads to a degradation of its performance as the beam will become less useful for physics experiments. A more in-depth and quantitative treatment on beam coupling impedance will follow in Chapter 2.

1.3. The CERN Accelerator Complex

The most famous accelerator of CERN is the LHC in which two proton beams of presently 6.5 TeV each are brought to collision. The LHC is however at the end of a whole accelerator chain in which particles are accelerated to ever higher energies in transferring the beam from one accelerator to the next. Figure 1.14 shows this accelerating complex crucial to the operation of the LHC and built over the last 60 years since the foundation of the laboratory. The evolution to larger accelerators for ever higher energies is obvious as progress in magnet technology could not keep pace with the energy range of interest for particle physics. Most of the accelerators can either be used to feed their own experiments or they are used as a beam injector for the next accelerator in the chain. In the first case of so-called fixed target experiments the particles are not made to collide with a second beam, but are shot on a material block and the particles created during the collision are studied. In the following the accelerator chain will be outlined one machine after the other, following the path of protons into the LHC.

Hydrogen atoms out of a simple gas bottle are stripped of their electrons by an electric field to yield positively charged protons. These protons are accelerated by the linear accelerator **LINAC 2** (see Fig. 1.14) over a length of 33 m to an energy of 50 MeV equivalent to 31 % of the speed of

[4]The beam loading effect will be introduced in more detail in Section 2.1.

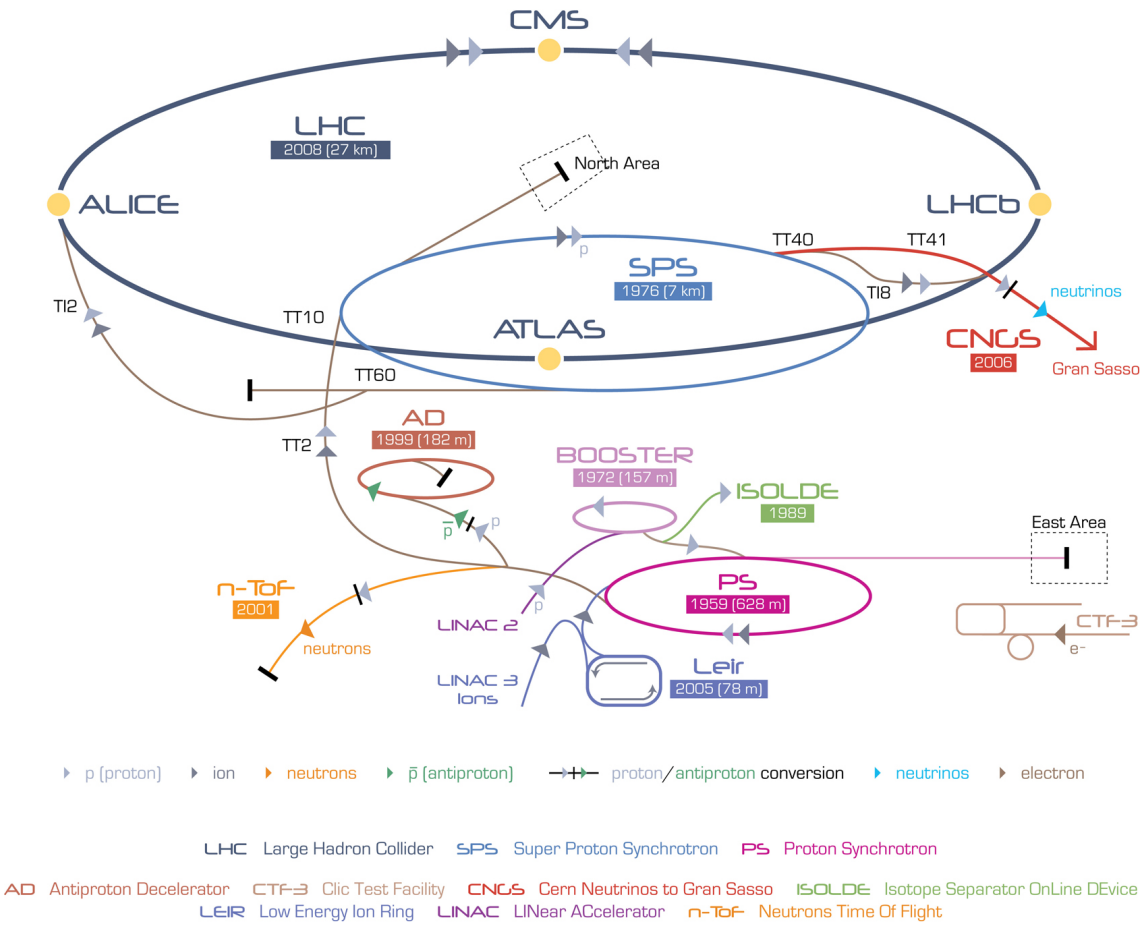

Figure 1.14.: Schematic of the CERN accelerator complex. ©CERN

light[5]. All subsequent accelerators are of the synchrotron type. This type of acceleration is more efficient for particles at higher energies as its components like RF cavities and magnets can be reused during several turns of the particles.

From LINAC 2 the beam is transferred via a continuous vacuum chamber into the **Proton Synchrotron Booster (PSB)** that consists of four rings stacked on top of each other each measuring 157 m in circumference. The main purpose of the Booster is to enhance the number of protons that can be accepted at the next stage. Otherwise, the energy delivered by LINAC 2 would be too low to achieve a sufficient beam intensity and the use of the beam for experiments would be greatly diminished.

[5]LINAC 2 was decommissioned in 2018 and will be replaced. From 2020 on, LINAC 4 will be the first accelerator in the chain accelerating protons to an energy of 160 MeV.

The PS Booster injects 1.4 GeV protons (92 % of the speed of light) recombined from the four rings into the **Proton Synchrotron (PS)**. The PS has been used to accelerate many different kind of particles including electrons, positrons and antiprotons in the past [1] and accelerates protons to 26 GeV (99.9 % of the speed of light). In the PS the point of transition is crossed at which the revolution frequency of the particles becomes dominated by an increase in mass and thus orbit length opposed to an increase of velocity. With the optics used today for proton acceleration, the PS is the only machine in the accelerator complex in which transition is crossed for this type of particle.

The **Super Proton Synchrotron (SPS)** is the next accelerator in the chain with a circumference of 7 km and lying 60 m under ground. Nowadays, protons are injected above transition in the SPS and accelerated to an energy of 450 GeV. Injection into the two vacuum chambers of the **LHC** takes place via transfer lines TI2 and TI8 in clockwise and counter-clockwise direction respectively, see Fig. 1.14. The LHC is located 79 to 140 m below ground and makes use of superconducting magnets of various types at temperatures as low as 1.8 K (-271.3°C). In total, 1,232 dipoles are used to bend and 392 quadrupole magnets are used to focus the beam. The filling with protons from the whole injector chain takes about 30 minutes and both beams are then accelerated to energies of nominally 7 TeV. This means that the protons are more than 7,000 times heavier than their rest mass and traverse the 27 km long ring over 11,000 times per second. The protons are made to collide at four locations around the accelerator ring marked in Fig. 1.14 where the four large particle detectors ALICE, ATLAS, CMS and LHCb are located. Tracks of the particles generated in the collisions are automatically analysed by large data centres connected to the detectors and studied further by physicists to conclude on their nature.

In addition, the injector chain at CERN delivers particles to other experiments also shown in Fig. 1.14. These shall only be listed in the following for completeness but are not discussed further:

- Fixed target experiments in the East and North areas fed by the PS and SPS respectively.
- The injector chain for heavy ion physics in the LHC (LINAC 3 and the Low Energy Ion Ring (LEIR)).
- The Antiproton Decelerator (AD).
- The Isotope Mass Spectrometer (ISOLDE).
- The Neutron Time-Of-Flight experiment (n-TOF).
- CERN Neutrinos to Gran Sasso (CNGS).
- CLIC test facility 3 (CTF3).

1.4. High-Luminosity LHC and LHC Injector Upgrade Projects

Particle detectors need to record large amounts of collision data so that sufficient statistical evidence is obtained to e.g. announce the discovery of a new particle. In order to increase the probability of observing interesting events or new physics, the amount of particle collisions should be as large as possible. The performance of a particle collider is therefore measured not only by its collision energy but also by its rate of collisions called luminosity. Luminosity quantifies the number of collisions per unit surface over a given period of time and measures the ability of a collider to produce a sufficient amount of interesting events in a given amount of machine run-time.

The LHC's design energy is 7 TeV per beam. To ensure machine safety and for commissioning and consolidation of the four detectors, beams of up to 4 TeV were collided during the first operational run of the LHC from November 2009 to February 2013. This start-up energy was still several times higher than the most powerful accelerator up to that date and already opened a new energy frontier for exploration resulting in the discovery of the Higgs boson in 2012. It should be noted that the key results a particle accelerator can deliver are usually achieved within the first years of its operation. This enforces a constant alternation between physics runs and shutdown periods in which the accelerator receives performance upgrades. The upgrade schedule for the LHC as well as its injectors is shown in Fig. 1.15.

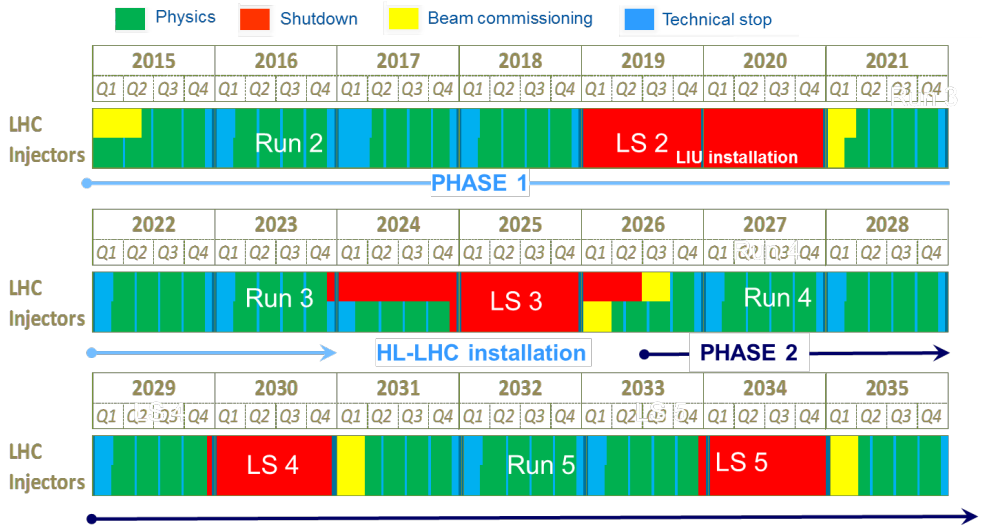

Figure 1.15.: Present schedule for the LHC and its injectors showing physics runs interrupted by machine upgrade periods. ©CERN

Since the end of the first long shutdown (LS) 1 in April 2015 the LHC ran a collision energy of 13 TeV. To fully exploit the potential of the LHC and to increase the possibility of new discoveries, its integrated luminosity (the total number of collisions per time) shall be increased by a

factor of ten during a major upgrade in the years 2024 to 2026 [17], designated LS 3 in Fig. 1.15. Consequently, today's nominal bunch intensity of $1.2{\cdot}10^{11}$ protons per bunch shall essentially be doubled to achieve the desired luminosity of $5{\cdot}10^{34}\,\mathrm{cm}^{-2}\,\mathrm{s}^{-1}$ [17]. The necessary efforts to prototype, test and implement this novel machine configuration, called the High-Luminosity LHC (HL-LHC), are described in the HL-LHC project. Overall, this project will take a decade to realize and part of its implementation has started in 2018.

Relatively new particle accelerators build in the years 2000 like the LHC were designed from scratch with a small overall beam coupling impedance budget in mind. This, however, is not the case for the older accelerators at CERN build decades ago and which were originally targeted to much lower beam intensities. Performance limitations arising from the injector chain with regard to the increased beam intensity are therefore addressed by the LHC injectors upgrade (LIU) project [18]. Within this project, each accelerator in the injector chain underwent extensive studies with the goal to increase the beam intensity and stability of the beam injected into the LHC. Several critical impedance sources of the CERN accelerator complex were identified and possible reductions of these shall be implemented during LS 2, within the schedule shown in Fig. 1.15. Also within these impedance reduction campaigns, databases for all machines consisting of their most important impedance contributors were created over the last years by bench measurements on and full-wave EM field simulations of different accelerator devices. These databases provide the necessary input for macro-particle simulations which allow to study the dynamic behaviour of different beams and machine configurations in the respective accelerators.

Relevant for this thesis are the upgrades of the SPS and its main 200 MHz RF system used for particle acceleration. Beam parameters achieved in the SPS at extraction until today and the requirements for the HL-LHC era are shown in Table 1.1 together with general parameters of the SPS. The SPS needs to deliver four batches of 72 bunches per extraction during the filling

Table 1.1.: Beam parameters achieved in the SPS until today for the proton LHC-type beam at extraction and the requirement for the HL-LHC era [17, 18, 19].

Parameter		**Achieved**	**Required**
Momentum	[GeV/c]	450	
Bunch intensity	$\cdot 10^{11}$	1.2	2.3
Number of batches×bunches		4×72	
Bunch spacing	[ns]	25	
Batch spacing	[ns]	225	
Longitudinal emittance	[eVs]	0.63	<0.65
Bunch length (4σ Gaussian fit)	[ns]	1.65	<1.7
Transverse emittance	[μm]	2.36	1.89
Circumference	[m]	6911.5	
Harmonic number		4620	

of the LHC. For this type of beam and the required quality parameters like the nominal bunch length and emittances given in Table 1.1, the maximum bunch intensity is so far limited to $\sim 1.2 \cdot 10^{11}$ p/b. Larger beam intensities lead to increased relative beam losses mainly caused by

electron-cloud effect, beam instabilities in the longitudinal plane as well as beam loading in the accelerating structures which reduces the available voltage [18, 20]. The RF power available for acceleration is a limiting factor especially at flat top, where a large accelerating voltage is required for a clean transfer of short bunches into the 400 MHz RF system of the LHC. For stability of the future high intensity LHC beams in the SPS an even larger accelerating voltage than today will be required, however without modifications less voltage will be available due to the effect of beam loading [21]. The RF system in its present form is therefore not able to satisfy future needs. Hence, as the essential part within the LIU project, the accelerating system in the SPS will undergo extensive improvements to resolve the problems it poses regarding longitudinal beam instabilities and the lack of RF voltage.

The main RF system used for acceleration of all beams in the SPS is presently a group of four travelling wave structures (TWSs) operating at 200 MHz. Two of these periodic multi-cell structures consist of four and two of five sections of 11 cells each. One of the 5-section structures is shown in Fig. 1.16. The peak RF power available before LS 2 per cavity[6] was 750 kW pulsed

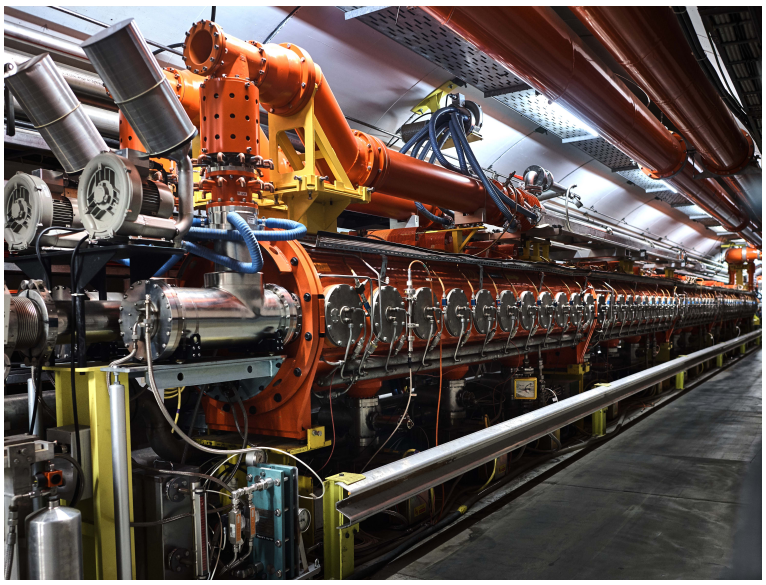

Figure 1.16.: One of the 5-section 200 MHz multi-cell TWSs used for particle acceleration in the SPS. The coaxial lines feeding the structure at the far end and the terminating coaxial water-loads at the beam entrance end in the foreground are also shown. ©CERN

(50% duty cycle at 42 kHz) [22]. In this configuration, the RF system can deliver a maximum total accelerating voltage of 7.5 MV at today's nominal LHC intensity of $1.2 \cdot 10^{11}$ p/b. The beam loading in a TWS scales with the square of its length. Even for a significant increase of input power the two long 5-section structures can therefore not provide a larger accelerating voltage at HL-LHC beam intensities than today [21]. During LS 2, the two 5-section cavities are therefore rearranged

[6]In the accelerator jargon, any system with the purpose of particle acceleration is often simply designated as cavity for convenience. Also travelling wave structures are therefore often somewhat incorrectly called travelling wave cavities.

to four shorter 3-section structures also using two spare sections. Like this, the total beam coupling impedance (the source of the beam loading effect) of the new cavity configuration consisting of two four and four three section cavities is reduced by 20 %. Two new power plants will be installed that feed the two 4-section cavities with 1.6 MW peak each [18]. The existing four power plants are upgraded to deliver 1.05 MW to feed the four 3-section cavities. Overall, these upgrades will increase the available accelerating voltage at HL-LHC intensities to 10 MV.

However, even if the limitation due to beam loading is solved with the RF upgrade, longitudinal beam instabilities in the SPS lead to an uncontrolled emittance blow-up during the ramp and consequently intensity loss [19, 20]. One of the most severe sources of instabilities in the SPS was identified within the LIU project to be already damped higher order modes (HOMs) around 630 MHz in the accelerating TWSs themselves [19, 20]. An example for a measurement of a typical instability in the SPS is shown in Fig. 1.17 [19]. As can be seen, the bunch length gets shorter

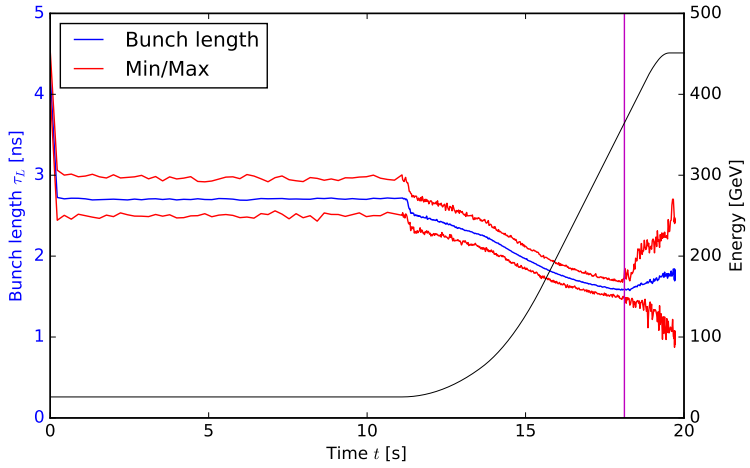

Figure 1.17.: Longitudinal instability during the SPS accelerating cycle for the LHC-type beam given in Table 1.1 with an average bunch intensity of $\sim 1.2 \cdot 10^{11}$ p/b. The beam energy is shown in black and the average bunch length in blue as a function of time. Taken from [19] with permission.

during the ramp due to a progressively larger accelerating voltage. The HOMs trigger a longitudinal multi-bunch instability which scales inversely proportional to the beam energy [21] and which manifests itself in bunch length oscillations within the batch. The minimum and maximum bunch lengths in the batch are used as a criterion to determine when the beam becomes unstable, shown by the magenta line in Fig. 1.17. The instability results in particle loss and bunches with lengths larger than 1.7 ns which should not be injected into the LHC to avoid further uncontrolled losses.

1.5. Thesis Motivation, Goals and Organisation

The SPS will not be able to reliably deliver the demanding beam required by the HL-LHC without mitigation of the HOMs around 630 MHz in the accelerating TWSs. In this respect consider Fig. 1.18, which shows the intensity threshold on the SPS flat top as a function of bunch length [23]. The data is obtained from the Beam Longitudinal Dynamics code (BLonD) [24], a 2D particle-tracking simulation code developed at CERN and which is based on a detailed impedance model of the SPS. The dot in Fig. 1.18 indicates the HL-LHC goal which is to be reached. As can be seen

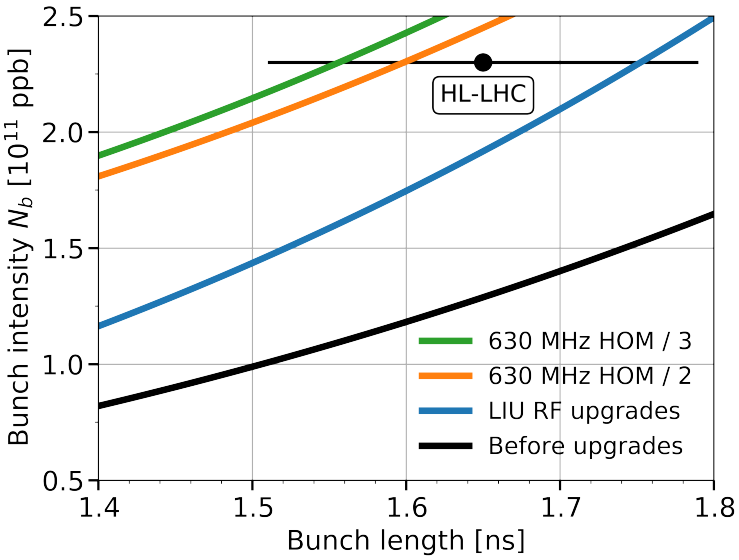

Figure 1.18.: Instability threshold on the SPS flat top as a function of bunch length obtained from particle simulations of one batch with 72 bunches. The situation until LS 2 (black) and the improvement due to the cavity rearrangement and the power upgrade (blue) are shown. The nominal HL-LHC goal of 1.65 ns bunch length and intensity of $2.3 \cdot 10^{11}$ p/b can only be reached by improved damping of the 630 MHz HOMs by a factor of two or better (orange, green) in addition to the RF upgrades. The operational variation on the bunch length is shown as well. Taken from [23] with permission.

from the simulations, the upgrade of the RF system concerning beam loading alone significantly improves the stability threshold, but is unable to assure stable beams at the desired 1.65 ns bunch length with $2.3 \cdot 10^{11}$ p/b. Only by mitigating the impedance of the HOMs in the accelerating structures the HL-LHC goals are reached, see Fig. 1.18. The lengths of the 4×72 bunches vary significantly around the nominal value during operation. An additional mitigation of the HOMs of at least a factor of three must be achieved to ensure reliable operation and to provide the required margin for operating the different bunch lengths. The 630 MHz HOM impedance reduction is therefore an essential part of the SPS upgrade and is hence included in the LIU baseline [20]. Note that, if significant improvement of 630 MHz HOM damping can not be achieved, other imped-

ance reduction campaigns like the shielding of sector valves and pumping ports will not effectively improve the intensity threshold as the HOMs are the limiting factor [25].

The HOMs around 630 MHz were already known to trigger longitudinal instabilities within the first year of SPS operation [26, 27]. At that time the instability was cured mainly by the use of damping probes with resistive loads placed on top of a number of cells which couple strongly to the mode around 630 MHz while being equipped with a rejection filter for the fundamental mode at 200 MHz [27]. The achieved damping is so tremendous that the accelerating structure could be operated over the last 40 years although the average beam current increased by around 3.5 times since then. For HL-LHC intensities however, macro-particle simulations suggest that an **additional damping** by a factor three of these already heavily damped HOMs is required [20], refer again to Fig. 1.18. A brief estimation can be made on the loaded (damped) quality factor Q_l required to completely suppress an instability of multi-bunch type on a beam with 25 ns bunch spacing. The EM fields in a cavity resonator with quality factor Q and angular resonant frequency ω_0 decay exponentially with the decay time (refer to Eq. (2.16) or to e.g. [28])

$$\tau = \frac{2Q}{\omega_0}. \tag{1.18}$$

This means that ideally the HOM damping should result in $Q_l \approx 50$ to avoid that subsequent bunches are significantly influenced by their preceding bunches. The undamped Q_0 of the HOMs is in the order of 18,000 which would correspond to an overall damping of ≈ -50 dB. The damping deployed already in 1976 results in $Q_l \approx 300..500$. Damping HOMs in a multi-cell cavity to these extents without influencing noticeably the fundamental accelerating mode is an extremely challenging and very ambitious task.

The goal of this thesis is to properly identify and characterise the offending modes in the 630 MHz frequency range of the accelerating TWSs and to mitigate these already heavily damped modes by an amount that significantly increases the beam instability threshold. The focus is on the new, shorter 3-section structures which have never been used in the SPS before, however studies are currently ongoing to apply the mitigation strategies developed throughout this thesis also to the 4-section structure. Further challenges are the lack of a general HOM-mitigation strategy on cavities with a large number of cells as well as computationally heavy full-wave EM field simulations with respect to both data volume and computation time due to the large physical size of the structures. A perturbation of the travelling-wave fundamental mode with regard to a detuning or damping due to the HOM mitigation will have a direct impact on the available accelerating voltage during the ramp. Another goal of the thesis is therefore to study and quantify the impact of damping probes and other devices for HOM mitigation on the accelerating mode and a solution was worked on that allows to damp the HOMs in the structure while keeping the impact on the accelerating mode within acceptable limits.

The thesis is organised as follows. Some fundamentals of particle acceleration with EM structures and the synchrotron principle are outlined in this first chapter. It is also shown how the thesis is embedded in the overall upgrade programs at CERN to increase the performance of the accelerator complex in view of the HL-LHC goals. Chapter 2 introduces the concept of beam coupling impedance which is used to describe the interaction of the particle beam with the accelerator devices

surrounding it. The impedance theory for standing wave resonances, like the HOMs in the SPS 200 MHz TWS, as well as for travelling wave modes is given. For the development of effective and in practice applicable HOM mitigation strategies, a broad understanding of the acceleration system including its fundamental mode is necessary. This is why in Chapter 3 the TWS is analysed in detail. An overview over the whole acceleration system is given together with consequences of a detuning or mismatch of the structure. The latter are important to later on analyse the impact of the HOM mitigation devices on the fundamental mode. The beam coupling impedance of the fundamental and higher order modes of the 33-cell structure including the existing damping scheme is simulated and analysed via EM codes. The HOM mitigation is systematically improved in Chapter 4 after properly identifying and characterising the modes with largest beam impedance. Appropriate measures are taken that target these HOMs, including an optimisation of the existing HOM coupler and a new mitigation technique via resonating elements that are directly placed onto the wall of the TWS. The practical feasibility of the proposed mitigation techniques is always taken into account. RF measurements of the TWS in different configurations are reported in Chapter 5. The goals are, amongst others, a confirmation of the simulation results in Chapter 4 as well as quantifying the deteriorating impact of the newly proposed mitigation scheme on the accelerating voltage. The thesis is concluded in Chapter 6 by a review and summary of its achievements.

2. Wakefields and Impedances

In order to mathematically describe the motion of charged particles in high-energy accelerators, the concepts of the wake function in the time domain and the beam coupling impedance in the frequency domain are in use since decades. In this chapter these two concepts are briefly introduced and applied to the cases of standing wave cavities and of TWSs which can both be used for particle acceleration. This also lays the foundation for numerical Eigenmode and Wakefield simulations used extensively throughout this thesis for the calculation of accelerator component impedances.

2.1. Longitudinal Wake Function and Wake Potential

In RF particle accelerators, packets of particles, so-called bunches, are accelerated instead of single particles. When a particle beam passes a discontinuity in the vacuum chamber or a surface of finite resistance, it will excite and leave behind EM fields known as the wakefield. This wake will not only influence the exciting bunch itself, but depending on the decay time of the fields also the subsequently following bunches. Due to this parasitic interaction of the beam with the surrounding accelerator components, the beam quality can get degraded and in the worst case the wakefields lead to beam instabilities or even beam loss. This holds especially true for the case of synchrotron acceleration in which the particles traverse the same discontinuities i.e. the same disturbance in every turn.

The forces acting on the charged particles and their resulting motion can be expressed in both the time and frequency domain. It is thereby usually sufficient to study only the integrated interaction over an accelerator device instead of the applied forces at single points in space. According to the direction of the forces that are integrated, a distinction is made between longitudinal and transverse planes with respect to the direction of motion. This work focuses on effects in the longitudinal plane since the longitudinal beam impedance is the known source of instabilities in the SPS [20].

We are now considering a single charged particle that is moving with speed βc in a smooth vacuum chamber like e.g. a section of the beam pipe. Thereby c designates the speed of light in free space and β the relative velocity v/c. The particle induces a corresponding image charge on the vacuum chamber walls. The spherical electric field of a stationary point charge (electrostatic case) is contracted to the plane perpendicular to the direction of motion with increasing velocity. The situation is illustrated in Figure 2.1a and the opening angle of the electric field is given by the

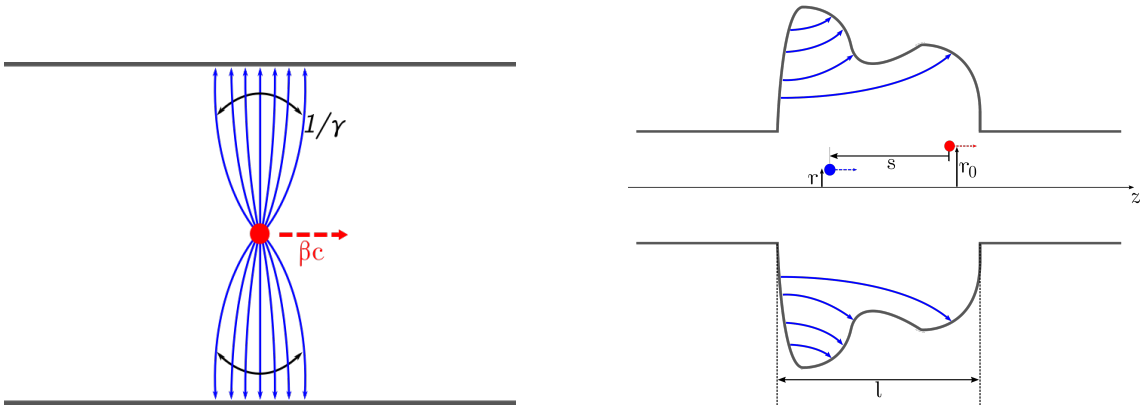

(a) Smooth metallic vacuum chamber.

(b) Cavity-like accelerator component.

Figure 2.1.: Illustration of a point charge travelling at relativistic velocity and the corresponding electric fields in different environments.

relativistic Lorentz factor [8]

$$\gamma = \frac{1}{\sqrt{1-\beta^2}}. \tag{2.1}$$

For the ultra-relativistic case with $\beta \approx 1$ there is no self-induced field in front or behind the charge. If however the particle traverses a cross-sectional change in the vacuum chamber or enters a device of arbitrary cross section, the image charge on the outer walls will have to travel a longer distance than the particle trajectory. The EM fields will therefore tear off and are left behind, building up the so-called wakefields which possibly start to oscillate, see Figure 2.1b.

For the following mathematical treatment the rigid beam approximation is used which assumes a particle speed $v \to c$ and no change of the beam trajectory due to the wakefields induced by the first particle (called the source particle). Furthermore, perfectly conducting walls and straight beam trajectories along the longitudinal coordinate z are assumed. A second particle (called the probe particle) with charge q is now considered that follows at a distance s behind the source particle and at a transverse offset r to the geometric centre of the structure. Assume that the source particle has a charge q_0 and travels at an offset r_0 parallel to the axis of the structure. The longitudinal wake function can then be calculated by integrating the longitudinal component of the Lorentz force $F_{||}(r_0, r, s, z) = qE_z(r_0, r, s, z)$ over the device length l [29]. Since the magnetic field is perpendicular to the direction of particle motion, it does not contribute to longitudinal forces acting on the particles. The longitudinal wake function is expressed by normalising to both the source and probe particle charges

$$G_{||}(r_0, r, s)\,[V/C] = -\frac{1}{q_0}\int_0^l E_z(r_0, r, t = \frac{s+z}{c})dz. \tag{2.2}$$

This is a longitudinally retarding voltage per unit charge and it is convention to add a negative sign to obtain a positive wake for a decelerating field. In the longitudinal plane and for rotationally-

or axis-symmetric structures usually the case $r_0 = r = 0$ is of most interest[1]. The wake function $G_{||}(s)$ is the Green function (i.e. the response to a step excitation) for a particular structure as it is excited by a point charge.

We now consider the case that the wakefield excitation is due to a bunch of particles with arbitrary longitudinal bunch charge distribution $I(s)$ with distance s to the probe charge measured from the bunch centre. The wake potential $W_{||}(s)$ is obtained from the convolution of the wake function with the normalised line charge density $\lambda(s) = I(s)/Q_{tot}$ [29]

$$W_{||}(s)\,[V/C] = \int_0^\infty G_{||}(s')\lambda(s-s')ds'. \tag{2.3}$$

The wake potential is actually the result obtained from numerical wakefield solvers like e.g. the time domain solver T3P of the ACE3P [31] simulation suite used throughout this thesis. For more details on wakefield simulations see Section 3.7.

Eq. (2.3) describes the voltage seen by a particle following at a distance $s > 0$ on the exciting bunch. As mentioned above, due to causality no EM fields are in front of a charge travelling at the speed of light c so that $W_{||}(s) = 0$ for $s < 0$. In the limit of $s \to 0^+$, the self-induced voltage by a particle on itself is [29, 32]

$$W_{||}(0) = \frac{1}{2}W_{||}(0^+) \tag{2.4}$$

and the energy lost by a particle of charge q to an initially empty cavity is $\Delta U = qW_{||}(0^+)/2$. This is often called the fundamental theorem of beam loading. The wake function will be illustrated in Section 2.3 (Fig. 2.5.).

2.2. Longitudinal Beam Coupling Impedance

The concept of an impedance in an electrical circuit is analogous to wakefields induced by a charged particle beam in an accelerator component. The beam constitutes a time varying current source that induces a voltage along the beam trajectory. Therefore, the concept of beam coupling impedance is introduced that relates the induced voltage to the beam current over the frequency spectrum. The impedance is very useful in comparing the impact of different accelerator components on the beam and their contribution to the overall impedance budget of an accelerator that may not be surpassed to assure stable operation for a given beam intensity. Similarly to the wake function, the beam coupling impedance could directly be defined via the current and field components in the frequency domain [29]. Here however, the focus will be on the calculation of the impedance from the wake potential via the Fourier transform $\mathcal{F}$, as it is practically of more relevance for the numerical computation of beam impedance. With the convolution theorem Eq. (2.3) becomes

$$\mathcal{F}\{W_{||}(s)\} = \mathcal{F}\{G_{||}(s)\}\mathcal{F}\{\lambda(s)\} \tag{2.5}$$

[1] For this case the wake function expanded into a power series in the particle offsets reduces to the dominant zero-order term [30].

under the Fourier transform and the longitudinal beam impedance can be calculated to

$$Z_{||}(\omega)\,[\Omega] = \frac{\mathcal{F}\{W_{||}(s)\}}{c\,\mathcal{F}\{\lambda(s)\}}. \tag{2.6}$$

The beam impedance is a complex quantity, meaning that a phase shift between the exciting bunch current and the induced voltage can occur. The real part is the power spectrum of the energy loss of a point charge, whereas the imaginary part leads to a shift in the synchrotron tune[2] due to the impedance of the accelerator component. As $I(s)$ and Q_{tot} are known inputs to the numerical Wakefield simulations, Eq. (2.6) was implemented in a post-processing of wakefield simulation data generated by T3P to obtain the beam impedance of devices under study in this thesis.

2.3. Impedance of Standing Wave Resonators

For the purpose of particle acceleration, resonant EM cavities are employed voluntarily by making use of the longitudinal electric field of the fundamental cavity mode with the lowest resonant frequency. Cross-sectional changes of the vacuum pipe along the accelerator however can constitute unwanted cavities resonating at several of their (eigen-) frequencies when excited by the passing beam. These mostly unwanted cavity geometries can be approximated by cylindrical pillbox cavity shapes, see Fig. 2.2, which resonate in standing wave modes that do not propagate as long as the mode frequency is below the lowest cutoff frequency of the attached beam pipes. The field pat-

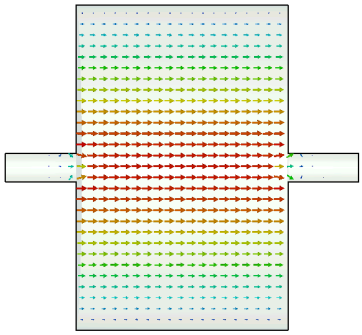

Figure 2.2.: Electric field of the fundamental[3] TM_{010} mode in a pillbox cavity with attached beam pipes (field magnitudes colour coded on a linear scale). The ratio of cavity length to radius is 1.3.

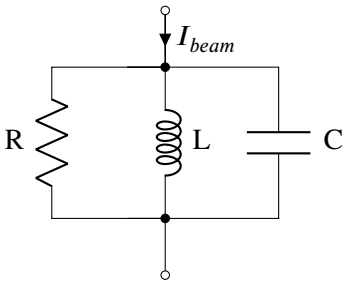

Figure 2.3.: Parallel RLC resonant circuit used to model the impedance of a single standing wave cavity resonance.

terns in such simple cavities can be calculated analytically ([9][33]) and resemble those found in many other cylindrical accelerator structures. Fig. 2.2 shows the electric field pattern of the TM_{010}

[2]The number of synchrotron oscillations (longitudinal motion) per revolution [16].

fundamental[3] mode in a pillbox cavity. For the nomenclature of mode designation in cylindrical cavities refer e.g. to [9].

The longitudinal effective voltage on-axis at the resonant frequency ω_0 of the cavity induced by either the beam or a generator current is

$$V = \int_0^l E_z(z) e^{j\omega_0 \frac{z}{\beta c}} dz. \tag{2.7}$$

The exponential accounts for the finite speed βc of the particles through the cavity of length l while the electric field $E_z(z)$ oscillates at the frequency ω_0.

Empirically, it is well known that a single cavity resonance can be modelled with a parallel RLC resonant circuit shown in Fig. 2.3. This is due to the fact that the frequency dependence of its input impedance matches the observed behaviour of cavity resonances, e.g. highest impedance exactly at the resonance frequency and a lower and wider peak with increasing losses. The impedance $Z_{||}$ presented by a cavity at one of its resonant frequencies ω_0 is therefore modelled as

$$Z_{||}(\omega)\,[\Omega] = \frac{R}{1 + jQ\left(\frac{\omega}{\omega_0} - \frac{\omega_0}{\omega}\right)}. \tag{2.8}$$

$\mathrm{Im}\{Z_{||}\}$ vanishes at the angular resonant frequency $\omega_0 = 2\pi f_0 = 1/\sqrt{LC}$ and the quality factor of the resonance was defined by $Q = \omega_0 RC$. The three independent cavity parameters resonance frequency f_0, quality factor Q and impedance R can be determined by RF measurements (see Chapter 5 for details) or EM simulations. The lumped elements R, L and C can then be derived from their relations to the cavity parameters given here. The quality factor accounts for the losses in the circuit or the physical cavity respectively, that lead to a gradual dissipation of the stored energy. The overall stored energy is also the maximum energy stored in one of the two reactive elements, and so with the use of peak (instead of rms) voltages

$$U = \frac{1}{2}C|V|^2 = \frac{1}{2}L\frac{|V|^2}{\left(\omega_0 L\right)^2}. \tag{2.9}$$

The energy dissipated in one time period is

$$\frac{P_{loss}}{f_0} = \frac{|V|^2}{2Rf_0}. \tag{2.10}$$

The same result for the quality factor as above is obtained when defining[4] it as the ratio between the stored and dissipated energy

$$Q = \frac{\omega_0 U}{P_{loss}} = \frac{\omega_0 U}{|V|^2/2R} = \omega_0 RC. \tag{2.11}$$

[3] For cavity dimensions following $l/r < 2.03$ (where l is its length and r its radius) this is the TM_{010} mode; otherwise the TE_{111} mode.

[4] In fact there is another common definition which is $Q = \frac{\omega_0}{\Delta\omega}$ and it is equivalent to the above, if $\Delta\omega$ is taken as the bandwidth between the two frequencies for which the real part of the impedance is half its maximum value [29].

Note that the cavity losses increase with decreasing R that should not be confused with the surface resistance of the cavity walls that will be introduced below.

Taking the ratio $R/Q = \sqrt{L/C}$ one notices that it does not depend on cavity losses but is given by its reactive parts only, which are exclusively determined by the geometry of the cavity. The 'R-over-Q' is therefore a fundamental quantity also called geometry factor in case of accelerator structures. With Eq. (2.11) the geometry factor[5] can be expressed by normalising the cavity voltage to the stored energy

$$\frac{R}{Q}\,[\Omega] = \frac{|V|^2}{2\omega_0 U} = \sqrt{\frac{L}{C}}. \tag{2.12}$$

It is useful to compare different modes but also different cavity geometries regarding their ability to convert stored energy into acceleration. By multiplying with the quality factor Q, the so-called shunt impedance

$$R\,[\Omega] = \left(\frac{R}{Q}\right) Q = \frac{|V|^2}{2P_{loss}} \tag{2.13}$$

is obtained. With increasing losses the ability of the cavity to shunt the accelerating gap is diminished and its impedance is reduced. The resistive shunt impedance R is equivalent to the beam coupling impedance $Z_{||}$ at resonance, see Eq. (2.8).

The resonator impedance $Z_{||}$ is shown in Fig. 2.4 for two examples. The shunt impedance determines the peak impedance at resonance and the quality factor the width of the resonance. $\mathrm{Im}\{Z_{||}\}$ behaves as an inductor for $\omega \ll \omega_0$ and capacitive for $\omega \gg \omega_0$, see Fig. 2.4b. At resonance, $\mathrm{Im}\{Z_{||}\}$ vanishes.

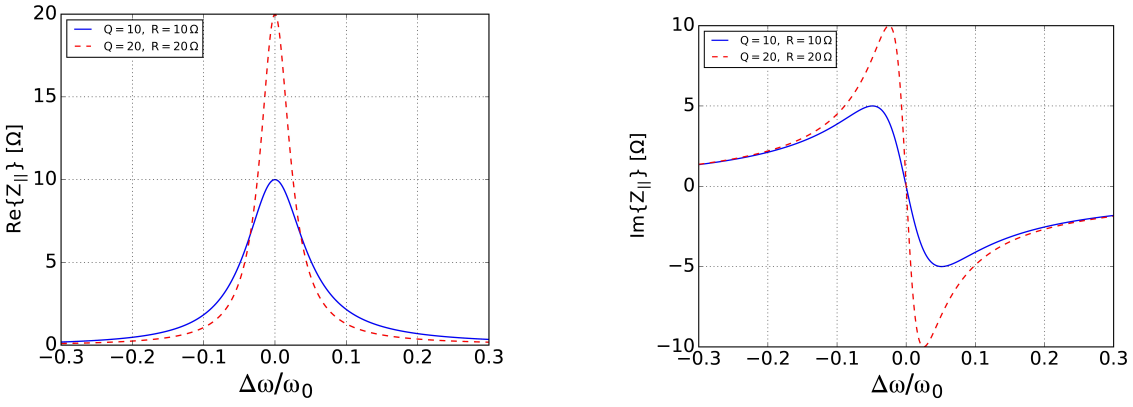

(a) Real part.

(b) Imaginary part.

Figure 2.4.: Impedance $Z_{||}(\omega)$ versus $\frac{\omega-\omega_0}{\omega_0}$ of two resonators with identical resonant frequency and R/Q.

[5]Confusingly, another so-called 'linac definition' for the R/Q is also in use in the accelerator community, which drops the factor ½ although peak voltages are used. The physically meaningful 'circuit definition' given above will be used throughout this thesis.

To model a single cavity resonance with the parallel RLC resonant circuit, the three independent cavity parameters ω_0, Q and R/Q have to be determined by either analytical methods, numerical simulations or measurements. Analytical calculations are often infeasible for nowadays complicated accelerator structures. Determination of the cavity parameters by measurements is shown in Chapter 5. For the numerical calculation of eigen-frequencies and field distributions of lossless and closed resonant structures, usually Eigenmode solvers are used[6]. The various RF parameters like e.g. the on-axis effective voltage can then all be calculated from the resulting electric and magnetic field distributions. The total, time-averaged stored energy is defined as [10]

$$U = U_e + U_h = \frac{1}{4}\int_V \left(\varepsilon|\vec{E}|^2 + \mu|\vec{H}|^2\right) dV. \tag{2.14}$$

At first, the Eigenmode solver determines the EM fields assuming a lossless cavity with perfectly conducting walls and without enforcing excitations in the cavity volume. The actual resistive power loss on the cavity walls is then calculated after the solver run by taking the surface integral over the magnetic field tangential to the inner cavity surface as [13]

$$P_{loss} = \frac{R_s}{2}\int_S |H_{||}|^2 dS. \tag{2.15}$$

$R_s = \sqrt{\mu_0\omega_0/2\sigma}$ is the surface resistance of the cavity walls with the electrical conductivity σ. From Eq. (2.14) and Eq. (2.15) the resonance parameters Q, R/Q and R are determined via Equations (2.11) to (2.13).

In Eigenmode simulations every cavity resonance is treated individually, however especially at higher frequencies resonances will overlap. The total EM field in the cavity is the vector sum of all modal fields and the overall impedance can be obtained by summing the contributions of individual RLC resonators. Finally, it should be noted that a standing wave cavity presents the same impedance to the beam and the RF generator. This is not true for TWSs as will be shown in the following section.

The resonator impedance $Z_{||}$ in Eq. (2.8) is Fourier transformed to obtain the wake potential

$$W_{||}(t) = \frac{\omega_0 R}{Q} e^{-t/\tau}\left[\cos\left(\omega_0\sqrt{1-\frac{1}{Q^2}}t\right) - \frac{1}{2Q\sqrt{1-\frac{1}{4Q^2}}}\sin\left(\omega_0\sqrt{1-\frac{1}{Q^2}}t\right)\right], \tag{2.16}$$

where $\tau = 2Q/\omega_0$ is the decay time [13]. In Fig. 2.5 the fundamental theorem of beam loading ($s = 0$) and the causality for beams with velocity c ($s < 0$) is also illustrated as discussed in Section 2.1. The wake of the resonance with higher quality factor keeps ringing in the cavity for a longer time and its impact on following particle bunches is therefore higher than that of the second resonator with $Q = 10$ in Figs. 2.4 and 2.5.

[6] With the newest additions to the e.g. CST and ACE3P codes also lossy eigenvalue problems can be solved by non-linear techniques.

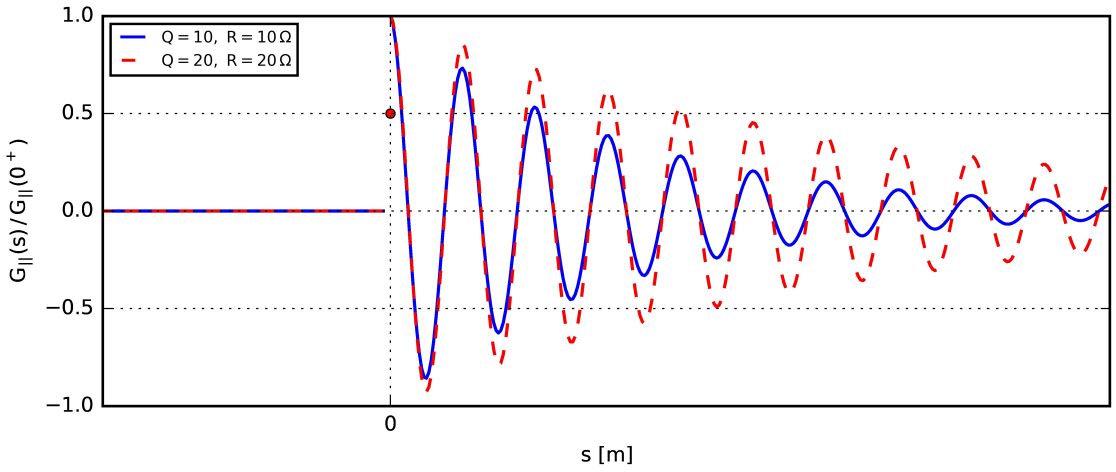

Figure 2.5.: Illustration of the wake function of the resonators shown in Fig. 2.4.

2.4. Impedances of Travelling Wave Structures

TWSs are essentially periodically loaded waveguides fed by a generator at the RF input and terminated by a matched load on the opposite side of the structure as is illustrated in Fig. 2.6. A TWS allows wave propagation at any frequency within one of its passbands opposed to (multi-cell) standing wave cavities in which the boundary conditions are satisfied only at discrete frequencies. To

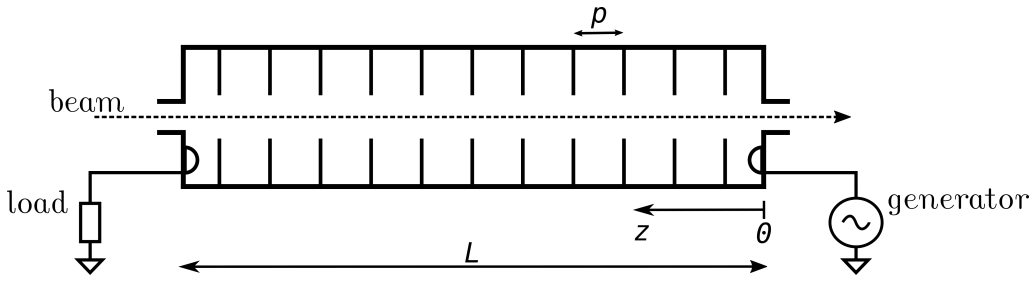

Figure 2.6.: Schematic of a travelling wave structure. For illustration, the loading elements are assumed to result in a backward-wave passband.

use such structures as particle accelerators the phase velocity v_p of the travelling EM wave must either be equal or be close to the particle velocity[7]. With the correct injection phasing into the structure, the particles then see a forward directed electric field while travelling along the structure. The phase velocity can be adjusted according to the kinetic energy of the particles that are to be accelerated by the type and dimensions of the waveguide envelope and the periodic loading.

[7]Otherwise, using $e^{-jk_z z}$ in Eq. (2.7) as the dominating term for the wave travelling in direction z, the factor $\int e^{j\omega\left(\frac{1}{\beta c}-\frac{k_z}{\omega}\right)z} dz$ where $k_z/\omega = 1/v_p$ is negligible for long distances.

We would now like to derive the accelerating voltage V_{rf} produced by the RF generator current I_g on the longitudinal axis of a TWS. The peak value of the accelerating field E_0 can be taken as constant along the structure as the attenuation length l_0 of such structures is typically much longer than their physical length, see Eq. (A.15). Let's assume equal particle and phase velocity for some relative particle velocity $\beta = \beta_0$ and travelling wave frequency $\omega = \omega_0$. For this case of perfect synchronism the accelerating voltage is simply proportional to the length of the structure L and is written as $V_{rf} = E_0 L e^{j\Phi}$. The angle Φ accounts for a possible phase shift between particle and wave half-way along the structure due to the injection-timing. A particle experiences maximum energy gain when entering the guide at a phase such that it is at the crest of the wave in the middle of the structure. For deviations of the particle velocity $\beta = \beta_0 + \Delta\beta$ or the frequency $\omega = \omega_0 + \Delta\omega$ from the synchronous cases the phase between particle and travelling wave will slip along the structure. For high energy particle accelerators we can assume $\Delta\beta = 0$, meaning that the particle velocity does not change during the traversal of the structure. The total accumulated phase slip $\tau(\Delta\omega)$ at the end of the structure then consists of a term $\tau_1(\Delta\omega)$ due to the dispersive characteristic of the structure and a term $\tau_2(\Delta\omega)$ caused by the non-synchronous particle velocity

$$\tau(\Delta\omega) = \tau_1(\Delta\omega) - \tau_2(\Delta\omega). \tag{2.17}$$

We assume further that the frequency deviation $\Delta\omega$ is small. The phase deviation τ_1 accumulated by the travelling wave over the full length L of the structure compared to the synchronous frequency can then be determined from the linear region of the dispersion curve around ω_0 for which holds

$$v_g = \frac{L\,\Delta\omega}{\tau_1(\Delta\omega)}. \tag{2.18}$$

The phase slip due to the beam is similarly derived from

$$\beta_0 c = v_p = \frac{L\,\Delta\omega}{\tau_2(\Delta\omega)}. \tag{2.19}$$

v_g and v_p are the group and phase velocities respectively for the synchronous case (β_0, ω_0). The total phase slip is obtained to

$$\tau = \frac{L\Delta\omega}{v_g}\left(1 - \frac{v_g}{v_p}\right) \tag{2.20}$$

Finally, we integrate the accelerating electric field induced by the RF generator along the structure, now also taking into account the phase slip per unit length between beam and RF wave. Note that the phase reference is taken in the middle of the structure for convenience. The effective accelerating voltage seen by the beam is

$$V_{rf} = E_0\, e^{j\Phi} \int_{-L/2}^{L/2} e^{j\frac{\tau}{L}z} dz = E_0\, e^{j\Phi}\, L \underbrace{\frac{\sin(\tau/2)}{\tau/2}}_{\text{TTF}} \tag{2.21}$$

including the so-called transit time factor (TTF) [27]. With respect to the definitions given for the standing wave resonator in Eqs. (2.11) and (2.13), the quality factor of the waveguide is defined as

$$Q = \omega \frac{\text{stored energy per unit length}}{\text{dissipated power per unit length}} \tag{2.22}$$

and the shunt impedance per unit length as

$$R\,[\Omega/\mathrm{m}] = \frac{(\text{accelerating field})^2}{\text{dissipated power per unit length}}. \tag{2.23}$$

With the series impedance R_2 defined in Eq. (A.7) the peak accelerating field can be expressed as $E_0 = \sqrt{R_2 P}$, where the power flow through the structure is $P = {}^1/_2 I_g^2 Z_0$. I_g is the peak generator current and Z_0 the characteristic impedance of the coaxial RF system. The accelerating voltage can then be written with the forward transfer impedance Z_{rf}

$$V_{rf} = Z_{rf}\, I_g\, e^{j\Phi} = \underbrace{L\sqrt{\frac{R_2 Z_0}{2}}\,\frac{\sin({}^\tau/_2)}{{}^\tau/_2}}_{Z_{rf}}\, I_g\, e^{j\Phi}. \tag{2.24}$$

The forward transfer impedance of a fictitious TWS with constant group velocity over the displayed frequency range is illustrated in Fig. 2.7 for two unit lengths. The typical $\sin(x)/x$-

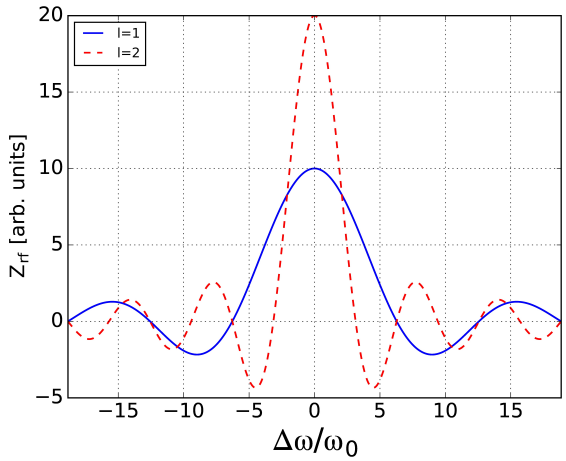

Figure 2.7.: Illustration of forward transfer impedance Z_{rf} of a TWS for two unit lengths assuming v_g = const. over the frequency range.

behaviour due to the TTF (see Eq. (2.21)) limits the usable bandwidth of the structure. The longer the structure, the smaller is its bandwidth but the higher is its efficiency for acceleration at small phase slips. The efficiency of the TWS is zero at frequencies for which ${}^\tau/_2 = n\pi \mid n \in \pm 1, \pm 2, \ldots$. In practice v_g varies rapidly in the passband so that the zeros lie asymmetric around the centre frequency f_0 of the structure.

For the derivation of the beam coupling impedance of a TWS we again start by considering the case of perfect synchronism between the phase velocity of the induced wave and the particle velocity of the beam [34]. Then, the waves excited in each cell will travel in synchronism with the beam along the structure. Therefore, the waves add linearly in the beam-forward direction,

whereas on-average they cancel out in the reverse direction. The decelerating electric field seen by the beam is then simply proportional to the length of the structure measured from the RF input end[8]. For the case of non-perfect synchronism a phase factor $e^{j\theta}$ with $\theta = \omega t - kz$ with the wave propagation constant $k = {}^{2\pi}/_{\lambda_g}$ is introduced. The induced field $E_b(z)$ is proportional to the phase slip along the structure

$$E_b(z) \propto \int_0^z e^{j\omega t - kz'} dz'. \tag{2.25}$$

By linear expansion of θ around the synchronous point (ω_0, k_0) one obtains

$$\theta = \omega t - kz = \left(\frac{\omega_0 + \Delta\omega}{v_p} - k_0 - \Delta k \right) z = \left(\frac{\Delta\omega}{v_p} - \Delta k \right) z \tag{2.26}$$

with the particle velocity being equal to the phase velocity $v_p = z/t$. The expansion can be conveniently expressed via the group velocity $v_g = {}^{\Delta\omega}/_{\Delta k}$ and the phase slip τ derived in Eq. (2.20)

$$\theta = -\tau \frac{z}{L}. \tag{2.27}$$

Solving the integral

$$E_b(z) \propto \int_0^z e^{j\theta} dz' = \frac{1 - e^{-j\frac{\tau}{L}z}}{j\frac{\tau}{L}}. \tag{2.28}$$

is then straightforward. It is obvious that the beam induced field is zero at the end of the TWS connected to the generator ($z = 0$). This means that the generator does not see the beam and always remains matched to the structure without the need for a protective circulator. By integrating the induced electric field along the structure and when making use of the identity $(1 - \cos(2x))/2 = \sin^2(x)$, the total self-induced voltage V_b on the beam is obtained to

$$V_b \propto \int_0^L \frac{1 - e^{-j\frac{\tau}{L}z}}{j\frac{\tau}{L}} dz = \frac{L^2}{2} \left[\left(\frac{\sin({}^{\tau}/_2)}{{}^{\tau}/_2} \right)^2 - 2j \, \frac{\tau - \sin(\tau)}{\tau^2} \right]. \tag{2.29}$$

With the series impedance R_2 of the structure introduced in Eq. (A.7) the beam coupling impedance of a TWS is given by [34, 35]

$$Z_b = \frac{R_2 \, L^2}{8} \left[\left(\frac{\sin({}^{\tau}/_2)}{{}^{\tau}/_2} \right)^2 - 2j \, \frac{\tau - \sin(\tau)}{\tau^2} \right]. \tag{2.30}$$

The complex beam coupling impedance is illustrated in Fig. 2.8 and it should be noted that it scales with the length squared. Obviously forward transfer and beam coupling impedances of a TWS are not identical as it is the case for standing wave cavities. As the forward transfer impedance is real valued and as the imaginary part of the beam impedance is non-zero at frequencies with vanishing real part, it is difficult to compensate beam loading in TWSs merely by adjusting the RF

[8] This is also true for backward-wave TWSs fed via the beam output end with RF power, see below.

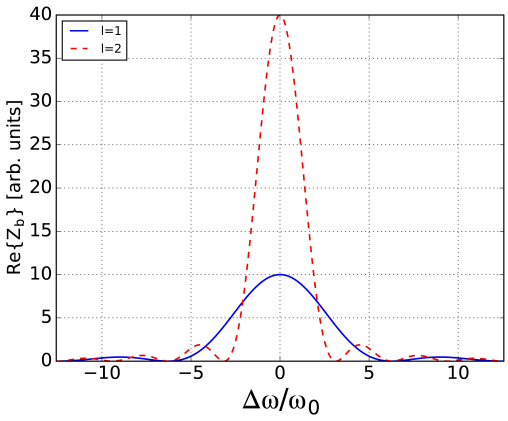

(a) Real part.

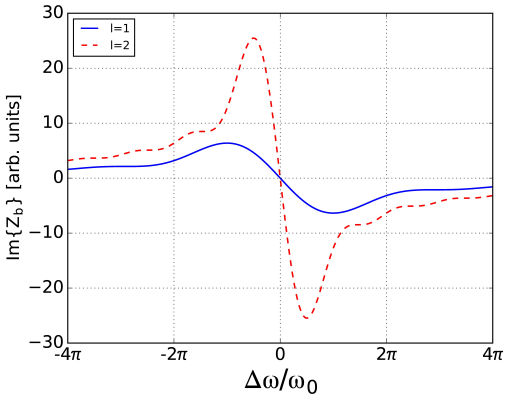

(b) Imaginary part.

Figure 2.8.: Illustration of beam coupling impedance Z_b versus $\frac{\omega-\omega_0}{\omega_0}$ of a TWS for two unit lengths assuming v_g = const. over the frequency range.

generator output. The results derived above not only apply to forward but also to backward TWSs for which group and phase velocities have opposite signs. The beam output end of a backward TWS is connected to the RF generator and the beam input end to the terminating load. The group velocity should be taken as positive in all formulae and the distance z for instance in Eq. (2.28) from the RF input end, whereas the particle velocity is to be taken as negative for a backward wave structure.

Consequently, the total voltage V seen by a beam passing through a TWS is the superposition of RF voltage and self-induced beam loading

$$V = Z_{rf} I_g - Z_b I_b. \tag{2.31}$$

3. The SPS 200 MHz Parallel Stem Acceleration System

In the following chapter different aspects of the SPS 200 MHz structure are analysed in detail for reference in later chapters. This includes a review of particle acceleration with travelling waves opposed to with the more common standing waves and an analysis of the EM field profiles associated with the parallel stem structure in both the fundamental and higher order modes. The important passbands of the structure are analysed with a computationally very efficient unit-cell approach of the periodic structure. The devices for HOM mitigation have a parasitic impact on the fundamental accelerating mode. As this impact of the newly proposed mitigation scheme shall be quantified in detail in this thesis, tuning and matching mechanisms of the parallel stem structure are considered as well. This includes a theoretical analysis of the impact of matching errors to the RF generator and the terminating load on the accelerating voltage. An introduction of a matching technique which is later on required in simulation and RF measurements is shown as well. Some important details on the EM simulations used throughout this thesis for the analysis of the full acceleration structures are given, before the beam coupling impedance of the fundamental and higher order modes in the future 33-cell TWSs are reported.

3.1. Choice of Travelling Wave Operation for Particle Acceleration

The CERN Council authorized in the early 1960s the design study of a new proton accelerator of "a very high energy". The study group on future accelerators presented a detailed design for a proton synchrotron of which the top energy was at first fixed to 300 GeV [36]. During the design phase the beam intensity was becoming an equally important parameter as the top energy in particle accelerator research. The accelerating system was therefore foresightedly designed with a future increase of beam intensity and consequently strong beam loading in mind. This accelerator became the high energy and high intensity machine known as the SPS today and only because of this foresight the accelerating system conceived more than 50 years ago can still be used today. In the following, the reasoning behind the choice of accelerating frequency and preferring a travelling-wave system over standing wave cavities as accelerating method will be outlined. More details can be found in above cited report.

The choice of accelerating frequency is influenced by many considerations, some of which are of technical and others of beam dynamics nature. For normal conducting RF systems it holds that

their geometry factor and shunt impedance per unit length increase with higher frequencies, see Eqs. (2.12) and (2.13). This means that the power required by a given type of structure with a fixed length to generate an accelerating voltage decreases with increasing frequency. However, a high frequency reduces the maximum allowed energy or phase deviation from the ideal synchronous particle that can be captured by the RF voltage and which might become too small for the desired bunch length. Also, the physical aperture - the cavity opening on the beam axis - might become too small for the beam to pass through due to its transverse motion. The chosen frequency must also fit the RF system used in the injector for synchronisation during beam transfer [36]. The availability and cost of high power sources is more favourable at some common frequency ranges and high power sources above 200 MHz were not very common in the late 1960s. Taking all these considerations into account, the frequency of the accelerating RF system was finally chosen to around 200 MHz.

In the conventional way of particle acceleration with a synchrotron the frequency of the accelerating RF system f_{rf} is kept synchronous with the particle revolution frequency f_{rev} up to the integer multiple of a harmonic number h

$$f_{rf} = h f_{rev}. \tag{3.1}$$

The required frequency variation during proton acceleration from injection (planned around 10 GeV) to top energy played a big role in the choice of cavity type[1]. As the top energy of 300 GeV is very high, the relative frequency swing for acceleration from the injection energy of 10 GeV can be calculated with the following approximate formula to only

$$\frac{\Delta f_{rf}}{f_{rf,top}} \approx 1 - \beta_i = 1 - \sqrt{1 - 1/\gamma_i^2} = 0.44\%\,, \tag{3.2}$$

with the RF frequency at top energy $f_{rf,top}$, the particle velocity β_i at injection relative to the speed of light and the corresponding relativistic Lorentz factor γ_i. At an operating frequency of 200 MHz this necessitates a bandwidth of 880 kHz of the accelerating structure.

For the case that standing wave resonant cavities are employed, their quality factors have to be much larger than the inverse of the frequency swing for reasonable power consumption. This means that the resonant frequency of such cavities needs to be constantly tuned during the ramp. Mechanically tuned cavities by means of a piston tuner were studied in detail and seriously considered for the SPS [37]. As the required frequency swing is small and due to other advantages explained in the following they were however dropped in favour of a fixed-tuned wideband system [36].

If a small phase slip between particles and accelerating wave is allowed, a travelling wave structure as described in Section 2.3 can easily provide the required bandwidth. The main advantage of such a structure is its high reliability due to the absence of any moving parts. Interventions on e.g. mechanical tuners employed in resonant cavities are undesirable firstly in view of radioactive contamination if a fast intervention is required. In case of a necessary replacement of the tuner the loss of vacuum comes along with an undesired down-time of the accelerator.

[1] As already mentioned, in the accelerator jargon, any system with the purpose of particle acceleration is often simply designated as cavity for convenience. Also travelling wave structures are therefore often somewhat incorrectly called travelling wave cavities.

At first sight a disadvantage of TWSs is the large power consumption compared to standing wave cavities [36]. However, this fact becomes negligible for high beam intensities with strong beam loading which changes the spatial distribution of electric field along the structure, see Eq. (2.28). A TWS then has the particularity that most of the additionally required power for restoring the accelerating field to its desired value does not equal the beam power but stems mostly from a decrease of the power that is otherwise lost in the terminating load. The beam induced-field is only at the centre frequency of the TWS 180° out of phase to the field induced by the generator and purely decelerating. For most of the accelerating cycle though, the required compensation depends on the stable phase angle as well as the particular phase-slip between particles and wave. Compensation can mostly be achieved by a mere phase shift and a slight increase of the input power [36]. The efficiency of a travelling wave system therefore rises rapidly with increasing beam intensity and the higher initially required power compared to standing wave cavities becomes less and less important. A large amount of additional power has to be installed anyway just to compensate the beam loading during a short time of the acceleration cycle and the power consumption for acceleration becomes relatively small. It is shown in more depth in [36] that the overall power consumption of a travelling wave accelerating system can in fact be made superior to standing wave cavities. As power source and TWS can simply be connected by a matched transmission line of arbitrary length (not taking losses into account), it is also possible to house the necessary power plants on the surface far away from the structure (at least 60 m in case of the SPS). Here, the sources are accessible for maintenance and possibly an expansion due to increased power demand during operation of the accelerator. For an accelerator of increasing energy and intensity this is a very valuable feature.

3.2. Multi-Stem Drift Tube Structures and Transverse Stem (TS) Resonances

The travelling wave accelerating structure of the SPS was chosen to be of the multi-stem drift tube type. Contrary to the Alvarez accelerator, each drift tube is supported by two stems with large diameter at an opening angle of 180°. In addition, the so-called stem passband created by this periodic loading is used for particle acceleration and not the TM_{01}-band. An extensive theory on multi-stem structures published in [14] studies the influence of different stem configurations, like the number of stems, their relative angles and thickness, on the cutoff frequency of the stem-passband which lies below the TM_{01}-band in frequency. The original intent of this study was to obtain the optimum stem configuration for confluence of the stem- and the TM_{01}-passband in standing-wave LINACs designed for various proton energies in the TM_{010}-mode (for notation see below). During the experimental verification of these multi-stem structures however, it became soon evident that the mode profile of the stem-passband itself also features a strong axial electric field that can directly be used for particle acceleration. The stem structure of the SPS is operated in this fundamental stem mode and not in the TM_{010}-mode. Consequently, no effort was undertaken to bring the stem- and the TM_{01}-passband into confluence on the SPS structure. Eq. (A.12) suggests that a TWS should have an R/Q as large as possible to be efficient. By careful optimisation of

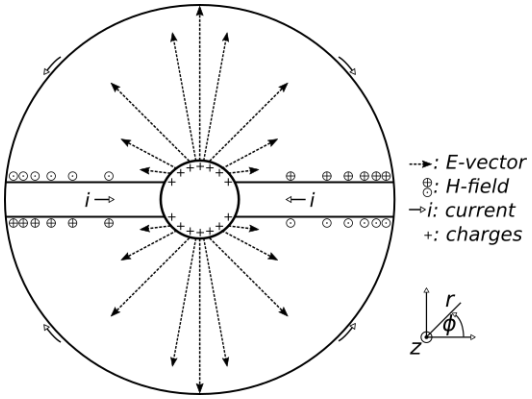

Figure 3.1.: Outline of TS_{11} field distribution in a two-stem (180°) drift tube structure. The vectors represent the field strength and orientation of the electric field E which does end on the cavity wall.

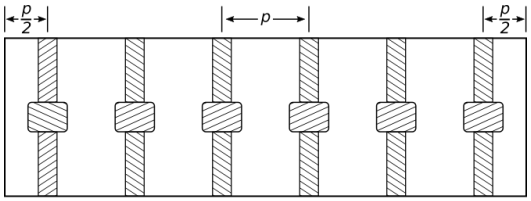

Figure 3.2.: Cross-section of a cavity tank periodically loaded with two-stem (180°) and drift tube assemblies.

the stem-loaded structure, a much larger value of 611 Ω/m could be obtained compared to e.g. an ordinary disc loaded structure for which $R/Q \approx 250\,\Omega/\mathrm{m}$ at β=1 and 200 MHz [27, 36].

The conventional TM and transverse electric (TE)-passbands of the uniform cylindrical waveguide or cavity also exist in the stem-loaded structure. As discussed in many textbooks, the modes can be identified by an azimuthal (m), a radial (n) and a longitudinal (l) index accounting for the number of local field zeros in the respective direction. With this, modes are typically designated as TX_{mnl}. Let us now determine the nature of the modes associated with the transverse stems and see if we can conveniently express also their field profiles with above naming convention. The stems behave as transverse resonators associated to conduction currents flowing along the stems. For symmetry reasons, the currents flow in opposite directions and the magnetic field around the stems is oriented as shown in Fig. 3.1. As a result, the drift tube will carry a net charge creating a transverse electric field to the outer cavity wall in the plane of the stems. The displacement current associated to this electric field flows via the outer cylinder back to the stems. To obtain the opposing field maxima at the azimuthal positions $\phi = 0, 180°$, the longitudinal component of the magnetic field H_z will vary azimuthally with $\cos m\phi$. The dominant resonance has the index $m = 1$ and higher order resonances are only possible with uneven m. Similarly, the radial component of the electric field E_r follows $\sin m\phi$ to comply with the boundary conditions. As for the common TE- and TM-modes, also the longitudinal component of the magnetic field H_z of the stem modes varies radially with the m-th order Bessel function of the first kind $J_m(\frac{\omega_0}{c}r)$ [14], with ω_0 the 0-mode frequency of the stem resonance. This also determines the current distribution along the stems. For the dominant, fundamental stem mode with the lowest resonance frequency the radial index is $n = 1$ since there is no change of sign in the radial variation of the fields. Let us designate this mode therefore by TS_{11}. Its field and current distributions are sketched in Fig. 3.1.

The cutoff frequencies (0-modes) of stem-passbands can be estimated by treating the structure as a coaxial waveguide with the drift tubes forming the inner conductor [14]. According to this theory the cutoff frequency of the lowest stem-passband can be increased either by a larger number of stems or an increased stem diameter. Confluence however can not be obtained with any two-stem configuration so that the accelerating passband in the SPS structure is below the cutoff of the uniform waveguide. The fields of a single stem-and-drift-tube assembly would therefore decay exponentially along an otherwise unloaded guide. However, by loading the guide with stems periodically, a coupled system with an associated passband is created.

A cavity tank as shown in Fig. 3.2 is obtained by terminating a piece of circular waveguide loaded with N stem assemblies by conducting end-plates. In such a tank of coupled resonators, N discrete standing-wave stem modes can be excited in the lowest passband, i.e. TS_{111}, TS_{112}, $\ldots \mathrm{TS}_{11\mathrm{N}}$. Each normal mode of the coupled system has a characteristic resonant frequency and field pattern with relative amplitudes and phases for the different resonator cells. For the general case of N coupled resonators, the properties of the normal modes can be determined by solving an Eigenvalue problem of coupled electrical circuits [38]. The result must however be adapted to the stem-loaded structure in which the longitudinal variations of the E_r and E_z field components for the respective standing wave modes are of special interest to us. The stem-loaded structure is terminated in two half end-cells and the resonating elements (the stem-cells) are not identical with the accelerating gaps, as it is e.g. the case in a disc-loaded structure. From textbooks we know that the longitudinal periodicity is half a guide wavelength $\lambda_g = {}^{2\pi}/_{k_z}$, where

$$k_z = \frac{l\pi}{L} = \frac{l\pi}{Np}. \tag{3.3}$$

The index l accounts for the number of half period oscillations over the total length L of the cavity with a cell length of p. Taking also the boundary conditions at the end-plates into account, the position dependence of the longitudinal electric field E_z in a stem-loaded structure is most conveniently expressed as $\cos k_z z$ and the radial electric field E_r follows $\sin k_z z$.

In the stem 0-mode with zero phase shift per cell, all stems carry the same currents, identical in both amplitude and phase. Imagine that the metallic end-plates are placed in the planes of the first and last stem assemblies, shorting these cells and leading to zero currents along the stems. For the 0-mode this means that the currents in all other cells are zero as well. In fact, this holds also true if the end-plates are placed in any other symmetry plane of the cells so that the stem 0-mode can never be excited in a typical tank, as e.g. the one shown in Fig. 3.2. In addition, the drift tubes are charged equally in the 0-mode so that there is almost no longitudinal electric field created on the axis of the structure for this mode. This will not be the case for modes with non-zero phase shifts per cell. On the contrary, a strong electric field is generated on-axis which can be used for particle acceleration.

The field dependencies of the TS modes obtained by treating the stems as transverse resonators are summarised in the following:

$$\begin{aligned} E_r(\phi) &\propto \sin m\phi \\ H_z(\phi) &\propto \cos m\phi \qquad\qquad m = 1, 3, 5, \dots \\ H_z(r) &\propto J_m(k_c r)\,. \end{aligned} \tag{3.4}$$

For each standing-wave mode l in a stem-loaded cavity tank as shown in Fig. 3.2, the relative transverse field strengths at the positions of the stems are

$$E_r(z) \propto \sin \frac{l\pi}{Np} z\,, \qquad z = \frac{p}{2} + np \quad \text{for} \quad n = 0, \dots, N-1. \tag{3.5}$$

The relative longitudinal field strengths at the positions of the gaps are

$$E_z(z) \propto \cos \frac{l\pi}{Np} z\,, \qquad z = np \quad \text{for} \quad n = 0, \dots, N. \tag{3.6}$$

The typical nomenclature to identify each mode is the quantity $l\pi/N$ with $l = 1, \dots, N$, which is the phase shift per cell.

3.3. System Overview

The unit-cell for the simulation of the periodic parallel stem structure used in the SPS is shown in Fig. 3.3. In addition to the drift tubes and stems it also consists of pedestals on which the stems

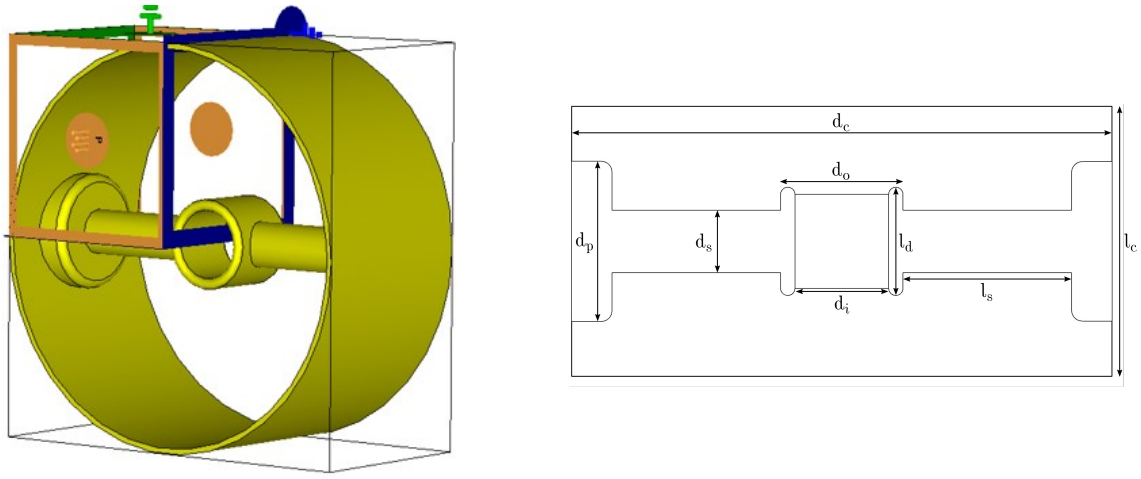

(a) Simulation model with periodic boundaries (orange) and symmetry planes (blue).

(b) Cross section.

Figure 3.3.: Unit-cell of SPS parallel stem structure.

are suspended. The pedestals are included in the design for constructional and tuning reasons. An

adjustment of the group velocity as suggested in [39] is not observed, as the presence of the pedestals merely shifts the whole FPB to higher frequencies by an amount independent of frequency. Models for EM simulations were drafted from mechanical drawings. The dimensions of the unit-cell are $l_c = 374\,\text{mm}$, $l_s = 321\text{mm}$, $l_d = 150\,\text{mm}$, $d_c = 750\,\text{mm}$, $d_s = 86.5\,\text{mm}$, $d_i = 130\,\text{mm}$, $d_o = 170\,\text{mm}$ and $d_p = 221\,\text{mm}$. The stem length l_s is used for the tuning of the structure to compensate fabrication tolerances; refer also to Section 3.5 in this regard. The diameters of the two pedestals differ by design by one millimetre for assembly reasons. In first simulations it could be shown that this difference has only a negligible impact on the longitudinal impedance and behaviour of the structure. Therefore, the pedestal diameter given above was used for both pedestals for all simulations. In this case, the structure is horizontally symmetric and hence allows the use of a vertical symmetry plane in many simulations which results in much shorter runtimes. This is especially valuable for time intensive wakefield simulations of the large 33-cell structures equipped with numerous HOM couplers. The validity of the simulation models will be confirmed throughout this thesis by comparison to RF measurements and analytic models, most notably those already introduced in Section 2.4.

The main components needed for the operation of each accelerating structure are outlined in the block diagram of Fig. 3.4. Also refer to Fig. 1.16 for illustration. The TWSs are fed via

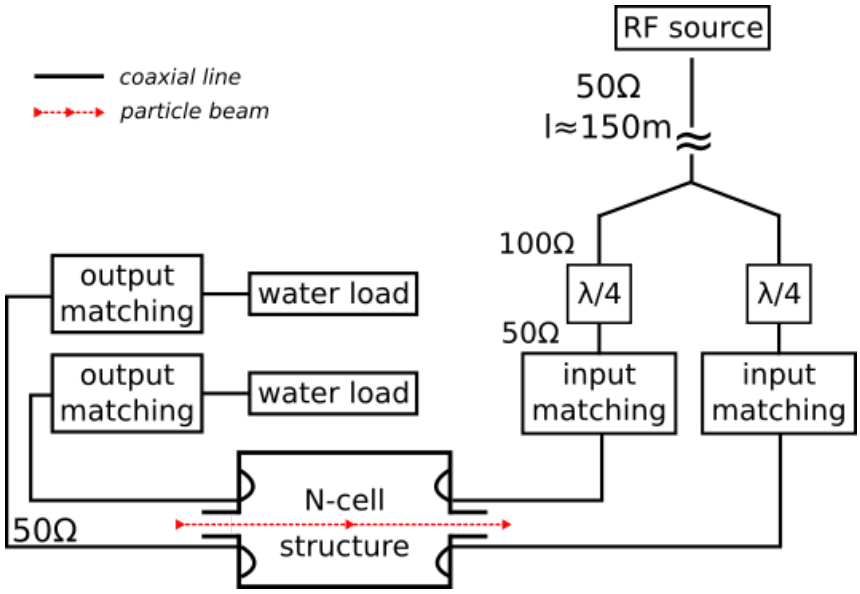

Figure 3.4.: System overview of a TWS in the SPS.

rigid 50 Ω coaxial lines with an outer diameter of 345 mm and a length of more than 100 m each. The structures must be fed axis-symmetrically to avoid transverse deflections of the beam. For this purpose the large coaxial lines are split up as illustrated in Fig. 3.4 and the inner conductors end in coupling loops on the pedestals of the first half cells, see Fig. 3.5. The coupling loops are henceforth called fundamental power couplers (FPCs). The FPCs are presently undergoing a redesign to cope with the increased input power and constrained space requirements within the

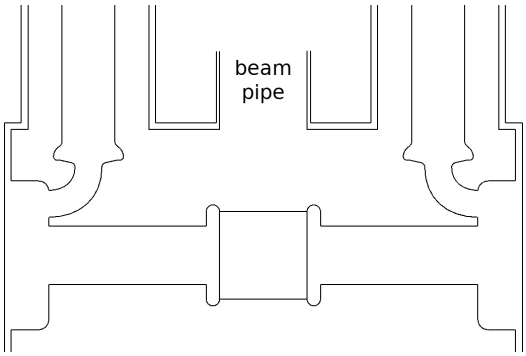

Figure 3.5.: Cross section of fundamental power couplers (FPCs) in use until LS 2.



Figure 3.6.: Inside view of the parallel stem accelerating structure. ©CERN

context of the LIU-project. The same FPCs are also used at the RF end of the structure to connect a coaxial water load in which the travelling wave is terminated. The presence of the FPCs detunes the first and last half cells so that the effective length for particle acceleration of a N-cell structure, also called the interaction length, is reduced by one full cell to $(N-1)l_c$. An inside view of the accelerating structure is shown in Fig. 3.6. The cylindrical envelope is of oxygen-free high-conductivity (OFHC) copper in a steel envelope [27]. For manufacturing and handling reasons the TWSs consist of 11-cell sections, of which one is shown in Fig. 3.7. The drift tube and stem



Figure 3.7.: Eleven-cell section of the TWS with access ports on top of each cell used for HOM damping, ten lateral ports in each accelerating gap used for low-level RF systems and three vacuum pumping ports (VPPs) at the bottom.

assemblies are installed by inserting them from the side as one unit into the envelope. RF contact between outer wall and pedestals is ensured via RF springs all around each pedestal.

A direct connection of the amplifiers and the termination to the loaded waveguide structure would not result in a pure travelling wave. Matching networks are employed at the input to avoid reflections back towards the RF source and at the output of the structure to ensure a good matching of the terminating water load, see Fig. 3.4. Another important purpose of the matching networks

is to provide damping of adjacent modes in the FPB which are excited by the beam due to the coupling impedance. A broadband match ensures that the water load not only terminates the RF input but also the neighbouring, high impedance modes. No beam power will run towards the RF source as the beam induced field is zero at the RF input end of the structure, cf. Eq. (2.28). The FPCs in combination with the matching can ensure a travelling wave operation in a bandwidth of a few Megahertz around the operating frequency. Refer to Sections 3.6 and 3.8.1 for more details.

Besides, each TWS is equipped with low-level RF feedback and -forward systems not shown in Fig. 3.4 to mitigate the effects of beam loading [40]. The TWS is cooled with water circuits on the outer cylinder and in the stems, see Fig. 3.7, with a nominal water temperature of 20°C and a water flow of around 550 $^{l}/_{\text{min}}$.

3.3.1. Brief Overview on Present HOM couplers

As is the case with any cavity or waveguide, the TWS also supports HOMs which can be excited by the passing beam. The FPCs are not intended to couple to the HOMs and do not provide significant damping for them. The cutoff frequency of the first HOM on the coaxial feeder lines that are directly attached to the TWSs is calculated to 739 MHz and of the cylindrical, on-axis beam pipe shown in Fig. 3.5 to 1.32 GHz. The most deteriorating TS_{31}-HOMs around 630 MHz can therefore be considered as cavity resonances and of standing wave type.

Figure 3.8a shows the detailed mechanical model of the coaxial coupler with an electric pickup which is presently used to damp HOMs in the TS_{31}-band. A ceramic window in the 50 Ω coaxial

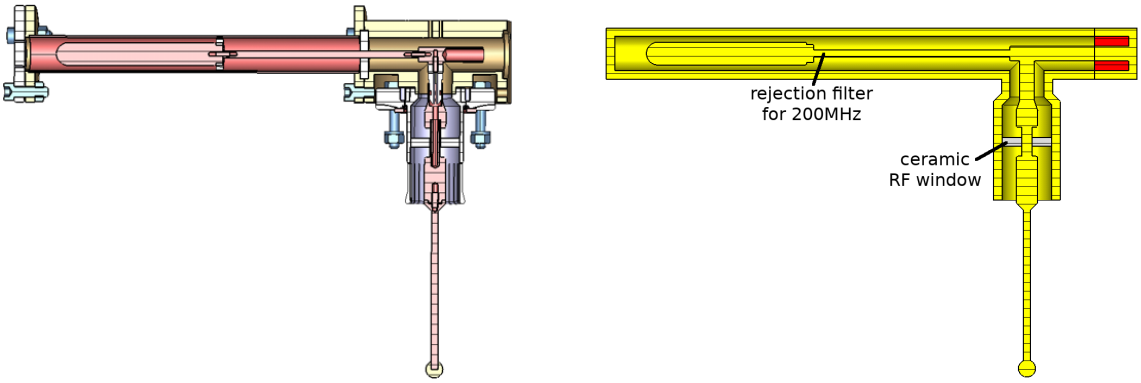

(a) Mechanical model.

(b) EM simulation model with the resistive load (red) realised via a lossy PML.

Figure 3.8.: Coaxial coupler with electric pickup for damping of longitudinal TS_{31}-HOMs at around 630 MHz.

line is permeable for the RF, but separates the evacuated cavity from the filter part which is at ambient pressure. The HOMs are terminated in a 50 Ω resistive load which is not shown in Fig. 3.8a. Modelling of the high mechanical detail is not required and a burden for EM simulations which

is why the model was reduced to the simplified version shown in Fig. 3.8b containing only those elements influencing the RF properties of the coupler significantly. A lossy perfectly matched layer (PML) implemented via a lossy material (red) also shown in Fig. 3.8b is used to simulate the resistive load. Refer to Section 3.7.2 for more details on this. Due to the similar field profiles of the fundamental TS_{11}- and the higher order TS_{31}-modes, the HOM coupler must feature a notch filter at 200 MHz to avoid damping of the accelerating mode. The two-element notch filter shown in Fig. 3.8 short circuits and reflects the fundamental mode at 200 MHz while also behaving as an open circuit at 630 MHz. A more detailed analysis of the coupler and its performance is carried out throughout this thesis. No documentation on the design of this HOM coupler and the reasoning behind its deployment on the TWSs is available from the time of its development in 1977.

Four of the TS_{31}-mode couplers were placed regularly on each section of the four TWSs in use until LS 2. A typical damping configuration including also two more coupler-types to mitigate transverse HOMs is illustrated in Fig. 3.9. The access ports on top of each cell are also used

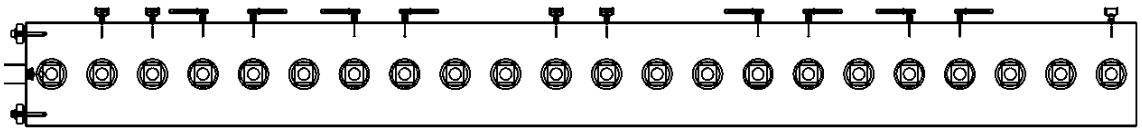

Figure 3.9.: Schema of the damping configuration on a 44-cell structure (centre-symmetric) showing the HOM coupler locations for damping of the 630 MHz longitudinal, the 938 MHz transverse and the 460 MHz transverse HOMs (on the end-plates). The 938 MHz coupler locations in cells 2, 3, 11, 12 and 22 are merely exemplary.

for the damping of a transverse resonance at 938 MHz via loop coupling to the magnetic field, see [41]. The electric pickup of the TS_{31}-mode coupler and the magnetic loop of the 938 MHz transverse mode coupler can also be seen in Fig. 3.6. A third type of HOM coupler for damping of transverse HOMs at 460 MHz with a horizontal, dipole-like antenna is in use on the end-plates of each structure. The two transverse HOMs mentioned before can drive the beam unstable in the horizontal plane.

3.4. Unit-Cell Simulations

3.4.1. Dispersion in the 200 MHz FPB and TS_{11}-Mode Field Profiles

The dispersion characteristics of an infinite periodic structure can be conveniently obtained from the simulation[2] of its unit-cell with periodic boundaries. These boundaries with definable phase advance are the application of Floquet's theorem in Eq. (1.6) and result in a small, convenient simulation, see Fig. 3.3a. For axisymmetric structures and depending on the mode type of interest,

[2]EM simulations throughout this thesis are conducted with the two codes CST [42] and the Advanced Computational Electromagnetic 3D Parallel Simulation Suite (ACE3P) [31].

the size of the problem can be further reduced by using transverse electric or magnetic symmetry planes. The transverse stem modes can be obtained by deploying magnetic symmetries as shown in Fig. 3.3a.

Figure 3.10 shows the first three passbands in the SPS 200 MHz TWS obtained from such unit-cell simulations. In addition to the usual passbands of the unloaded, uniform waveguide, a

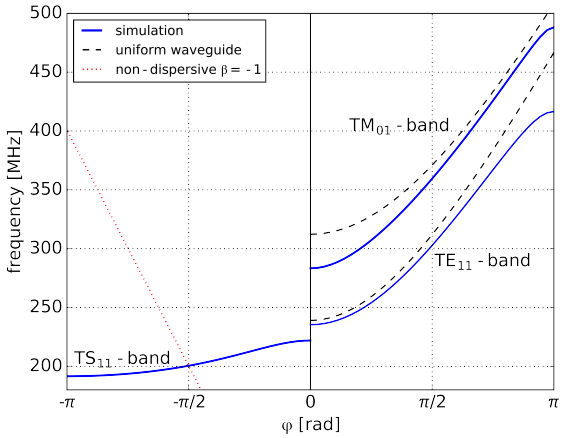

Figure 3.10.: Fundamental space harmonics of the three lowest passbands in the SPS 200 MHz TWS obtained from unit-cell simulations with periodic boundaries. The characteristics of a non-dispersive wave with relative phase velocity β representing the particle beam is shown as well (dotted). The analytic calculation of the TE_{11} and TM_{01} bands in the corresponding unloaded circular waveguide is given as reference (dashed) [9].

backward-wave passband is created below the cutoff frequency of the unloaded guide. It is called the stem-passband as it results from the coupled stem resonators. Figure 3.10 also includes the theoretical characteristics of a non-dispersive wave as it would exist in free space with a relative phase velocity of β=-1. This often called 'lightline' represents the particle beam and Fig. 3.10 suggests that the beam is synchronous with the stem mode at around 200.222 MHz having a $\pi/2$ phase advance per cell. The $\pi/2$-mode was chosen for operation as it features high shunt impedance and nearly the desired group velocity in the parallel stem structure [39]. As to why the structure is tuned to the specific frequency of 200.222 MHz refer to Section 3.5. The stem length of l_s= 321 mm results in the correct tuning in simulations.

The R/Q of the structure at the travelling-wave operating mode is simulated to 626 Ω/m, the quality factor to 22800, the attenuation length to 515 m and consequently the series impedance is 27.8 $k\Omega/\mathrm{m}^2$. These values are only slightly higher than those given in [27] and to the authors understanding these were obtained from RF measurements on a two-cell prototype, see e.g. [43]. Despite the small discrepancy, this suggests additional losses in the actual structure which are not modelled by the simulation. Candidates are the RF spring contacts surrounding each pedestal, which are hard to model and infeasible to simulate. An electrical conductivity of $5.8 \cdot 10^7$ S/m for the OFHC copper is used throughout all simulations. The impedances of the TWS will be slightly

overestimated by the simulations, however regarding the relative, additional HOM-mitigation this is of no relevance.

The surface current and the electric and magnetic field profiles for the $\pi/2$ stem mode are reported in Fig. 3.11. They are in good agreement with the general characteristics already obtained in Section 3.2 by treating the stems as transverse resonators.

An appropriate equivalent circuit to model the FPB is the one introduced in Fig. 1.11 for resonantly coupled resonators. An adapted version of the circuit is shown in Fig. 3.12. Every cell includes two resonators, the stem ($\omega_s = 1/\sqrt{L_s C_s}$) and the drift tube $\omega_d = 1/\sqrt{L_d C_d}$ resonator which model the stem- and the TM_{01}-passbands respectively. More details on this equivalent circuit are given in Appendix B together with the derivation of its dispersion equation

$$\sin^2 \frac{\varphi}{2} = \frac{L_d}{L_s} \left(\frac{\omega^2}{\omega_s^2} - \frac{1 - k_s \cos\varphi}{1 - k_s^2} \right) \left(1 - \frac{\omega_d^2}{\omega^2} + k_d \cos\varphi \right), \tag{3.7}$$

where

$$\omega_d = \frac{1}{\sqrt{L_d C_d}} \qquad \omega_s = \frac{1}{\sqrt{L_s C_s}} \qquad k_d = \frac{M_d}{L_d} \qquad k_s = \frac{M_s}{L_s}. \tag{3.8}$$

The 0-mode frequencies of the drift tube and stem passbands are

$$\omega_{d,0} = \frac{\omega_d}{\sqrt{1 + k_d}} \qquad \omega_{s,0} = \frac{\omega_s}{\sqrt{1 + k_s}}. \tag{3.9}$$

respectively.

3.4.2. Impedance Calculation in the FPB of 33-, 44- and 55-Cells

The phase and group velocities in the frequency range of the fundamental passband (FPB) are easily calculated from its simulated dispersion curve with Eqs. (1.4) and (1.5) respectively and they are plotted in Fig. 3.13. Note the opposite signs due to the backward characteristic of the stem passband. The respective values at 200.222 MHz are $v_p \approx c$ and $v_g = 0.09466c$. The latter is in excellent agreement with the value reported in [27]. With the so obtained frequency dependent group and phase velocities we can calculate the forward and beam coupling impedances of a TWS with an arbitrary number of cells in the frequency range of the FPB. The forward impedance Z_{rf} of 33-, 44- and 55-cells is plotted in Fig. 3.14 according to Eq. (2.24). Peak impedance is provided by the structures at the synchronous frequency for which the phase slip between EM wave and particle beam is zero along the whole length of the structure. Note the asymmetric distribution of the zeros about the synchronous frequency and the more broadband characteristic of shorter structures. The beam coupling impedance Z_b of 33-, 44- and 55-cells is plotted in Fig. 3.15 following Eq. (2.30). Note the considerably lower peak coupling impedance of 33-cell structures compared to that of 55-cells which is part of the motivation to change the configuration of the TWSs [20].

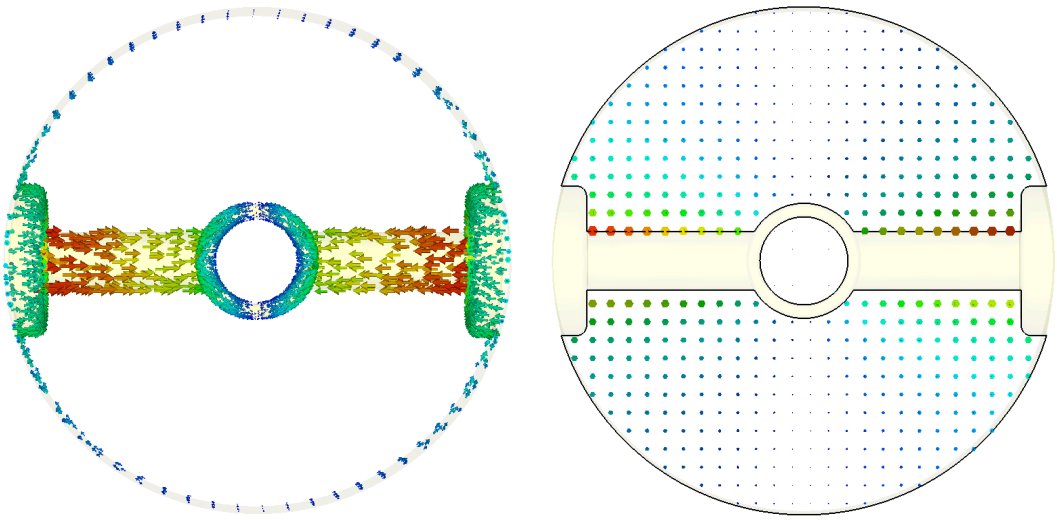

(a) Surface currents.

(b) Magnetic field.

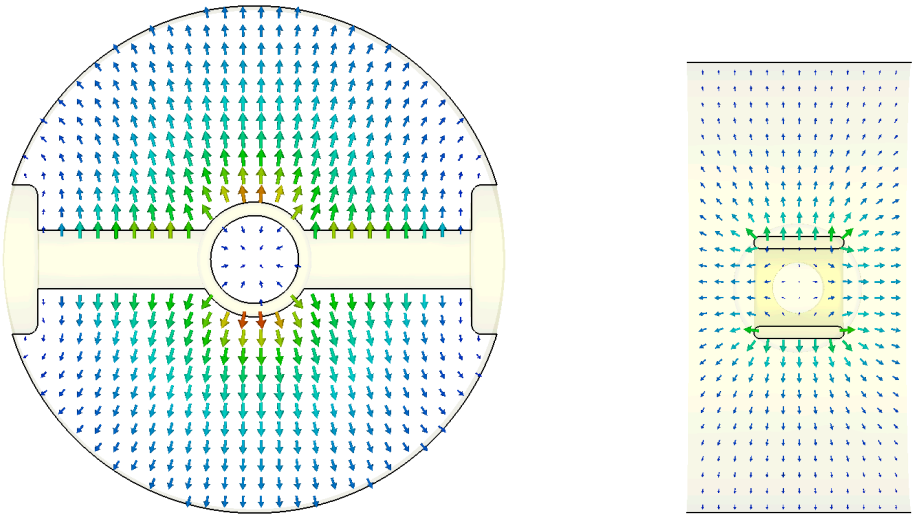

(c) Electric field.

(d) Electric field.

Figure 3.11.: EM characteristics of the $\pi/2$ accelerating mode on cross sections of a unit-cell, obtained with CST. Color-coding of field-strength is on a linear scale.

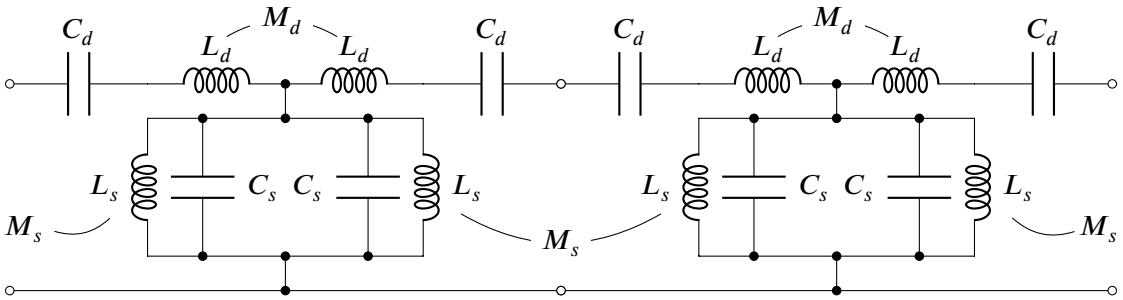

Figure 3.12.: Periodic equivalent circuit for multi-stem drift tube structures, see Appendix B for more details.

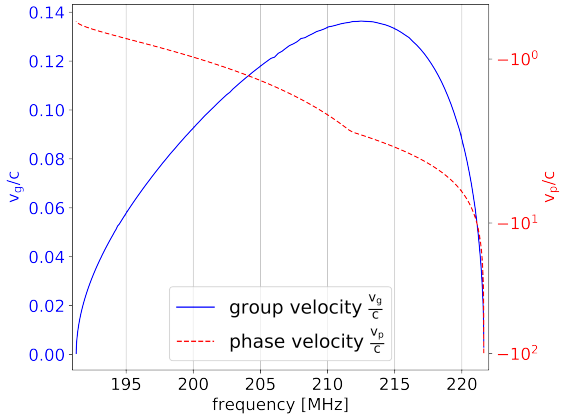

Figure 3.13.: Group velocity v_g and phase velocity v_p of the TWS in the frequency range of the FPB.

3.4.3. TS_{31}-HOM Dispersion Around 630 MHz

The unit-cell approach can also be used for a first characterisation of the passbands around 630 MHz, which is known to be the frequency range of HOMs responsible for the beam instability. This will serve as a basis for the detailed identification of the deteriorating high-impedance modes in Chapter 4 later on. The dispersion curves of the TWS in the 630 MHz frequency range are shown in Fig. 3.16 and were reported in **[44]**. Here, all passbands as well as the 'lightline' are folded into the interval $0<\varphi<\pi$. The beam is actually synchronous with the $n = -1$ space harmonics of the HOMs (refer to Fig. 1.7). It is helpful to first briefly study the dispersion characteristics for the simpler case in which the pedestals are not included in the structure, meaning that the stems are connected directly to the outer wall with constant diameter, see e.g. Fig. 3.1. By its EM characteristics shown in Fig. C.1 we identify the lower passband in Fig. 3.16 as the TS_{31}-band. This is the first higher mode of the fundamental TS_{11}-band at the third harmonic frequency. The current along the stems now shows a zero, see Fig. C.1a, and the analysis in Section 3.2 suggests a cur-

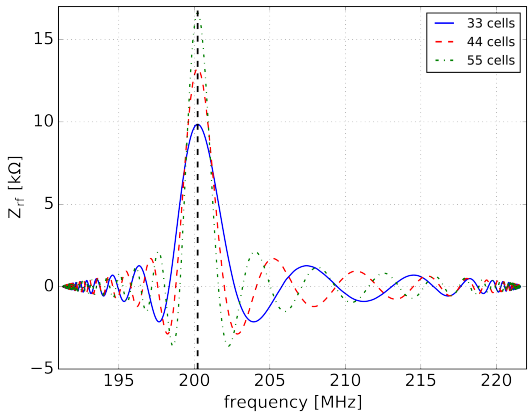

Figure 3.14.: Forward transfer impedance Z_{rf} of 33-, 44- and 55-cell TWSs tuned to 200.222 MHz in the frequency range of the FPB.

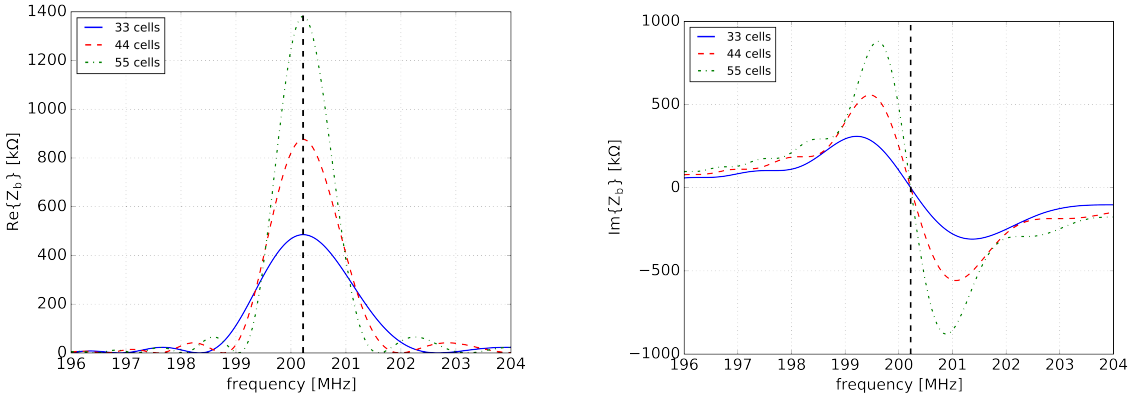

(a) Real part.

(b) Imaginary part.

Figure 3.15.: Beam coupling impedance Z_b of 33-, 44- and 55-cell TWSs tuned to 200.222 MHz in the frequency range of the FPB.

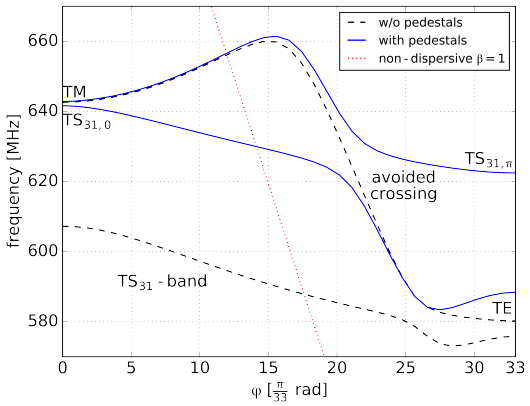

Figure 3.16.: Dispersion curves of HOMs in the 630 MHz range obtained from unit-cell simulations with transverse magnetic symmetry planes for the parallel stem structure without (dashed) and with pedestals. The mode types in the passbands at the respective phase advances φ are indicated. The 'lightline' is shown as well (dotted).

rent distribution following the third order Bessel function. The second harmonic of the stem band can not exist in the structure due to the azimuthal boundary conditions. The upper passband in Fig. 3.16 for the case without pedestals is a TM-mode which can not clearly be identified due to the complicated periodic loading of the waveguide. The change in sign of group velocity within this band suggests that this mode is coupled with another mode [45]. And indeed, when carefully studying the field profiles within this passband one observes a gradual change of the mode type in going to larger phase advances φ. The 0-mode is of TM-type, whereas the π-mode is of TE-type, cf. Fig. C.2. Note that the coupled TE-band is not shown in Fig. 3.16.

For the case of the full SPS parallel-stem structure including the pedestals we make two observations. First, the TS_{31}-band is shifted to higher frequencies. This is because the pedestals are placed in a region where the TS_{31}-modes feature strong magnetic field.[3] The second observation is a phenomenon which is quite well known in the literature under the name 'avoided crossing' of passbands [45, 46]. If two modes are coupled via the periodic obstacles which load the waveguide, their passbands do not cross in the dispersion diagram as it would be the case if they were uncoupled. The 'avoided crossing' can be observed in Fig. 3.16 around $\varphi = 110°$ ($\approx {}^{20\pi}/_{33}$) and the behaviour corresponds to the case that the passbands have the same sign of group velocity as described in [45]. Coupling between the two passbands is confirmed when looking at the field profiles. The 0- and π-mode field profiles of the lower passband are shown in Fig. C.3. While the 0-mode again shows the TS_{31} characteristic, the π-mode of this band shows the TE-mode characteristic of the mode already coupled to the upper passband in the case without pedestals. The 0-

[3] Consider Slater's formula for a boundary perturbation of cavities [10], indicating the frequency shift:

$$\frac{\omega - \omega_0}{\omega_0} \approx \frac{\int_{\Delta V} \left(\mu |H_0|^2 - \epsilon |E_0|^2\right) dv}{\int_V \left(\mu |H_0|^2 + \epsilon |E_0|^2\right) dv}$$

and π-mode of the upper passband however show the TM and TS_{31} characteristics respectively as shown in Fig. C.4. This means that the potentially harmful field characteristic of the TS_{31} mode with strong beam coupling impedance makes a gradual transition from the lower to the upper passband, which should be kept in mind for the later improvement of the HOM damping. Around 630 MHz, HOMs from two different passbands exist in the structure which are both of the TS_{31} type (HOMs with $\approx {}^{15\pi}/_{33}$ phase advance from the lower passband and $\approx {}^{22\pi}/_{33}$ of the upper band in Fig. 3.16). The 'lightline' in Fig. 3.16 suggests that the beam is synchronous with the stem mode at ${}^{14\pi}/_{33}$ phase advance and this mode is therefore expected to have largest beam coupling impedance. And indeed, from the additional analysis in Chapter 4, it will become clear that the most deteriorating HOMs around 630 MHz in the SPS 33-cell structure are those with the TS_{31} characteristic and a ${}^{14\pi}/_{33}$ and ${}^{15\pi}/_{33}$ phase advance respectively.

Physically, the coupling between the bands can be explained by a cross coupling between the drift tube and the stem resonator. The equivalent circuit presented in Fig. 3.12 for modelling the FPB could be extended in this regard by using an additional mutual coupling and possibly with an additional resonator chain for the coupled TE-mode. Overall, it is clear that the mode coupling around 630 MHz is a complicated mixture, which is typical at higher frequencies in a waveguide with periodic loading.

3.5. Tuning

The TWS is a fixed-tuned, broadband accelerating system. Due to its broadband characteristic, very precise tuning is not as crucial as for standing wave cavities. The TWS features peak forward impedance at its synchronous frequency for which the phase slip between the beam and the travelling-wave ${}^{\pi}/_{2}$-mode along the structure is zero. It is not immediately evident to which beam energy the synchronous frequency of the structure should be tuned to, as the available accelerating voltage for the proton LHC beam is a limitation at both the start of the magnet ramp (injection energy 26 GeV/c with RF frequency 200.265 MHz) and at flat top (extraction energy 450 GeV/c with RF frequency 200.394 MHz). Tuning to the centre frequency of the ramp suggests itself as well.

However, a different criterion was used for the initial tuning in the '70s. At this time, the injection energy was lower than today and in addition different machine optics were used. As a result, the transition energy in the SPS was crossed during the first years of operation. This is no longer the case today. At transition, the stable phase angle ϕ_s needs to undergo a sudden jump from the rising to the falling edge of the accelerating voltage. It is therefore advantageous if the synchronous frequency falls onto the transition frequency to reduce the demand on the final amplifier stages and machine operation at this critical point in the ramp. In this case the amplifiers merely need to undergo a phase jump while the RF magnitude can be kept constant and an abrupt change in power, required to compensate beam loading, is then not needed. The situation is illustrated in the vector diagram of Fig. 3.17. Only at the synchronous frequency the beam current and beam loading vectors have exactly opposite sign. And therefore only at this frequency the vector addition of V_{rf} and

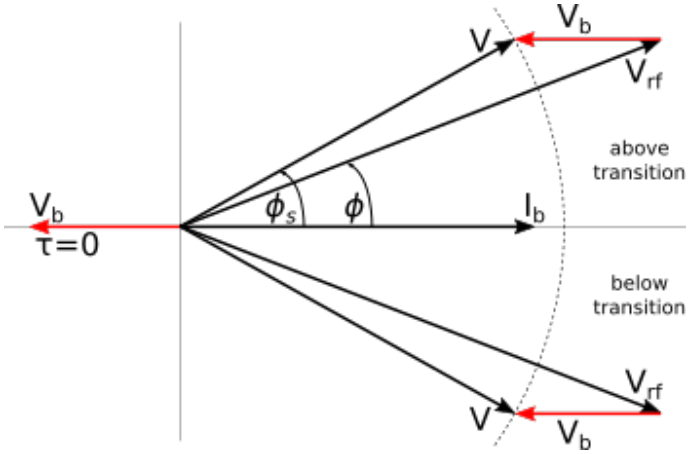

Figure 3.17.: Vector diagram of Eq. (2.31) with V_b=-$Z_b I_b$ at transition crossing for the case that the TWS is tuned to the transition frequency. A phase jump from $-\phi$ to $+\phi$ by the RF source is sufficient to set the desired stable phase angle ϕ_s under beam loading. A change in RF amplitude is not required as the beam loading vector V_b is exactly opposite to the beam current I_b in this case.

V_b has a constant amplitude during a phase jump to the falling edge of the total voltage V seen by the beam. This is why the $\pi/2$-mode of the TWSs was tuned to the former transition frequency of 200.222 MHz. Note that today, this is well below even the injection frequency of the proton LHC beam.

It would be uneconomical to manufacture the accelerating structures with tight tolerances to achieve the desired synchronous frequency immediately. Instead it is common to relax on the manufacturing tolerances and to compensate for the errors in a tuning process later on. The cell tuning mechanism used for this purpose is the distance between the two pedestals of a cell or equivalently its stem lengths. The frequency dependence of the $\pi/2$-mode on the stem length around 200 MHz is

$$\frac{df_{\pi/2}}{dl_s} = -266\,\frac{\text{kHz}}{\text{mm}}\,.$$

The cell frequency is especially susceptible to the stem diameter d_s

$$\frac{df_{\pi/2}}{dd_s} = +451\,\frac{\text{kHz}}{\text{mm}}\,.$$

It is worthwhile to note that in fact the cell frequency depends linearly on all cell dimensions around 200 MHz. The tuning was carried out for each 11-cell section individually in the '70s. Not all cells of a tuned section must therefore have equal stem lengths. The $\pi/2$-mode frequency was interpolated from the 11 standing wave resonances in the FPB and corrected by adjusting a special set of 11 adjustable drift tubes. The section was then fitted with brazed drift tube assemblies of the appropriate stem lengths instead [27]. The dispersion curves of the three available spare sections of the 200 MHz structure and the tuning of the TWSs in use in the SPS until LS 2 are measured in detail in Section 5.2 and Section 5.5.2 respectively.

3.5.1. Frequency Dependence on Pressure and Temperature

The tuning procedure, but also RF measurements are often carried out in the lab frame with a non-evacuated cavity i.e. at potentially varying temperature and humidity levels. It is therefore necessary to convert the mode frequencies in the structure to its operating conditions, meaning when it is under vacuum and cooled via cooling circuits. The refractive index of a medium is defined as $n = \sqrt{\epsilon_r \mu_r}$ so that, with the refractive index of air at atmospheric pressure typically taken as n_{air}=1.0003 [47], the frequency in the evacuated cavity will be $f_{vac} = n_{air} f_{air}$.

As previously mentioned, the mode frequency of a cell in the TWS depends linearly on all cell dimensions around 200 MHz. Under the assumption that all parts of a cell are uniformly affected by a change in temperature dT, let us therefore estimate the change in frequency with the linear thermal expansion coefficient α of the cavity material. For the expansion dl of a cavity dimension the coefficient is defined as

$$\alpha = \frac{1}{l}\frac{dl}{dT}\,. \tag{3.10}$$

We are interested in the mode frequency $f_{vac}(T_0)$ of the cavity under vacuum and cooled with water at temperature T_0, but we measure the frequency $f_{air}(T)$ in air and at temperature T. With $dT = T - T_0$ we obtain the relation

$$f_{vac}(T_0) = \frac{n_{air}}{1 + \alpha(T_0 - T)} f_{air}(T) \tag{3.11}$$

to calculate the desired $f_{vac}(T_0)$.

The SPS TWS is made of OFHC copper in a steel envelope [27]. The linear thermal expansion coefficient of OFHC copper is reported as $\alpha = 17.7\,\frac{\mu\mathrm{m}}{\mathrm{m}\,^\circ\mathrm{C}}$ [48]. At 200 MHz this results in a frequency shift of $\pm 3.54\,{}^{kHz}/_{^\circ\mathrm{C}}$ which is in good agreement with the value of $\pm 25\,\mathrm{kHz}/\pm 7.5\,^\circ\mathrm{C}$ given in [27]. Note that for the required precision in our applications the influence of a change in humidity on the tuning can be neglected.

3.6. Matching

3.6.1. Consequences of RF Generator and Load Mismatch

Proper travelling wave operation and a waveguide-like behaviour of each accelerating structure is ensured by matching networks at the in- and output. The input network matches the TWS to the RF generator and avoids excessive reflection of power. A mismatch results in less power transfer to the TWS and consequently a lower accelerating voltage. The quality of the match can simply be measured by the input reflection coefficient S_{11}. With the series impedance R_2 and the input power P, we rewrite Eq. (2.21) for the voltage induced by the RF generator to

$$V_{rf} = \sqrt{R_2 P}\, e^{j\Phi}\, L\, \frac{\sin(\tau/2)}{\tau/2}\,. \tag{3.12}$$

The actual RF voltage taking the input-mismatch into account is then reduced to

$$\sqrt{1-(S_{11})^2}\,V_{rf}\,.$$

The output network matches the terminating load to the TWS, thus avoiding reflections at the end of the structure back towards the RF input. The consequence of a load mismatch is briefly studied in the following also with the goal of finding an appropriate criterion to assess the quality of the match. Consider the schematic of a TWS with spatial period p and load mismatch Γ at $z = L$ in Fig. 3.18. The generator injects the travelling wave

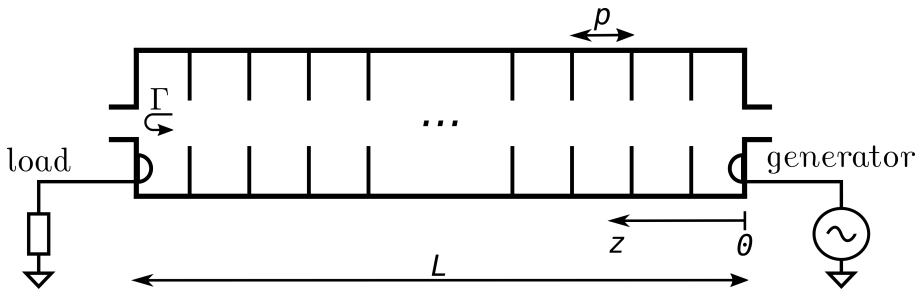

Figure 3.18.: Schematic view of a travelling wave system with load mismatch Γ and spatial period p.

$$E^+ = E_0\, e^{-jkz}$$

with wavenumber $k = {}^{\Delta\varphi}/_{p}$ into the N-cell structure. The wave reflected at the RF output at $z = L = Np$ is

$$E^- = \Gamma\, E_0\, e^{-jkL}\, e^{jk(z-L)} = \Gamma E_0\, e^{jk(z-2L)}.$$

We neglect attenuation and a re-reflection at the RF input which usually is a very good approximation since the structure is build for matching. For the case of a $\pi/2$-mode, we write the superposition $\Sigma = E^+ + E^-$ as

$$\Sigma_{\pi/2} = E_0\,(1-\Gamma)e^{-j\frac{\pi}{2p}z} + E_0\,2\Gamma \begin{cases} \cos\left(\frac{\pi}{2p}z\right) & \text{for N even} \\ -j\,\sin\left(\frac{\pi}{2p}z\right) & \text{for N odd}\,. \end{cases} \tag{3.13}$$

This is a forward travelling wave of reduced amplitude $E_0\,(1-\Gamma)$ with a superimposed $\pi/2$ standing wave of amplitude $E_0\,2\Gamma$. The $\pi/2$ standing wave also exists in a TWS with uneven number of cells N as we assumed no re-reflected wave. The phase of Γ will depend on the output matching network. If Γ is of zero phase at $z = L$, Eq. (3.13) shows that the standing wave has no net accelerating effect on the beam. Ignoring the anyway unwanted standing wave, the actual RF voltage $\tilde{V}_{rf}$ obtained taking the generator and load mismatch into account is

$$\tilde{V}_{rf} = \sqrt{1-(S_{11})^2}\,(1-\Gamma)\,V_{rf}\,. \tag{3.14}$$

A good match of a TWS to its load is more important than the input match. The so-called field flatness over all cells is therefore an important quality parameter for a travelling wave system. The $\pi/2$ standing wave manifests as a π-pattern with amplitude $E_0\,\Gamma$ on the modulus of the total field along the TWS, refer e.g. to Section 3.8.1.

3.6.2. A Direct Matching Technique for Travelling-Wave Operation

The stem-loaded waveguide is a four port device with two ports at the in- and output, respectively. An input matching network shall provide maximum power transfer from the RF source to the accelerating structure. For a one-port network it is well known that maximum power transfer is obtained through complex conjugate matching, see e.g. [49]. If maximum power transfer can also be ensured between the waveguide and terminating load, a pure travelling wave with maximum accelerating voltage and broadband impedance characteristic is obtained in the structure.

The output of the unmatched stem-loaded waveguide acts back on its input which is why the addition of an output matching network would change the input reflection coefficient of the structure and vice versa. The in- and output matching must therefore be designed simultaneously to ensure complex conjugate match at both ports. To facilitate the matching network design, the problem is reduced to two ports by the reasonable assumption of a left-right symmetry of the structure. In EM simulations this can be implemented by a magnetic boundary in the vertical-longitudinal plane and in practice by using a 3 dB, 0°-splitter/ combiner at both in- and output. If necessary, the so designed two-port matching networks could be deployed on both ports at the in- and output respectively to match the full four-port structure.

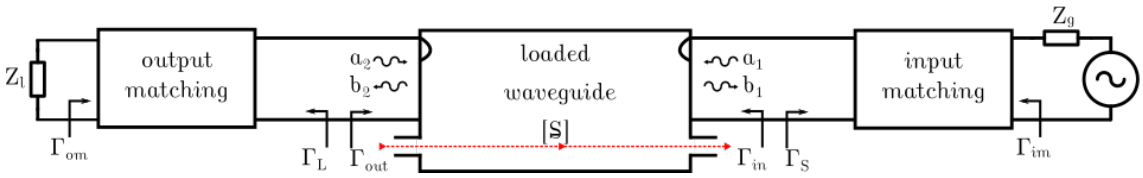

Figure 3.19.: Circuit model of a travelling-wave system consisting of an RF source with internal impedance Z_g, in- and output matching networks, the periodically loaded waveguide and the terminating load Z_l.

The overall system can be modelled by the circuit in Fig. 3.19. The stem-loaded waveguide is described by the 2x2 scattering parameter matrix $\underline{\mathbf{S}}$ and the demands on the matching are summarised as

- $\underline{\Gamma}_{im} = 0 \quad (\underline{\Gamma}_{om} = 0)$
- $\underline{\Gamma}_{in} = \underline{\Gamma}_S^* \quad \& \quad \underline{\Gamma}_{out} = \underline{\Gamma}_L^*$

- Broadband match to damp neighbouring modes with high beam coupling impedance in the FPB.

The broadband match is already inherent in the design of the FPC coupling loops that can ensure travelling-wave operation over a bandwidth of roughly 4 MHz without additional matching sections, see Fig. 3.22 later on.

In the past, an iterative matching procedure was used which consists of adjusting coaxial matching sections at the in- and outputs until $\underline{\Gamma}_{im}$ and $\underline{\Gamma}_{om}$ are suppressed to a satisfying degree around the synchronous frequency of 200.222 MHz. Good power transfer from the generator to the terminating load is then ensured by measuring the received power at the load and comparing to the available power of the generator.

For the purpose of this thesis, a simultaneous complex conjugate matching (SCM) approach, which is well known from microwave transistor amplifier design [49, 50], was adopted to the travelling-wave matching problem at hand. This has to the advantage, that from a single measurement of the scattering parameter matrix $\underline{\mathbf{S}}$, the required impedance of the matching networks can be calculated immediately and the design takes place in a single step. To the authors knowledge the SCM technique was so far not used for matching TWSs.

The specific reflection coefficients Γ_S and Γ_L of the in- and output matching networks that fulfil the conditions for SCM are derived in the following with respect to the nomenclature in Fig. 3.19. We first express Γ_{in} in terms of Γ_L and Γ_{out} in terms of Γ_S by an analysis of the reflected and transmitted wave amplitudes on the two-port loaded waveguide

$$\begin{aligned} \underline{b}_1 &= \underline{S}_{11}\underline{a}_1 + \underline{S}_{12}\underline{a}_2 = \underline{S}_{11}\underline{a}_1 + \underline{S}_{12}\underline{\Gamma}_L\underline{b}_2\,, \\ \underline{b}_2 &= \underline{S}_{21}\underline{a}_1 + \underline{S}_{22}\underline{a}_2 = \underline{S}_{21}\underline{a}_1 + \underline{S}_{22}\underline{\Gamma}_L\underline{b}_2\,. \end{aligned} \tag{3.15}$$

The reflection coefficient seen into the input port then is

$$\underline{\Gamma}_{in} = \frac{\underline{b}_1}{\underline{a}_1} = \underline{S}_{11} + \frac{\underline{S}_{12}\underline{S}_{21}\underline{\Gamma}_L}{1 - \underline{S}_{22}\underline{\Gamma}_L} \tag{3.16}$$

and similarly at its output

$$\underline{\Gamma}_{out} = \frac{\underline{b}_2}{\underline{a}_2} = \underline{S}_{22} + \frac{\underline{S}_{12}\underline{S}_{21}\underline{\Gamma}_S}{1 - \underline{S}_{11}\underline{\Gamma}_S}. \tag{3.17}$$

This system of equations is now solved under the conditions of complex conjugate matching for maximum power transfer. The system then reads

$$\begin{aligned} \underline{\Gamma}_S^* &= \underline{S}_{11} + \frac{\underline{S}_{12}\underline{S}_{21}\underline{\Gamma}_L}{1 - \underline{S}_{22}\underline{\Gamma}_L} \\ \underline{\Gamma}_L^* &= \underline{S}_{22} + \frac{\underline{S}_{12}\underline{S}_{21}\underline{\Gamma}_S}{1 - \underline{S}_{11}\underline{\Gamma}_S} \end{aligned} \tag{3.18}$$

and the solution is obtained to

$$\begin{aligned} \underline{\Gamma}_S &= \frac{B_1 \pm \sqrt{B_1^2 - 4|C_1|^2}}{2C_1} \\ \underline{\Gamma}_L &= \frac{B_2 \pm \sqrt{B_2^2 - 4|C_2|^2}}{2C_2}, \end{aligned} \tag{3.19}$$

with

$$\begin{aligned} B_1 &= 1 + |\underline{S}_{11}|^2 - |\underline{S}_{22}|^2 - |\Delta|^2, \\ B_2 &= 1 + |\underline{S}_{22}|^2 - |\underline{S}_{11}|^2 - |\Delta|^2, \\ C_1 &= \underline{S}_{11} - \Delta\underline{S}_{22}^*, \\ C_2 &= \underline{S}_{22} - \Delta\underline{S}_{11}^*, \\ \Delta &= \underline{S}_{11}\underline{S}_{22} - \underline{S}_{12}\underline{S}_{21}. \end{aligned} \tag{3.20}$$

The positive sign in front of the radical in Eq. (3.19) is to be used if $B_{1/2} > 0$.

With Eq. (3.19), in- and output matching networks can be designed by a single measurement of the two-port TWS, taking also their respective terminations Z_g or Z_l immediately into account. In the general case, reflections and standing waves occur on the matching networks in front and behind the TWS, meaning that the power in the multiple reflections adds up constructively to deliver or take out maximum power to or from the accelerating structure. However, as the maximum possible power is delivered from the input matching network to the TWS and the same amount of power is taken out (in the lossless case), no standing waves may occur on the TWS itself. Within the accuracy and bandwidth of the matching, a pure travelling wave is therefore ensured in the accelerating structure.

3.7. Preface to EM Simulations with CST and ACE3P

The development of a new, improved HOM damping scheme for the future 33-cell TWSs had to rely heavily on numerical EM simulations. This cell configuration has never been used in the SPS before and a 33-cell test setup became available for RF measurements only very recently. Typically, frequency domain eigenmode and time domain wakefield solvers are used for calculating the beam coupling impedance of particle accelerator devices. The wakefield solver calculates the wake potential (refer to Section 2.1) of the structure under test from which the impedance over a large frequency range can be computed. This is especially appropriate and important for long accelerator structures in which the impedance of neighbouring, low Q resonances overlap. The computationally less demanding eigenmode simulation calculates the impedance via the energy stored in the volume of the structure. The quality factors as 'seen' by the beam do not correspond to the quality factors calculated by the eigenmode solver which only depend on the RF losses. A beam loading is not taken into account.

Due to the importance of the HOM damping upgrade, two simulation suites were used to benchmark the results obtained from wakefield simulations. These are the Microwave & Particle Studio suite of Computer Simulation Technology company (CST) [42] and the Advanced Computational Electromagnetic 3D Parallel Simulation Suite (ACE3P) [31]. The eigenmode solvers of these two suites deliver quasi identical results for the structures calculated throughout this thesis. This is not surprising as the eigenmode solver of both codes is based on the finite-element method (FEM) [51] and uses tetrahedral meshing for discretisation of the computational domain. Therefore, only the eigenmode results of CST will be shown throughout this thesis, but important results were also verified by the eigenmode solver of ACE3P. The two suites differ however conceptually in the implementation of their respective wakefield solvers. The CST wakefield solver is closely related to the finite-difference time-domain (FDTD) method [52] and uses hexahedral meshing. The wakefield solver of ACE3P however is based on FEM and uses curved tetrahedral elements which are more powerful in meshing small geometric features. ACE3P was specifically developed for modelling large accelerator structures with small and complex geometric features and is optimised for large-scale parallel computing on the supercomputing facilities at the National Energy Research Scientific Computing Center (NERSC) [53] in the USA. The wakefield results of the two simulation suites agree to a reasonable extent, however, as significant differences can be observed, the results of both will be shown and compared for the important cases. The achieved additional HOM damping factor is confirmed by both codes, which gives great confidence in the results. The time domain wakefield solver of ACE3P is called Tau3P (T3P).

3.7.1. Wakefield Simulation of Longitudinal Beam Coupling Impedance

Some details of the wakefield calculation method and some of the simulation settings are outlined in the following. The structure under study is excited by stepping a rigid, longitudinal line charge of typically Gaussian distribution along its beam axis. The wake potential is then calculated according to Eq. (2.3) as function of the distance s behind the centre of this exciting line charge representing the leading particle bunch. The beam coupling impedance calculated by Eq. (2.6) is made independent of the bunch length by normalisation to the Gaussian frequency content and the total charge in the distribution. The choice of the standard deviation σ_z of the Gaussian line charge depends on the maximum frequency of interest f_{max} in the impedance spectrum and is a decisive simulation parameter for the following reasons. The Gaussian frequency spectrum approaches zero after some σ_f, amplifying noise and introducing numerical errors in the impedance spectrum. Higher frequencies in the structure are less strongly excited compared to lower frequencies. For a shorter bunch however, the mesh density must be increased to avoid that a too large portion of the bunch is stepped over mesh cells instead of gradually exciting consecutive cells on the beam path. Similarly, the time step of the simulation must also be reduced. Both, the increased mesh size (higher total number of mesh cells) and the reduced time step, increase the simulation time. The bunch length must therefore be chosen appropriately and the impedance calculation is stopped above $f_{max} = n\sigma_f$. The spatial and spectral widths of the Gaussian bunch are inversely related

and the required bunch length σ_z for a maximum frequency f_{max} in the impedance spectrum is calculated from

$$\sigma_z = n\frac{c}{2\pi f_{max}}. \tag{3.21}$$

Typically $n = 3$ is chosen for which the bunch spectrum drops to 1 % of its peak value. At present, the HOM impedance of the SPS TWSs is only of interest up to a frequency of 1 GHz. It is expected that no significant impedance relevant for today's beam stability lies beyond this frequency in the structure. The longest allowed bunch length sufficiently exciting this frequency is determined to 143 mm.

After choosing the appropriate bunch length, mesh and time step convergence studies have to be conducted with the goal to obtain the least computationally demanding simulation delivering reliable impedance results. Guidelines for an appropriate mesh size are no less than ten mesh lines per minimum wavelength of interest in CST and an average mesh edge length l satisfying $l \leq \sigma_z/3$ in T3P. In the first place, the mesh must however be dense enough to resolve areas with small geometric features. The mesh convergence study then consists of decreasing the maximum allowed element size and calculating the wake potential for the length of the structure, meaning until the bunch has left the structure. Convergence is achieved when the results are stable and the procedure is repeated with a decreasing time step. Sampling the frequency component with the shortest wavelength of interest in the wake potential by ten points is a good starting point. In the final simulation with stable parameters the required wake-length depends on the quality factor of the resonances within the structure. The resolution in the impedance spectrum can only be increased by a longer simulation time.

Mesh convergence studies were conducted in both T3P and CST to obtain the smallest possible mesh size for the SPS 33-cell TWS that delivers reliable impedance results. A magnetic boundary condition in the vertical symmetry plane can be used for the impedance calculation of the longitudinal HOMs if the coaxial HOM couplers are oriented longitudinally as well. In T3P, a convergence study has to be conducted for the time step as well whereas CST chooses the appropriate time step automatically. In T3P the tank volume can be meshed quite coarse as curved, 10-point tetrahedral elements are used whereas the electric pickups have to be meshed densely. The mesh with straight-edge tetrahedra is visualized in Figs. 3.20a and 3.20b. In CST, hexahedra are used for discretisation of the computation domain, see Fig. 3.20c. The superiority of a tetrahedral over a hexahedral mesh in modelling the fine structures and making a smooth transition to the large tank volume is evident when comparing the meshes shown in Fig. 3.20.

The final simulation settings for the two solvers are given in Table 3.1. A good quality mesh without badly shaped elements is obtained in T3P for a total mesh count of at least 1.2 to 1.4 million tetrahedra, depending on the amount of HOM couplers used in the 33-cell structure. The average mesh edge length then is far below the above given stability guideline for a 143 mm bunch length. It was therefore reduced to 115 mm, allowing to calculate the impedance spectrum beyond 1 GHz without requiring a denser mesh or shorter time step. In CST the required bunch length and maximum allowed time step are influenced by other parameters and the latter is calculated automatically. Sixteen to 21 million hexahedra are required to reach mesh convergence in CST. For a sufficient resolution of the impedance spectrum in the high-impedance 630 MHz frequency

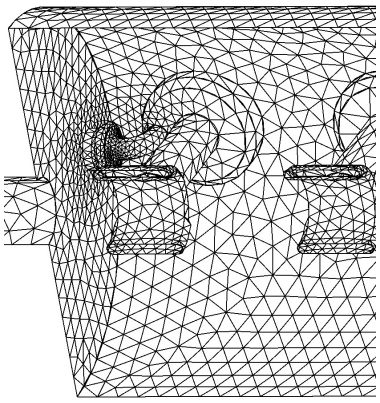

(a) Shorted FPC elbows and coarse meshing of tank volume in T3P.

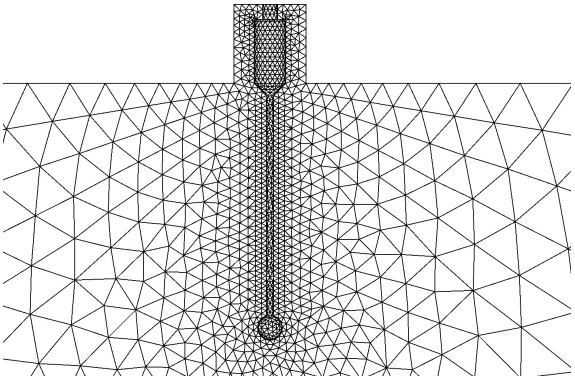

(b) Meshing of electric pickup in T3P.

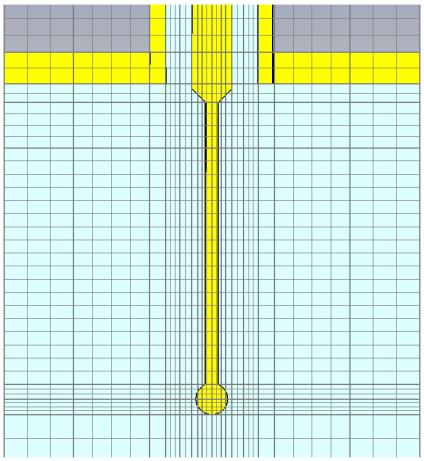

(c) Meshing of electric pickup in CST.

Figure 3.20.: Discretisation of the computation domain with tetrahedra for T3P and hexahedra in CST. In T3P curved tetrahedra are used, but only straight-edge tetrahedra can be visualised here.

Table 3.1.: Simulation settings in T3P and CST for calculation of beam impedance in 33-cell structures with different HOM coupler configurations simulated throughout this thesis.

	T3P	**CST**
f_{max} [GHz]	1	1
bunch σ_z [cm]	11.5	10
bunch charge [pC]	1	1
# mesh [Mio.]	1.2 - 1.4 tets	16 - 21 hex
Δt [ps]	20	$\rightsquigarrow \approx$1.3
wake [km]	1.5-3	3
basis order	2nd	-
linear solver	MUMPS	-

range a wake-length of at least 1.5 km is required even in the heavily damped cases. Such long wakefield simulations are computationally expensive and time consuming with simulation times of about 14 days on a shared server. On computer clusters implementing MPI (Message Passing Interface), the simulation time is reduced to three to four days.

For details about the calculation methods used in T3P and the additional simulation parameters given in Table 3.1 refer to [54]. Both EM solvers merely calculate the fields on the mesh nodes. In between nodes the EM fields have to be interpolated and in case of T3P optionally by higher order basis functions. Elements of higher degree are computationally more demanding, but the total element count can be reduced leading to a trade-off between mesh density and interpolation order. Tests with 1st to 3rd order basis functions were conducted on the SPS TWS geometry. No significant differences in the impedance results were observed between 2nd and 3rd order, however the required computational resources drastically increased in case of the 3rd order basis function. First order elements resulted in inaccurate results so that the 2nd order interpolation was used for all simulations conducted throughout this thesis.

3.7.2. Implementation of a Lossy Perfectly Matched Layer for the Simulation of Resistive Loads

The perfectly matched layer (PML) as well as the absorbing boundary condition (ABC) are very common in FDTD and FEM simulations to terminate the calculation domain. In the form of waveguide-ports these techniques are often used to simulate boundaries without reflection of EM waves, as e.g. the open boundary condition. Waveguide-ports can therefore also be used to simulate the terminating, resistive loads of both coaxial- and waveguide-type HOM couplers on full-scale cavity models. However, due to their implementation they cannot be used together with periodic boundaries in unit-cell simulations as the energy loss through them can not properly be taken into account. The periodic boundaries facilitate the study of modes with a specific phase advance per cell, like e.g. the $^{14\pi}/_{33}$ HOM around 630 MHz discussed at the end of Section 3.4.3. Due to the small size of such simulations, the optimisation of HOM couplers for specific modes would be

most rapid and convenient if the coupler model could be included in the unit-cell simulation. For this purpose, a PML was implemented via a lossy material that mimics the behaviour of a resistive load. The appropriate characteristics such a material must fulfil are detailed further below. The lossy PML then makes part of the simulation model, see Fig. 3.8b, and can therefore also be used in unit-cell simulations with periodic boundaries, contrary to waveguide-ports. Finally, the PML was used not only for the termination of the numerous HOM couplers on full-scale simulation models of the SPS TWSs, but also for the termination of the in- and output matching networks. This modification made the models very convenient to use. The models became consistent across the different solver types within a simulation suite, as no specific parameters need to be set (as it is the case for waveguide-ports), but also across the two simulation suits CST and ACE3P used throughout this thesis.

A lossy material is characterized by its complex permittivity $\underline{\varepsilon}$ and permeability $\underline{\mu}$

$$\underline{\varepsilon} = \varepsilon - j\frac{\sigma}{\omega} \tag{3.22}$$

$$\underline{\mu} = \mu - j\frac{\sigma_m}{\omega} \tag{3.23}$$

with σ being the electric and σ_m the magnetic conductivity. At the interface between a lossless material and the matched load an incident EM wave shall ideally undergo full transmission and zero reflection. From these boundary conditions the relations

$$\frac{\mu_2}{\varepsilon_2} = \frac{\mu_1}{\varepsilon_1} \quad \text{and} \quad \frac{\sigma_m}{\mu_2} = \frac{\sigma}{\epsilon_2} \tag{3.24}$$

between the media are derived which ensure the proper matching [55]. For a transition from free space, we have $\varepsilon_r = \mu_r = 1$ which results in the condition

$$\sigma_m = \sigma\frac{\mu_0}{\varepsilon_0} \tag{3.25}$$

that the material properties of the load have to fulfil. Here, ε_0 and μ_0 are the permittivity and permeability respectively in free space and ε_r and μ_r the relative permittivity and permeability respectively of the two materials. For a very poor conductor with the arbitrary value of $\sigma = 0.5\ ^S/_\mathrm{m}$ a coaxial load with a length of 20 mm is sufficient to fully absorb an incident wave. The simulated reflection coefficient of the lossy PML is below -60 dB and independent of frequency[4] as well as the characteristic impedance of this coaxial load. The actual 50 Ω load resistors in use on the HOM couplers have a maximum power rating of 25 W and perform typically around -45 dB reflection in the 630 MHz frequency range.

[4] verified from DC up to 1 GHz.

3.8. Simulation of the 33-Cell Structure

3.8.1. Matching of the FPB and Calculation of Its Peak Forward Impedance

To properly simulate the forward impedance of a 33-cell structure, it must be matched around the $\pi/2$-mode so that a pure travelling wave is obtained. The one-step matching procedure described in Section 3.6.2 for a simultaneous match of the in- and output of the structure is applied to this case in the following. Due to the exact structural symmetry in simulations, the procedure will result in identical matching networks at the in- and output. The scattering parameters of the parallel stem structure are simulated in arbitrarily chosen planes on the coaxial lines shown in Fig. 3.21a. This case of an arbitrary match, in which the coaxial lines of random length are merely terminated

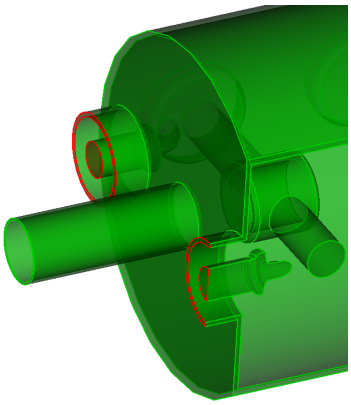

(a) Arbitrary match used for the illustration of an ill-matched TWS. Planes for implementation of the SCM (see (b)) are highlighted in red.

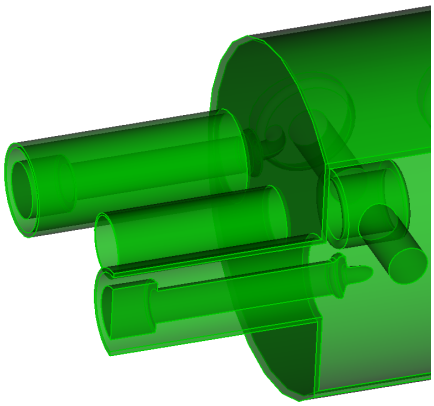

(b) Matching network implementing the SCM and used for impedance simulations of the travelling-wave FPB.

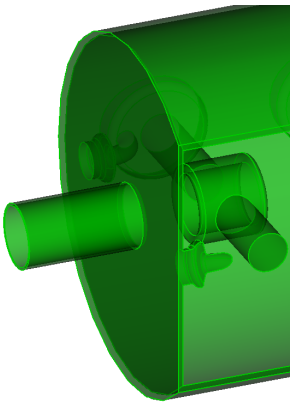

(c) Worst case scenario used for the simulation of 630 MHz-HOMs. The coupling loops of the FPCs are shorted in the plane of the end-plate resulting in full reflection of these HOMs.

Figure 3.21.: Different terminations of the FPCs in simulations used throughout this thesis.

by their 50 Ω characteristic impedance, is in the following also used to illustrate the impact of a mismatch on the accelerating voltage.

The scattering parameters at the synchronous frequency of 200.222 MHz are simulated to

$$\begin{aligned} \underline{S}_{11} &= \underline{S}_{22} = 0.6227\angle -34.6° \\ \underline{S}_{12} &= \underline{S}_{21} = 0.7697\angle -124.6° \,. \end{aligned} \tag{3.26}$$

Following Eq. (3.19), the structure is properly terminated for travelling-wave conditions at this frequency by matching networks that present the reflection coefficient or the equivalent input impedance of

$$\begin{aligned} \underline{\Gamma}_m &= 0.355\angle 38.5^\circ \quad (= \underline{\Gamma}_S = \underline{\Gamma}_L) \\ \underline{Z}_m &= (76.6 + j38.7)\,\Omega \end{aligned} \tag{3.27}$$

to the 33-cell structure. Obviously, this is not simply the complex conjugate of the reflection coefficients S_{11} and S_{22}. For simulations, the simplest realisation of this matching is a step transition to a coaxial line with characteristic impedance of 23.8 Ω (corresponding to $\Gamma = 0.355\angle 180°$) and an elongation of the existing 50 Ω line by 0.294 m which adds the required phase shift of 141.5° at 200.222 MHz. The characteristic impedance Z_0 of a coaxial line with outer and inner diameters D and d respectively is defined as

$$Z_0 = \sqrt{\frac{\mu}{\varepsilon}}\,\frac{\ln(D/d)}{2\pi}\,. \tag{3.28}$$

The matching network is shown in Fig. 3.21b. For other than scattering parameter simulations, the 23.8 Ω-line is terminated by the lossy PML introduced in Section 3.7.2.

Simulated input reflection and transmission coefficients for the 33-cell TWS with arbitrary match and SCM are compared in Fig. 3.22. The input reflections at the synchronous frequency of 200.222 MHz are S_{11}= -4.1 dB and S_{11}= -30.1 dB respectively. In simulation, $S_{11} = S_{22}$ and $S_{21} = S_{12}$ due to the perfect symmetry. From a single measurement of scattering parameters (Eq. (3.26)), the SCM technique immediately provides an excellent match (Eq. (3.27)) without requiring any further adjustments. Figure 3.22a shows a narrowband match around 200.222 MHz resulting in negligible reflections towards the RF source, but also the broadband characteristic required to damp adjacent, high-impedance modes excited by the beam. Figure 3.22b illustrates the bandpass like behaviour of the structure. In the well matched case and for an RF injected around 200 MHz, the 33-cell structure basically behaves as a waveguide with the transmission S_{21}=-0.12 dB being quasi entirely a result of its resistive losses. The typical characteristics of resonant modes are no longer visible in this frequency range as they are damped by the FPCs with the attached SCM networks.

The simulations of the electric field on the central axis of the 33-cell structure at 200.222 MHz for the two matchings are shown in Fig. 3.23. Note that the peak fields of these two cases have to be compared with care due to the different quality of the input match resulting in significantly less power being accepted by the structure in the unmatched case. The modulus of the electric field in Fig. 3.23a clearly shows the π-pattern due to the mismatch of the terminating load to the TWS as predicted by the analysis in Section 3.6.1. Figure 3.23b illustrates that the electric field in the end half-cells is, due to the presence of the FPCs, out of phase with the $\pi/2$-mode along the rest of the structure. Also, the electric field in these cells is strong only over a very short distance so that the two end half-cells do not contribute to the accelerating voltage and the effective length of the structure is only $(N-1)l_c$. By integration of the on-axis electric field at 200.222 MHz the accelerating voltage is calculated to 597 V in case of the arbitrary match and to 1.993 kV for the SCM. The latter is only 0.14 % below the theoretical value for an input power of 1 W_p and using the simulated series impedance of 27.8 $k\Omega/m^2$.

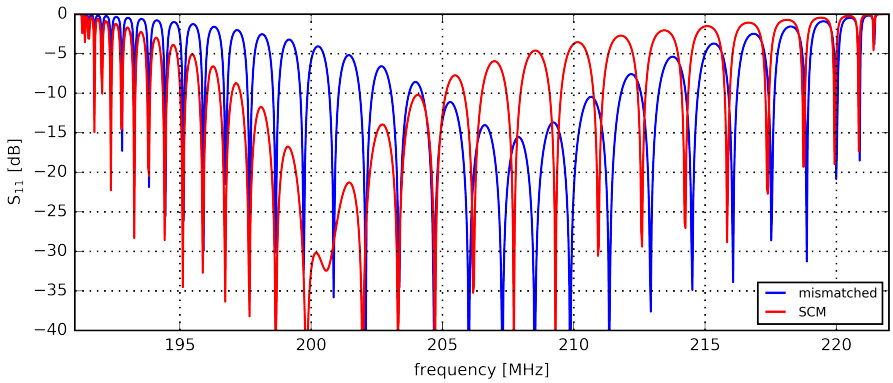

(a) Reflection S_{11}.

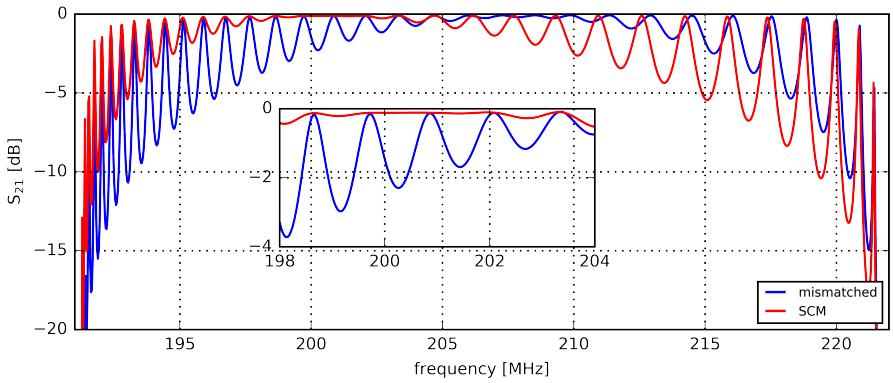

(b) Transmission S_{21}.

Figure 3.22.: Comparison of scattering parameters for the simulated 33-cell structure with arbitrary match (Fig. 3.21a) and SCM (Fig. 3.21b). The SCM results in a broad- ($\approx \pm 5$ MHz) and narrow-band ($\approx \pm 200$ kHz) match around the synchronous frequency of 200.222 MHz. Due to the exact symmetry in simulations there is $S_{11} = S_{22}$ and $S_{21} = S_{12}$.

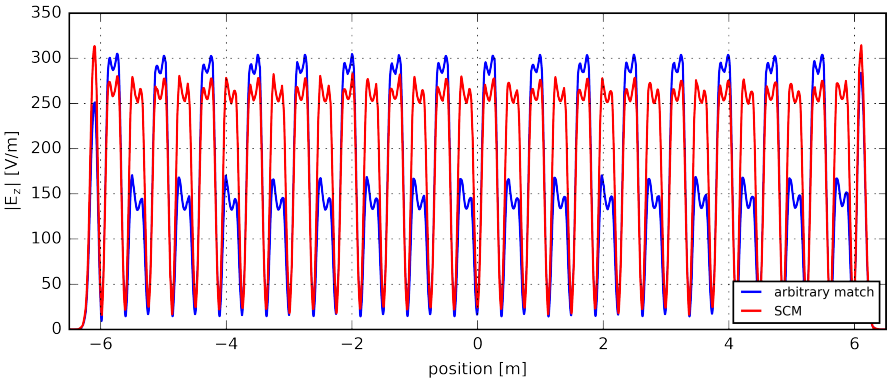

(a) Modulus of electric field E_z.

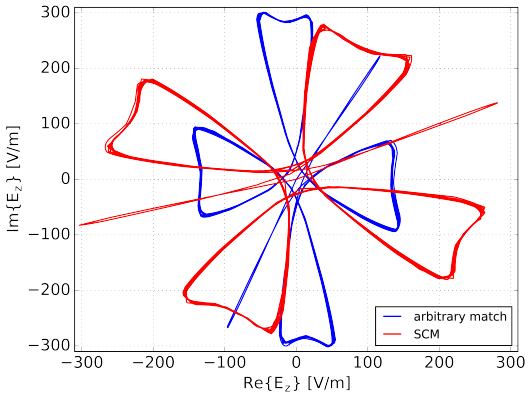

(b) Complex electric field E_z.

Figure 3.23.: Simulation of on-axis, longitudinal electric field E_z at 200.222 MHz in the 33-cell structure with arbitrary match (Fig. 3.21a, S_{11}= -4.1 dB) and SCM (Fig. 3.21b, S_{11}= -30.1 dB) for an input power of 1 W peak injected at z=+6.6 m.

3.8.2. Beam Coupling Impedance of the TS_{11} FPB

The beam coupling impedance for a 33-cell structure obtained from wakefield simulations is compared in Fig. 3.24 to the analytic model of Eq. (2.30). In case of the properly matched structure

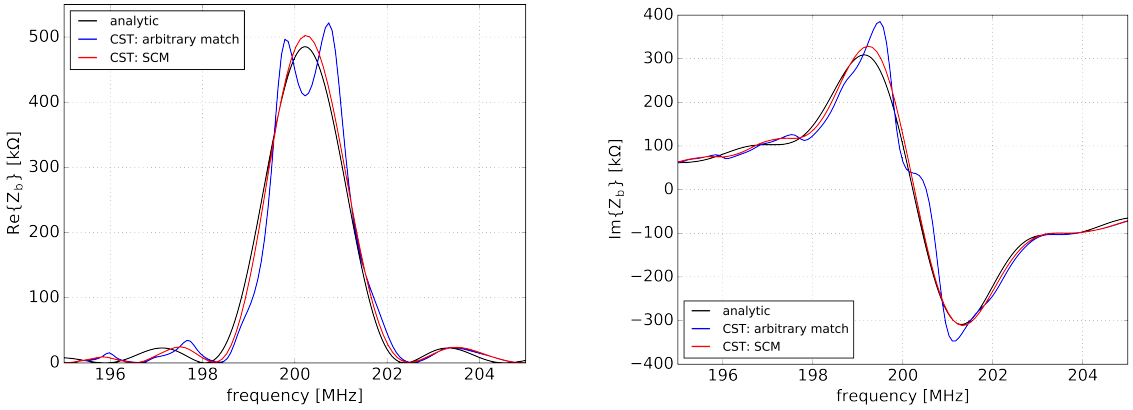

(a) Real part.

(b) Imaginary part.

Figure 3.24.: Beam coupling impedance of simulated 33-cell structure. Comparison of analytic model of Eq. (2.30) with R_2=27.1 $k\Omega/m^2$ to simulations with arbitrary match (Fig. 3.21a) and SCM (Fig. 3.21b).

the agreement to the analytic model is excellent. Note that the slight difference in peak amplitude can be attributed to the higher simulated series impedance R_2. As already discussed previously in Section 3.4, the values reported in [27] are used for the analytic model. The case of arbitrary match illustrates the impact of a mismatched TWS on the beam coupling impedance. Standing wave resonances with large beam coupling impedance occur in the band due to a lack of broadband match around 200.222 MHz. These resonances are not sufficiently damped by the FPCs and can drive the beam unstable.

3.8.3. Beam Coupling Impedance of HOMs and Performance Analysis of the TS_{31} HOM Damping Scheme Used Until Long Shutdown 2

The HOMs up to a frequency of at least 739 MHz can be considered as standing wave resonances. Refer also to Section 3.3.1 in this regard. Simulations of scattering parameters around 630 MHz for the case shown in Fig. 3.21a suggest that the FPCs used until LS 2 do not couple to the cavity in this frequency range. As the FPCs are presently undergoing a redesign, their final coupling to the HOMs is still unknown, but is expected to be weak as well. The final implementation of the matching networks for the fundamental accelerating mode might also impact HOM damping. Therefore, the worst case scenario, in which the HOMs are not at all damped by the FPCs, is assumed throughout this thesis for the impedance calculations of the HOMs. This situation is implemented by shorting the coupling loops in the planes of the end-plates as shown in Fig. 3.21c.

This results in a full reflection of HOM power picked up by the coupling loops and largest quality factors of the TS_{31}-HOMs. Note that any other matching would be random and does most likely not correspond to any real world situation used in the machine after LS 2. It would therefore be unmotivated. The coupling loops themselves however are included in simulations as a volume perturbation that significantly alters the HOM field profiles and hence impacts their impedance.

Figure 3.25a shows the beam coupling impedance of HOMs up to 1 GHz in a 33-cell structure obtained from wakefield simulations with CST on a linear and logarithmic scale. The results shown

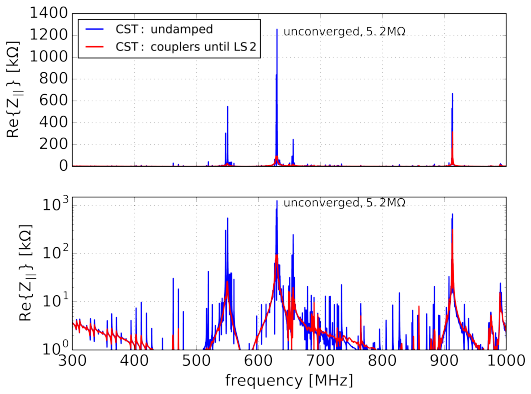

(a) Real part of beam coupling impedance for HOMs up to 1 GHz on a linear (top) and logarithmic (bottom) scale without and with the longitudinal damping scheme used until LS 2. The impedance at 630 MHz is unconverged and Eigenmode simulations suggest a peak of 5.2 MΩ.

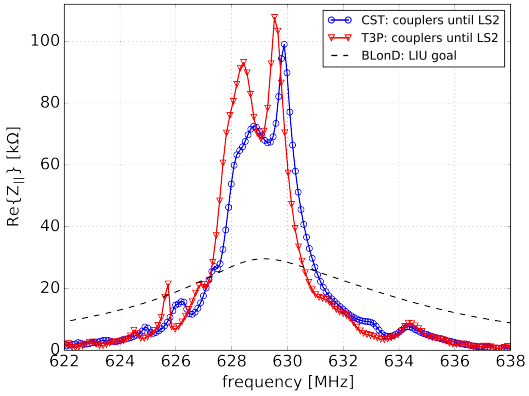

(b) Real part of beam coupling impedance for TS_{31}-HOMs in the 630 MHz frequency range including the longitudinal damping scheme used until LS 2 and calculated by T3P and CST respectively. The LIU goal shows the desired impedance obtained from instability simulations with the Beam Longitudinal Dynamics code (BLonD).

Figure 3.25.: Simulated beam coupling impedance of HOMs in a 33-cell structure based on the worst case matching-scenario for the FPCs shown in Fig. 3.21c.

are for the two configurations illustrated in Fig. 3.26. The undamped case consists of a bare, 33-cell

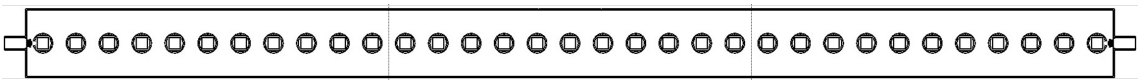

(a) Bare, undamped 33-cell structure.

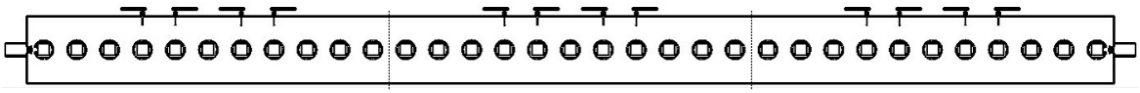

(b) 33-cell structure including the TS_{31}-HOM longitudinal damping scheme consisting of four HOM couplers per 11-cell section and used until LS 2.

Figure 3.26.: Illustration of 33-cell simulation models used for the calculation of HOM beam coupling impedances shown in Fig. 3.25.

structure with short-circuited FPCs but without any HOM couplers. The second case includes the longitudinal damping scheme for the TS_{31}-HOMs used until LS 2, see Fig. 3.26b. Note that the impedance around 630 MHz is unconverged in case of the undamped structure in this time domain wakefield simulation. The quality factors of these HOMs are so high ($Q \approx 40000$) that despite a simulated wake length of 3 km the sampling in the impedance spectrum is insufficient to resolve this impedance peak fully. Eigenmode simulations are better suited to calculate the impedance in this case and suggest a peak impedance of 5.2 MΩ at this frequency. The damping introduced by the HOM couplers is very broadband and results in damping by a factor of around 50 of the TS_{31}-HOMs at 630 MHz. Another strong impedance peak is also visible at 915 MHz which corresponds to the 2nd higher order passband of the fundamental TS_{11}-mode at the 5-th harmonic frequency. In comparison to the HOMs at 630 MHz, these modes are excited less by the beam spectrum and have, due to their relatively large quality factors, too long rise times to be responsible for the multi-bunch instability[5]. It is known that a strong longitudinal impedance can also be observed around 1.4 GHz corresponding to the 7-th harmonic, however these modes so far showed to be of less relevance for beam stability.

Figure 3.25b shows a detailed view of the damped TS_{31}-HOMs in the 630 MHz frequency range calculated by the T3P and CST solvers. The agreement between the two solvers is reasonable considering that CST uses hexahedral mesh whereas T3P uses tetrahedral mesh. The impedance peak at 628 MHz seems better resolved by the more adequate tetrahedral mesh. A deviation in frequency by around 500 kHz is also observed between the two solvers. Better agreement might be achievable by a further increase of the mesh density (using smaller mesh elements), but the additional insight that could be gained from an RF perspective is marginal whereas the computational effort increases even further. The multi-bunch instability in the SPS depends mainly on the maximum shunt impedance in the 630 MHz frequency band and not on a shift of a few Megahertz [57]. The calculated longitudinal impedance of around 100 kΩ for the 33-cell structures is too high for the HL-LHC beam intensity. The LIU requirement for the additional mitigation of these HOMs is also shown in Fig. 3.25b. Ideally, the impedance in the 630 MHz range of a 33-cell structure with the improved HOM damping scheme should lie below this LIU goal. The desired impedance results in the intensity threshold shown in green in Fig. 1.18.

[5]Recent simulation results of the full LHC proton beam in the SPS with BLonD suggest that these HOMs are triggering multi-batch instabilities for the beam intensity required in the future [56].

4. Improvement of TS_{31} HOM Mitigation in the Future 33-Cell Structures

4.1. Analysis of TS_{31} HOMs in 11- and 33-Cells

The longitudinal damping scheme in use until LS 2 consists of four 630 MHz couplers per 11-cell section as was already introduced in Fig. 3.26b. Little documentation exists, but the regular placement of the HOM couplers suggests that the damping scheme was developed on a single section instead of on the full 44 or 55 cell structures. As a consequence, HOMs which are only affiliated to the long structures built of several sections are not specifically targeted by this damping scheme. Results from the eigenmode solver for the 11-cell standing wave resonances in the 630 MHz frequency range for both the undamped and damped cases are shown in Fig. 4.1. The important modes are identified from their transverse electric field profiles and labelled accordingly by their phase advance per cell in the travelling-wave case. The $^{8\pi}/_{11}$-mode at 626.6 MHz is of the upper TS_{31}-passband as was developed in Section 3.4.3 and shown in Fig. 3.16. In the bare section, the resonance with the largest impedance is the $^{5\pi}/_{11}$-mode at 628.7 MHz. This mode has by far the largest $^{R}/_{Q}$ of all resonances, which is a result of its close synchronism with the particle beam, cf. Fig. 3.16. Its electric field in the vertical plane is shown in Fig. 4.3a. To identify this essentially transverse mode, we need to count the number of half period oscillations in the transverse electric field along the length of the structure. In Fig. 4.3a, five half period oscillations over 11 cells are identified. Note also the longitudinal electric field on axis of the $^{5\pi}/_{11}$-mode shown in Fig. 4.3b. Its phase shows the typical characteristic of a standing wave mode on a shorted piece of transmission line. Using Eq. (3.5) to create Fig. 4.4 and comparing to Fig. 4.3a, we see that we can actually predict the relative transverse electric field strength in the stem cells at the positions of the HOM access ports - a prerequisite for the potential placement of HOM couplers. Prediction is still possible when numerous cells are equipped with HOM couplers.

We now analyse the performance of the pre-LS 2 HOM damping scheme on the single section by using the quasi identical eigenmode results obtained from CST and ACE3P presented in Fig. 4.1. The data shows that the impedance of the $^{5\pi}/_{11}$-mode is damped by almost two orders of magnitude. The loaded quality factor Q_l is simulated to 490 for this mode.

The HOM with the largest impedance in the damped configuration is the $^{8\pi}/_{11}$-mode. However, its Q_l is still quite high so that its impedance is negligible in the deteriorating frequency range of 628 to 630 MHz due to its narrowband characteristic. The impedance of the other HOMs in the

frequency range is damped as well and the mode damping is in most cases accompanied with a shift of the resonance frequencies to lower values.

The performance of the pre-LS 2 damping scheme on 33-cells is presented in Fig. 4.2 The FPCs should now also be included in the model to obtain meaningful results (refer to Section 4.2). As discussed, the worst case scenario shown in Fig. 3.21c is assumed. The most important HOMs of interest in the two TS_{31} passbands are again labelled by their phase advance per cell. In this context, we conclude the following:

- The huge geometry factor of the $^{14\pi}/_{33}$-mode in the undamped configuration is due to the exact synchronism of this mode with the beam, cf. Fig. 3.16.
- The placement of the HOM couplers changes the geometry, shifts the resonance frequency and slightly modifies the longitudinal field profile E_z of the $^{14\pi}/_{33}$-mode resulting in a heavily mitigated $^{R}/_{Q}$ in eigenmode simulations. Refer also to Eq. (2.12) in this regard.
- The $^{5\pi}/_{11}$-mode already observed on the single section fits three times in 33-cells and therefore also exists in this cell configuration.
- The $^{8\pi}/_{11}$ mode having high impedance in the single section has lower impedance in the longer 33-cells as it is out of synchronism with the beam in long structures, see Fig. 3.16.
- The very good damping performance of the pre-LS 2 damping scheme can also be explained by the HOM coupler analysis that follows in Section 4.3. In the damped configuration we are basically left with four HOMs of significant impedance in the 630 MHz frequency range.
- The $^{14\pi}/_{33}$- and $^{5\pi}/_{11}$-modes have large $^{R}/_{Q}$ but low Q_l. The $^{22\pi}/_{33}$- and $^{23\pi}/_{33}$-modes of the upper TS_{31}-passband (shown in Fig. 3.16) have moderate $^{R}/_{Q}$ but still a large Q_l. These four HOMs must be targeted to reduce the impedance around 630 MHz.

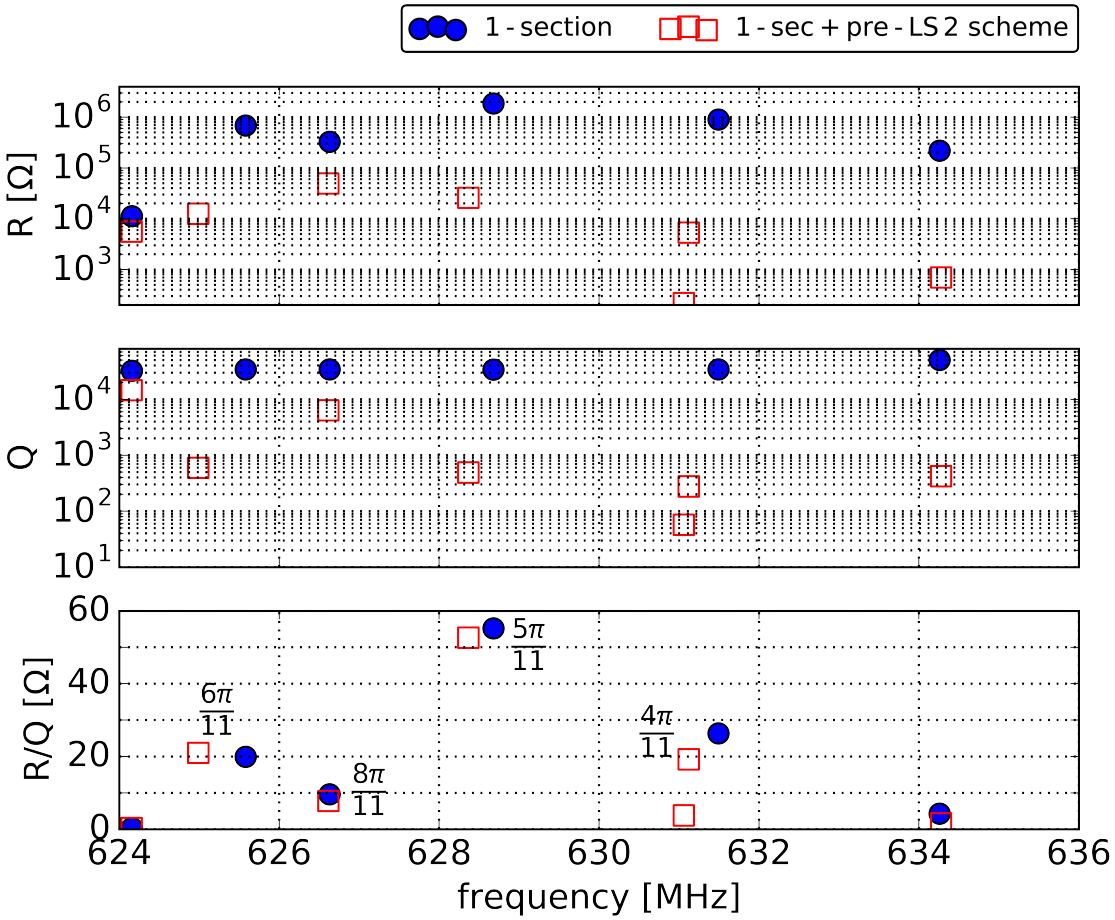

Figure 4.1.: Shunt impedance R, quality factor Q and geometry factor R/Q of eigenmodes in an **11-cell section** terminated by metallic end-plates and in two configurations. One, the bare section without HOM couplers. Two, with four longitudinal HOM couplers installed in the positions shown in Fig. 3.26b. The FPCs are not included in the model. The $8\pi/11$-mode at 626.6 MHz is of the upper TS_{31}-passband that is shown in Fig. 3.16.

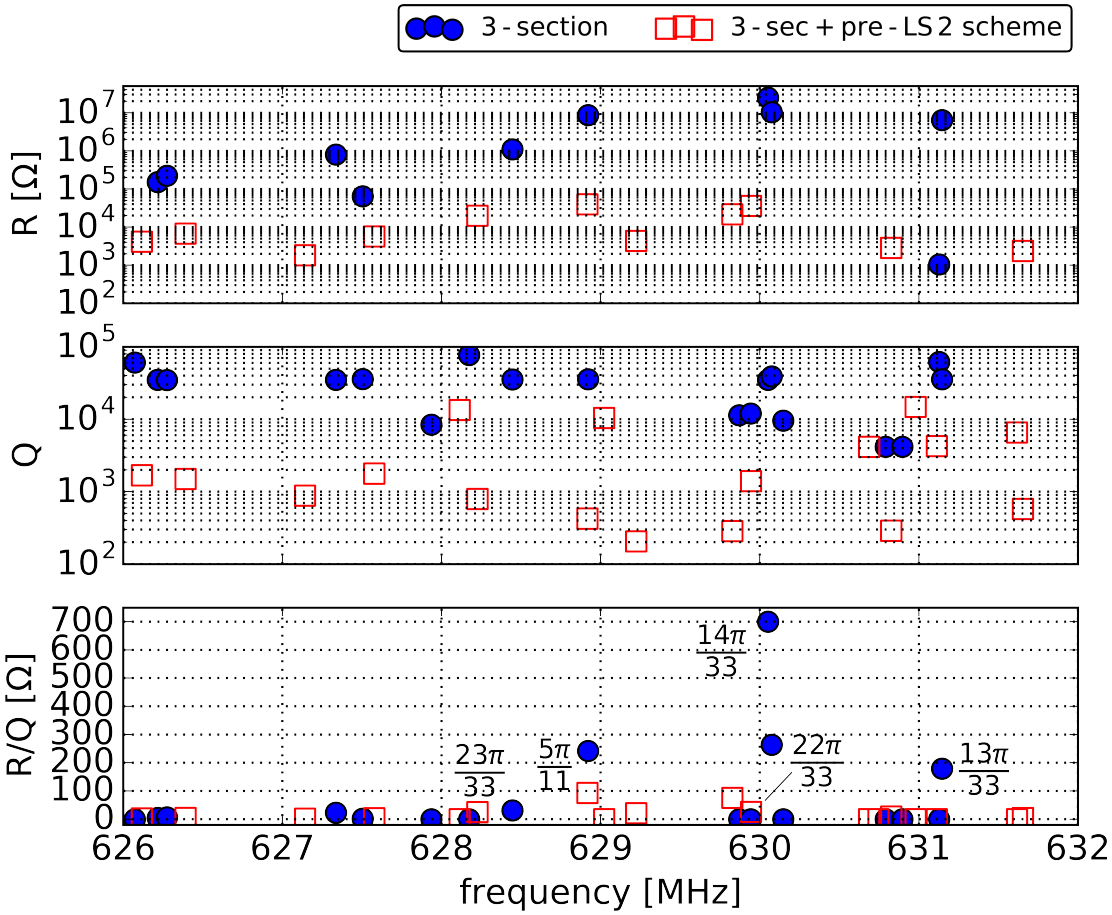

Figure 4.2.: Shunt impedance R, quality factor Q and geometry factor R/Q of eigenmodes in a **33-cell structure** terminated by metallic end-plates and in two configurations. One, the bare cavity without HOM couplers. Two, with 12 longitudinal HOM couplers installed in the positions shown in Fig. 3.26b. The FPCs are included and shorted in the plane of the end-plates as shown in Fig. 3.21c. The $22\pi/33$- and $23\pi/33$-modes are of the upper TS_{31}-passband that is shown in Fig. 3.16.

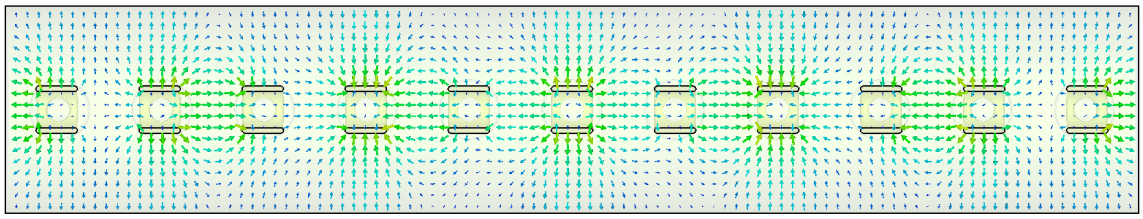

(a) Electric field on the vertical cavity plane. Color-coding of field-strength is on a logarithmic scale. For the field profile in the longitudinal cross-section refer e.g. to Fig. C.3b.

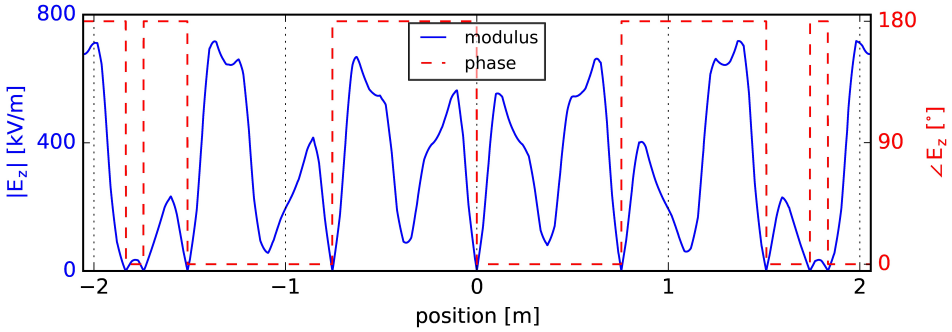

(b) On-axis longitudinal electric field E_z for a stored energy of 1 J.

Figure 4.3.: Electric field of the TS_{31} $^{5\pi}/_{11}$ standing wave mode in a bare, 11-cell section terminated by metallic end-plates. This mode is identified as one of the high-$^{R}/_{Q}$ HOMs building up in the structure which gives a large contribution to the beam coupling impedance.

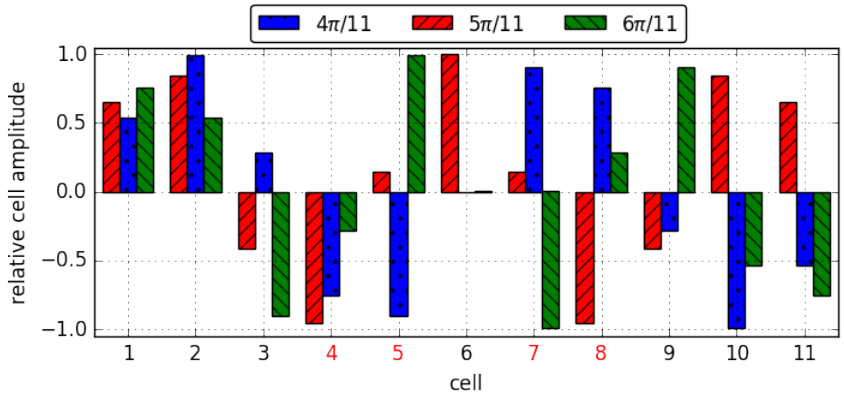

Figure 4.4.: Relative transverse electric field strengths in the stem cells of an 11-cell cavity for different modes obtained from Eq. (3.5). Cells already occupied by HOM couplers in the pre-LS 2 damping scheme are labelled in red on the abscissa.

4.2. Additional HOM Couplers for Increased Damping of TS_{31} Modes

Improved HOM damping can be achieved by adding HOM couplers in cells with strong electric field of the four HOMs identified in the previous section. Suitable cells must also be determined by a one-by-one inspection of the simulated field distributions. The presence of the FPC loops has a shorting-like effect on the electric field in the end half-cells. As a consequence, the EM fields along the whole length of the structure are modified and do not correspond precisely to field distributions in 33 nor 32 cells. The theoretical field distributions in 33-cells as previously presented for the 11-cell section in Fig. 4.4 can therefore only serve as a rough guideline to identify suitable cells for additional HOM couplers **[58]**.

After careful field analysis and only a few full model eigenmode simulations, a damping improvement is achieved by placing six additional couplers in the 33-cells as illustrated in Fig. 4.5 (red). Although the achieved improvement is relatively minor, the impedance of all four high-

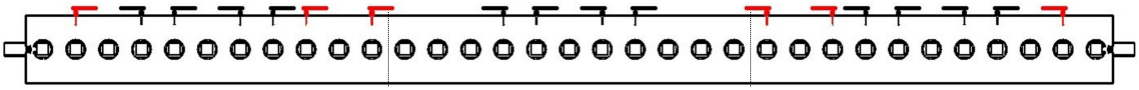

Figure 4.5.: Illustration of 33-cell structure with improved damping scheme for the TS_{31}-HOMs. Six HOM couplers drawn in red are added to the existing, pre-LS 2 damping scheme.

impedance modes is reduced, cf. Fig. 4.6. The eigenmode simulation calculates the loaded quality factors of the $^{14\pi}/_{33}$, $^{5\pi}/_{11}$, $^{22\pi}/_{33}$ and $^{23\pi}/_{33}$ HOMs to 336, 327, 1033 and 460 respectively in the improved damping configuration. The impedance of each mode has a frequency dependence according to Eq. (2.8) and the -3 dB bandwidths of the four HOMs are up to approximately 2 MHz. Due to the mode overlap, the peak impedance in the 630 MHz frequency range is much larger than on first sight suggested by the eigenmode simulations. This is confirmed by the wakefield simulation results of the same damping configurations shown in Fig. 4.7. Eigenmode and wakefield simulations are in good agreement for these configurations. A peak to peak damping improvement by a factor of 1.4 is provided by the six additional HOM couplers. However, the LIU goal to reach a maximum longitudinal peak impedance of around 30 kΩ (also shown in Fig. 4.7) cannot be ensured by this damping configuration.

The loaded quality factor of the $^{22\pi}/_{33}$-mode is significantly larger than that of the two high-$^{R}/_{Q}$ HOMs. Note that the longitudinal HOM coupler is less effective on some of the TS_{31} modes of the upper passband in Fig. 3.16. This is due to a reduced electric field at the position of the electric pickup of these modes, cf. Fig. 4.8a, when compared to the electric field distribution of HOMs in the lower passband, cf. Fig. 4.8b. If required, a specialised HOM coupler to more effectively damp the HOMs of the upper passband could be designed and added to the improved damping scheme later on. Compared to the high-$^{R}/_{Q}$ HOMs of the lower passband, these modes feature strong field in more cells due to their larger phase advance per cell so that finding a suitable spot

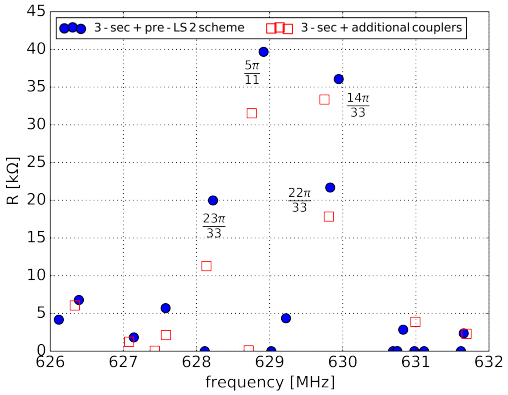

Figure 4.6.: Shunt impedance R in the 630 MHz frequency range of 33-cells with HOM damping configurations illustrated in Fig. 3.26b and Fig. 4.5 respectively. Results obtained from eigenmode simulations.

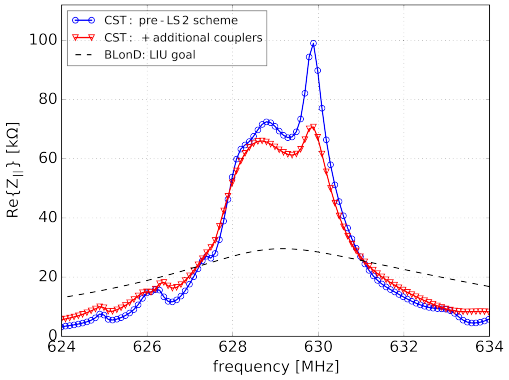

Figure 4.7.: Real part of longitudinal beam coupling impedance $Z_{||}$ in the 630 MHz frequency range of 33-cells with HOM damping configurations illustrated in Fig. 3.26b and Fig. 4.5. Results obtained from wakefield simulations.

for a specialised coupler is easier. In the following the focus is therefore on improved mitigation of the two high-R/Q modes with largest individual impedance.

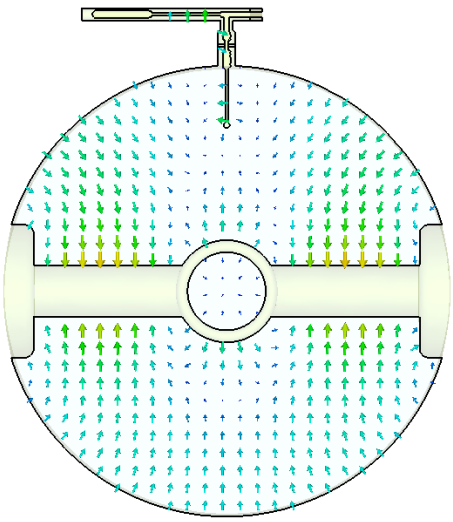

(a) The TS_{31} $^{22\pi}/_{33}$ HOM of the upper passband in Fig. 3.16. The loaded quality factor in this periodic setup is simulated to Q_l=4950.

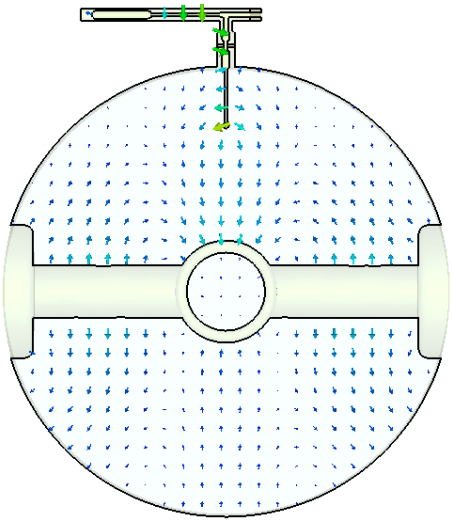

(b) The TS_{31} $^{5\pi}/_{11}$ HOM of the lower passband in Fig. 3.16. The loaded quality factor in this periodic setup is simulated to Q_l=117.

Figure 4.8.: Simulated electric field in a unit-cell with periodic boundaries and equipped with an HOM coupler. Color-coding of field strengths is on logarithmic scales.

4.3. Improved HOM Coupler for Increased Damping of High-$^R/_Q$ TS_{31} Modes

The existing 630 MHz HOM coupler already has an excellent damping performance. If possible however, the coupler shall be further optimised to achieve the additionally required HOM-mitigation. The $^{5\pi}/_{11}$- and $^{14\pi}/_{33}$-modes were identified as the main contributors to the beam coupling impedance in the deteriorating 630 MHz frequency range. The coupler optimisation is therefore targeted foremost to these two high-$^R/_Q$ modes present in a 33-cell structure, possibly allowing less damping of other, less deteriorating HOMs. To gain insight into the coupling mechanism to a cavity mode and the limits of obtainable damping, we consider in the following a standing wave resonance that is to be damped via a single HOM coupler.

The fundamental principle of HOM damping is illustrated in the circuit model of Fig. 4.9. The cavity resonance is again modelled by the parallel RLC resonator. We now want to connect an external load resistor R_l to the cavity so that the resonance not only loses energy by dissipation in the cavity walls but also due to a power flow to the external load resistor. The HOM damping increases with the power P_{ext} transferred to the load. Similar to the unloaded quality factor Q_0 defined via the power loss P_{cav} in the cavity (see Eq. (2.11)) we define an external quality factor

$$Q_{ext} = \frac{\omega_0 U}{P_{ext}}. \tag{4.1}$$

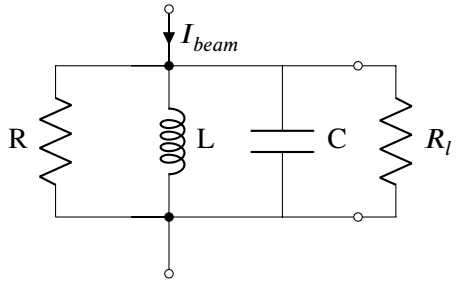

Figure 4.9.: Working principle of HOM couplers.

Q_{ext} is very convenient for quantifying the amount of mode damping that is due to losses external to the cavity. With the total power $P_{tot} = P_{cav} + P_{ext}$ we obtain the relation

$$\frac{1}{Q_l} = \frac{1}{Q_{cav}} + \frac{1}{Q_{ext}} \tag{4.2}$$

for the loaded quality factor Q_l of the damped resonance.

The coupling device used to connect the load resistor to the cavity mode is not modelled in Fig. 4.9. Usually, coupling to the electromagnetic fields of a cavity can be achieved by probe coupling to the electric field, loop coupling to the magnetic field or a mixture of these two mechanisms. Waveguide coupling is an additional option, but not considered here. Instead the focus will be on electric probe coupling with coaxial HOM couplers. Figure 4.10 shows a realistic model for probe coupling to the cavity resonance. The electric pickup is represented by the coupling capacit-

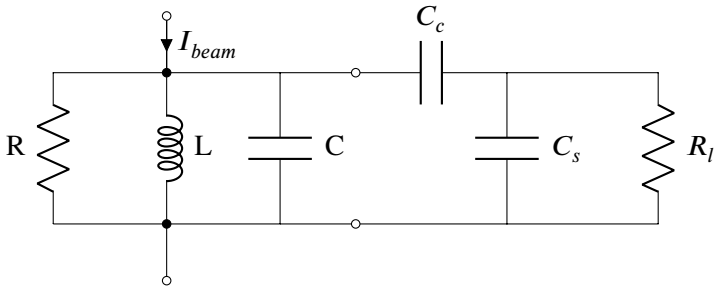

Figure 4.10.: Electric coupling of a resistive load R_l to a cavity resonance.

ance C_c. The small portion of cavity field impinging on the probe tip with surface S induces the current

$$I_0 = j\omega\varepsilon_0 \int_S \vec{E}\, d\vec{S} \tag{4.3}$$

associated to the displacement current of the electric field E. However, the probe also has a parasitic self capacitance in parallel with a stray capacitance due to unavoidable fringe fields. This

fringe field stores energy near the probe, but does not contribute to damping. It must nevertheless be included in the circuit model and is represented by the stray capacitance C_s in parallel with the resistive load [59].

Under the assumption that the cavity is continuously excited to oscillate with constant stored energy U, we can use an equivalent generator approach for some basic studies of the coupler performance that can be expected. Figure 4.11a shows a simplified circuit in which the cavity and the coupling mechanism is replaced by a generator with short circuit current I_0 and internal reactance C_s. The power extracted from the mode is given by

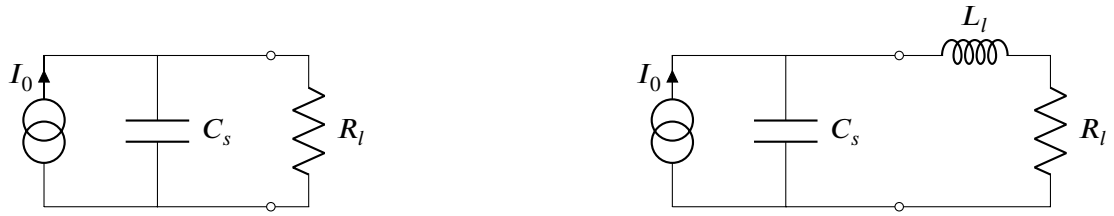

(a) Purely resistive load.

(b) Complex load for series-compensation of C_s.

Figure 4.11.: Equivalent generator circuits for probe coupling.

$$P_{ext} = \frac{1}{2} I_0^2 \,\mathrm{Re}\{Z\} = \frac{1}{2} I_0^2 \frac{G_l}{G_l^2 + (\omega C_s)^2}, \tag{4.4}$$

where the impedance seen by the current source is denoted with Z and $G_l = 1/R_l$. We easily find that the optimum value for the load resistor leading to the lowest Q_{ext} is

$$R_{opt} = \frac{1}{G_{opt}} = \frac{1}{\omega C_s}. \tag{4.5}$$

Apparently, the obtainable damping is always limited by the parasitic probe capacitance. Physically this is explained by the fact that a part of the displacement current picked up by the probe is shunted by C_s and not delivered to the load resistor as would be desired. The dilemma is that when the surface of the probe is increased to improve damping, C_s will increase as well. The gain of an increased current is therefore partially lost, but the maximum size of the pickup is restricted.

This problem can most easily be circumvented at a single frequency by compensating C_s with an inductance in parallel with C_s and R_l. If tuned to the cavity mode, this simple resonant circuit avoids that part of the displacement current is shunted to ground and the load impedance seen by the cavity is purely real. As it is of more use for the application to the 630 MHz HOM coupler later on, we will focus our analysis on a series type compensation of C_s with the inductance placed in series with the load resistor as shown in Fig. 4.11b. By the deployment of this complex load consisting of R_l and L_l in series, the coupler itself is now a resonator with quality factor $Q_c = \omega_0 L_l / R_l$ which

we tune to the cavity resonance so that $\omega_0 = 1/\sqrt{LC} = 1/\sqrt{L_l C_s}$. The real part of the impedance presented to the cavity by the coupler is now

$$\mathrm{Re}\{Z_c\} = \frac{R_l}{\left(\omega C_s R_l\right)^2 + \left(\frac{\omega^2}{\omega_0^2} - 1\right)^2} \tag{4.6}$$

so that the extracted power at resonance is (under constraints)

$$P_{ext}|_{\omega=\omega_0} = \frac{1}{2} I_0^2 Z_c|_{\omega=\omega_0} = \frac{1}{2} I_0^2 \frac{1}{(\omega_0 C_s)^2 R_l}. \tag{4.7}$$

On first sight, there appears to be a contradiction here as the power transfer to the load can apparently be increased to arbitrarily large values by reducing R_l to zero. However, for that specific case there are no external losses and the cavity resonance must be unloaded.

To resolve this issue we must recognize the system of cavity and HOM coupler with complex load as two coupled resonators and apply coupled resonator theory. Due to our compensation of the stray capacitance C_s with the inductance L_l the HOM coupler is now also a resonator. The equivalent generator approach used above showed the limitations due to the stray capacitance C_s. It is however insufficient to describe the effects in coupled resonant circuits with strong coupling. Instead, the full circuit of cavity and HOM coupler with complex load $R_l + j\omega L_l$ shown in Fig. 4.12 must be considered. The two resonators are coupled with a certain coupling factor $0 \leq k \leq 1$ which

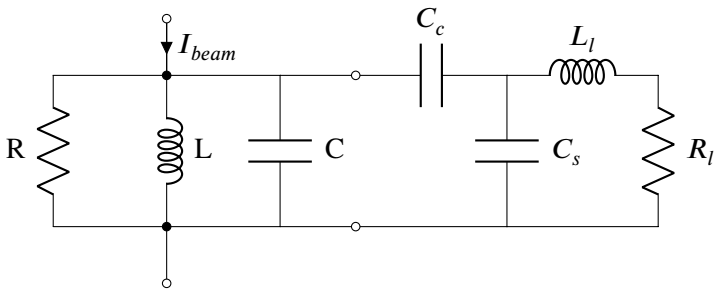

Figure 4.12.: Two capacitively coupled resonators modelling probe-coupling of a complex load $R_l + j\omega L_l$ to an RLC cavity resonance.

describes the coupling strength and the resonator interaction. The typical definition of the coupling factor $k = C_c/\sqrt{CC_s}$ for electrically coupled resonators is given in textbooks, e.g. [60, 61]. After a series-to-parallel conversion of L_l and R_l, the impedance of the circuit seen by the beam current I_{beam} is

$$Z \approx \left(\frac{1}{R} + j\frac{C}{\omega}(\omega^2 - \omega_0^2) + \frac{1}{\frac{1}{\frac{R_l}{\omega^2 L_l^2} + j\frac{C_s}{\omega}(\omega^2 - \omega_0^2)} - \frac{j}{\omega C_c}} \right)^{-1} \tag{4.8}$$

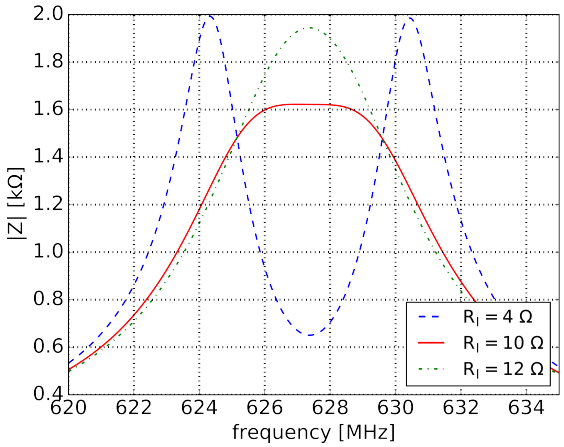

Figure 4.13.: Implementations of the circuit in Fig. 4.12 illustrating under- (R_l=12 Ω), over- (R_l=4 Ω) and critical-coupling (R_l=10 Ω).

and its behaviour can be divided into the three different regimes illustrated in Fig. 4.13. For large Q_c the cavity mode is merely split into two resonances with strong impedance and the largest mode bandwidth is obtained for R_l=0 with $\Delta\omega = k\omega_0$ [62]. This is called the case of overcritical coupling. Optimal damping is usually obtained around the point of critical coupling (R_l=10 Ω in Fig. 4.13) for which we again find an approximate condition $\omega_0 C_c = \sqrt{RR_l}$ in textbooks. In the case of undercritical coupling, Eq. (4.8) shows a single resonance with non-minimal peak impedance.

We now want to relate the external quality factor Q_{ext} of the cavity resonance due to the resonant HOM coupler with the coupling factor k and the lumped values of the complex load. This will allow the optimal design of an HOM-coupler for critical coupling in practice. We adjust the circuit of Fig. 4.12 by using the impedance of the HOM-coupler at resonance from Eq. (4.6) (assuming moderate Q_c at first) such that we arrive at the circuit of Fig. 4.14a. After a series-to-

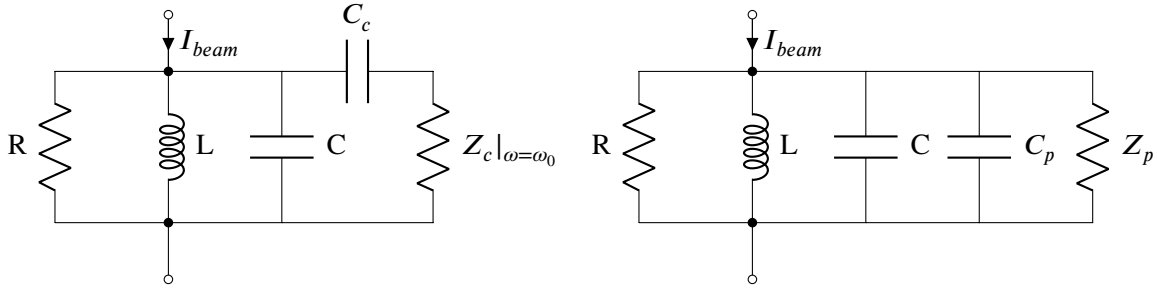

(a) Assumption of moderate Q_c.

(b) Series-to-parallel conversion.

Figure 4.14.: Circuits for the derivation of Eq. (4.9).

parallel conversion, the circuit in Fig. 4.14b is obtained with $C_p \approx C_c$ and $Z_p = 1/[(\omega_0 C_c)^2 Z_c|_{\omega=\omega_0}]$. We can typically neglect C_c against C and arrive at

$$Q_{ext} = \omega_0 C Z_p = \frac{1}{k^2 Q_c} = \frac{R_l}{k^2 \omega_0 L_l}. \tag{4.9}$$

Eq. (4.9) also suggests infinite damping at ω_0 for $R_l = 0$, but we know that for $Q_c > 1/k$ the cavity mode is merely split into two impedance peaks. If for example under-critical coupling to a cavity resonance is achieved for a certain value of R_l, it is obvious from Eq. (4.9) that when the coupling k is kept constant, R_l needs to be reduced to obtain critical coupling.

In the following, above theory is applied to the 630 MHz HOM coupler with the goal to couple critically to the two high-R/Q, $14\pi/33$ and $5\pi/11$ HOMs. The first step would be the compensation of the parasitic pickup capacitance. The electric pickup has however already an inherent inductive component in its post which is in series with the characteristic impedance of the coaxial coupler. The circuit in Fig. 4.12 with a compensation of the stray capacitance C_s in series with the load resistance R_l therefore correctly models the 630 MHz HOM coupler and is directly applicable. Figure 4.15 shows the surface currents on the HOM coupler for the TS_{31} $5\pi/11$-mode. The surface current on the pickup shows the characteristic distribution of an open-ended $\lambda/4$-resonator. This

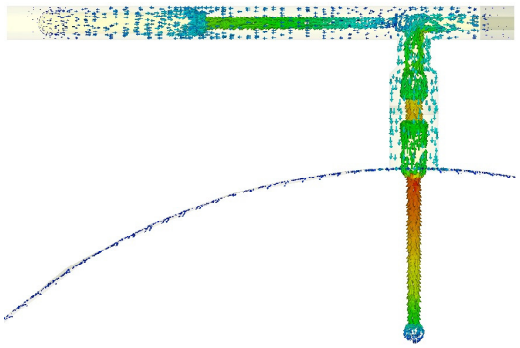

Figure 4.15.: Surface current distribution on the HOM coupler and its resonant pickup around 630 MHz. Color-coding on a logarithmic-scale.

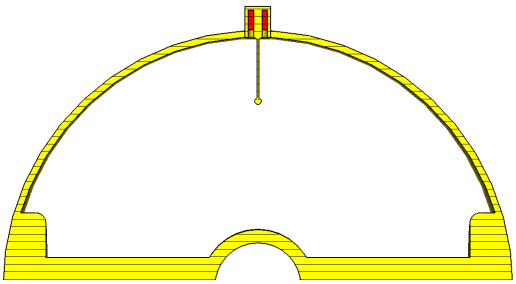

Figure 4.16.: Periodic unit-cell approach for optimisation of the coaxial HOM coupler and load impedance by variation of their inner conductor diameter.

means that the pickup of the existing HOM coupler with a length of $l \approx 105\,\text{mm} \approx \lambda/4$ is in fact already resonant around 630 MHz. This inherent compensation of the parasitic reactance explains the very good performance of the HOM coupler although it is merely terminated with its characteristic impedance of R_l=50 Ω and not also an additional inductive load (L_l in Fig. 4.12). The modification of any pickup dimension deteriorates the HOM coupler performance. Simulations presented in the following will show that critical coupling to the high-impedance HOMs is however not achieved with the load impedance of R_l=50 Ω. Following Eq. (4.9), we must now reduce the coupler and load impedance R_l to optimise the HOM coupler. This increases Q_c and brings the coupler closer to the point of critical coupling to these HOMs.

Most efficient and convenient optimisation of the load impedance for the $^{14\pi}/_{33}$ and $^{5\pi}/_{11}$ HOMs can be accomplished via a unit-cell simulation with periodic boundaries. The fundamental rejection filter of the HOM coupler behaves as an open-circuit at 630 MHz and can therefore be discarded for this optimisation, see Fig. 4.16. The implementation of the resistive load in this periodic setup is only possible via the lossy PML developed in Section 3.7.2. The load impedance presented to the HOMs by the coupler can then simply be varied via the diameter of the inner conductor of the coaxial load, cf. Eq. (3.28). A magnetic symmetry in the vertical-longitudinal plane can also be exploited, allowing rapid load optimisation for the TS_{31}-HOMs.

Figure 4.17 shows the results of the coupler impedance sweep for the 630 MHz HOMs with $^{14\pi}/_{33}$ and $^{5\pi}/_{11}$ phase advance per cell, respectively. Although Eq. (4.9) suggests a reduction of the

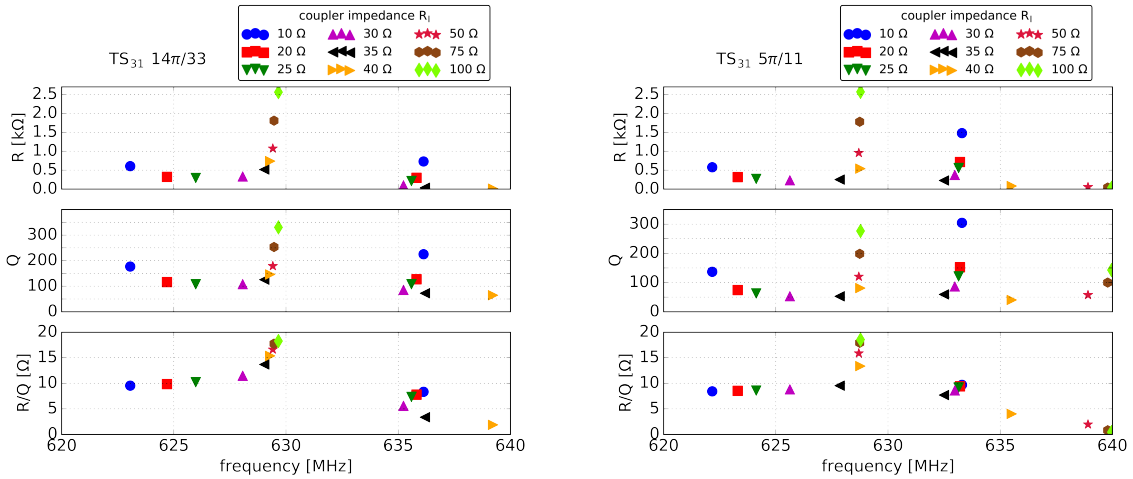

(a) TS_{31} $^{14\pi}/_{33}$ HOM.

(b) TS_{31} $^{5\pi}/_{11}$ HOM.

Figure 4.17.: Shunt impedance R, quality factor Q and geometry factor $^{R}/_{Q}$ as function of the HOM coupler and load impedance R_l in the simulation setup of Fig. 4.16.

load impedance, the results for values larger than 50 Ω are also shown to demonstrate the expected deterioration of the coupler performance for these values. The conclusions for the $^{14\pi}/_{33}$ HOM that can be drawn from the analysis of Fig. 4.17a are listed in the following:

- Only a single eigenmode is found by the unit-cell simulation in the frequency range from 620 to 640 MHz in case of a load impedance of R_l=50 Ω or higher, cf. Fig. 4.17a. The increase of the impedance R for R_l>50 Ω suggests under-critical coupling to the HOM and is correctly predicted by the circuit model in Fig. 4.12 and Eq. (4.9).

- For a load impedance of 40 Ω an additional eigenmode at around 639 MHz is found, which has however a small $^{R}/_{Q}$ and a negligible overall impedance R.

- Lowering the load impedance R_l further, gradually increases the impedance R of the additional mode, now around 635 MHz. This is predicted by the circuit model in Fig. 4.12 and the transition between critical and over-critical coupling is fluent.
- Lowest overall shunt impedance is obtained around a load impedance R_l of 20 to 25 Ω. Compared to the case of R_l=50 Ω the shunt impedance is lowered and distributed over a wider frequency range.
- The shunt impedance of the two modes increases when lowering the load impedance even further, see e.g. R_l=10 Ω in Fig. 4.17a. This is in accordance with two over-critically coupled resonators.
- The circuit model in Fig. 4.12 correctly predicts the behaviour and performance of the 630 MHz HOM coupler for different coupler impedances. The inductive component of the electric pickup compensates its stray capacitance in series with the coupler impedance. For a parallel type of compensation the behaviour for different coupler impedances would be inverse.

The situation for the high-R/Q mode with $5\pi/11$ phase advance is shown in Fig. 4.17b and the analysis can be conducted analogously. Lowest shunt impedance in the 630 MHz frequency range is achieved around a load impedance of 30 to 35 Ω for this mode.

Following the explanations given above, the improved impedance mitigation can be implemented by redesigning the existing HOM coupler to a characteristic impedance of around 25 to 30 Ω. The fundamental rejection filter does not necessarily have to be touched. It is however desirable to avoid a change of the coupler geometry due to the large number of couplers already deployed today (72 in total) as well as those already in manufacture for the upgrade ($\approx$ 120 in total). Besides the attempt to limit the number of variations in coupler designs, especially a replacement of the ceramic RF windows comes with large costs. Alternatively, the desired characteristic impedance can also be implemented by deploying loads with a complex input impedance on the HOM coupler output ports. The complex impedance must then be transformed via the 50 Ω transmission line of the coupler to the desired impedance seen by the HOMs at the base of the electric pickup. To choose the complex load correctly, knowledge of the electrical length from the load port to the pickup is required. In practice, a 25 Ω-equivalent impedance at the pickup is easiest to realise; two 50 Ω resistors can then be placed in parallel and connected in series with a piece of 50 Ω coaxial line of correct length. A 25 Ω-equivalent load impedance will therefore also be used in simulations of the full 33-cell structure. More details on the design procedure of the complex load for the existing 630 MHz HOM coupler are given in Section 5.3. The design and implementation for the EM simulations shown in the following is essentially identical. The complex load implementation will have a lower bandwidth than coaxial couplers with a 25 Ω characteristic impedance and the impact of the design change on the broadband damping performance of the HOM coupler must be verified as well.

Figures 4.18 and 4.19 show the HOM-mitigation performance of the complex loads when placed on all couplers. A strong improvement is observed in the eigenmode results and the loaded

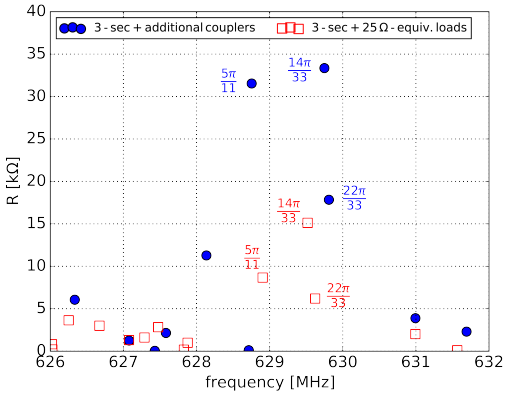

Figure 4.18.: Shunt impedance R in the 630 MHz frequency range of 33-cells with the HOM damping configuration illustrated in Fig. 4.5 without and with 25 Ω-equivalent complex loads deployed on the HOM couplers respectively. Results obtained from eigenmode simulations.

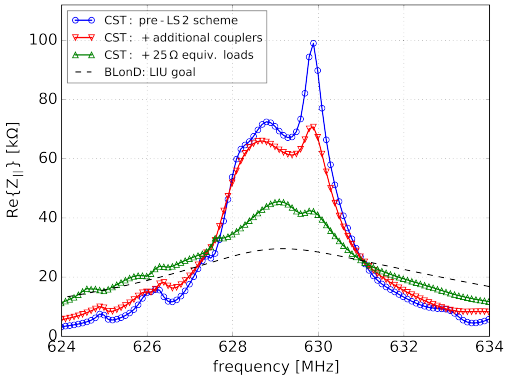

Figure 4.19.: Real part of longitudinal beam coupling impedance $Z_{||}$ in the 630 MHz frequency range of 33-cells with HOM damping configurations illustrated in Fig. 3.26b and Fig. 4.5. The 25 Ω-equivalent complex loads are deployed on all HOM couplers. Results obtained from wakefield simulations.

quality factors of the $14\pi/33$, $5\pi/11$ and $22\pi/33$ HOMs are now 246, 234 and 1060 respectively. While the Q_l of the high-R/Q modes are now very low for a cavity of this type, the Q_l of the $22\pi/33$-mode is basically unchanged compared to the case with 50 Ω loads. The reduced impedance of this mode in the eigenmode simulation is due to a reduction of its R/Q together with a shift of its resonance frequency. The increased damping observed in the eigenmode result does not translate entirely to the wakefield simulation, see Fig. 4.19. The decay time of the damped HOMs now approaches the transit time of the beam through the long, 33-cell structure. Contrary to the eigenmode calculations, the time domain wakefield simulation properly takes into account transients which become more important in this regime. In eigenmode simulations the R/Q is simply calculated via the steady state stored energy in the overall volume, not taking into account effects due to the quite complicated accelerator structure. Nevertheless, a good impedance mitigation due to the complex loads can also be observed in Fig. 4.19. We notice however also an increased impedance below 627 MHz and above 631 MHz which is a result of the slight overcritical coupling already observed in Fig. 4.17. This means that part of the impedance reduction is not due to damping, but rather due to a re-distribution of the impedance over a wider frequency range. This known effect of impedance broadening is a typical feature. The overall mitigation remains very beneficial for the intensity threshold of the multi-bunch instability. Improved damping by the deployment of complex impedance loads is also confirmed by RF measurements which are reported in Section 5.3.

Note that the impedance presented by the complex loads to the HOMs is frequency dependent. The damping performance of the pre-LS 2 damping scheme is therefore compared with that of the additional HOM couplers combined with the 25 Ω-equivalent (at 630 MHz) complex loads

up to 1 GHz in Fig. 4.20. The complex loads are also beneficial for impedance mitigation at other

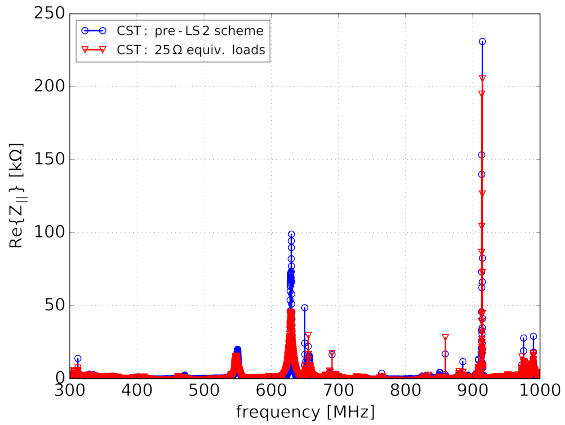

Figure 4.20.: Calculation of longitudinal beam impedance $Z_{\parallel}$ of the configuration illustrated in Fig. 4.5 demonstrating the impact of 25 Ω-equivalent complex loads on the broadband damping performance of the TS_{31} HOM coupler (red). Comparison to the pre-LS 2 scheme with 50 Ω loads illustrated in Fig. 3.26b (blue).

frequencies and no serious deterioration of the impedance situation can be observed over the spectral range of interest. The FPB is not influenced by the complex loads as the rejection filter works independent of the connected load impedance. The complex loads perform even better on 44-cell configurations, cf. Appendix D. In that case, the LIU impedance goal can almost be attained by deploying complex loads on the pre-LS 2 damping configuration alone, without having to add more HOM couplers.

4.4. Constraints on HOM Impedance Mitigation

The loaded quality factors of the two high-R/Q HOMs are around 230 when the optimised couplers developed in the previous section are deployed. This is a very low value for this type of structure and it is questionable that it can be reduced significantly further. An inherent limitation is the structural top-bottom asymmetry that is a result of the numerous HOM couplers placed on top of the TWS in the new damping scheme, see Fig. 4.5. It was illustrated in **[44]** that due to this asymmetry large parts of the energy of damped HOMs are stored in the lower half of the TWS. As there is no counterweight to the numerous couplers on top, the EM fields are pushed into the lower half of the cavity where they become inaccessible to the HOM couplers. Only two access ports exist in the lower half of the structure dedicated to HOM damping and they are situated on the two end-plates. An electric HOM coupler pickup was developed in **[58]** that can partially suppress the effects caused by the asymmetry. Improving the damping of the high-R/Q HOMs merely via the two end-cells is however infeasible as the EM fields in all other cells remain unmodified. Machining

of the sections to create additional access ports in the bottom is out of the question as damage can not be excluded beforehand and vacuum tightness later on cannot be guaranteed [63].

The last option to access the lower part of the structure is then via vacuum pumping ports (VPPs) of which each 11-cell section features three, below cells three, six and nine, see Fig. 3.7. Each VPP features a honeycomb grid in the inner copper layer of the cavity with a hole diameter of 18.5 mm, refer to Fig. 4.23a, and which is impenetrable for the 200 MHz fundamental mode. Machining of the honeycomb grid is most likely required to place HOM couplers in some of the VPPs. The vacuum is however sealed on the outer flanges of the VPPs so that vacuum tightness does not pose a problem. Nevertheless, the operation appears to be mechanically demanding if damage to the copper layer has to be excluded. Still, this option was studied, assuming that the installation of HOM couplers in some VPPs is feasible. Figure 4.21 illustrates the placement of three 630 MHz couplers in cells which show strong electric field of the high-R/Q HOMs and which are equipped with a VPP. The performance of this damping scheme as obtained from a wakefield

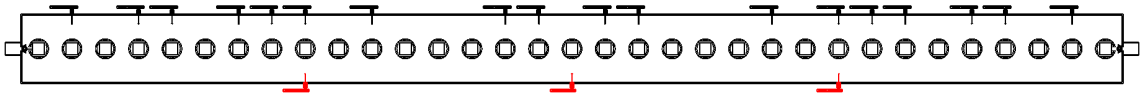

Figure 4.21.: Illustration of a 33-cell structure with the pre-LS 2 damping scheme, the additional HOM couplers in the top and three couplers in VPPs in the bottom (red). On all HOM couplers 25 Ω-equivalent complex loads are deployed.

simulation is reported in Fig. 4.22. Due to the existing field densities, the placement of HOM

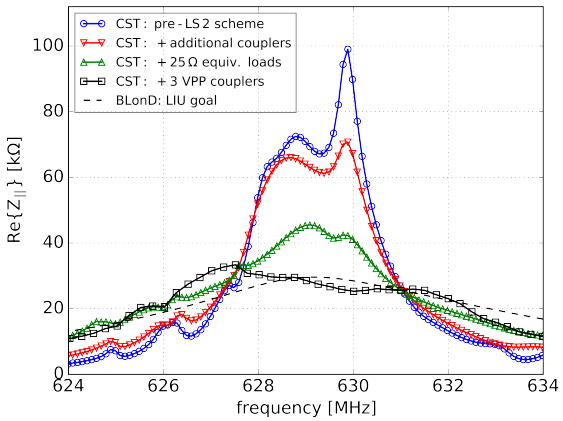

Figure 4.22.: Real part of longitudinal beam coupling impedance $Z_{||}$ in the 630 MHz frequency range of 33-cells for different damping configurations. The impedance for the case that three HOM couplers are used in VPPs as illustrated in Fig. 4.21 is equal or below the LIU goal for large parts of the frequency range. Results obtained from wakefield simulations.

couplers in the bottom is highly effective and the LIU goal can already be reached over large parts

of the frequency range of interest. Three couplers have been placed and these act as a counterweight to the numerous HOM couplers on top and avoid that large parts of the HOM energy are stored in the bottom of the structure where it is otherwise inaccessible. It is likely that with slight optimisations of this damping scheme the LIU goal can be fully reached. This option has however not been studied any further in the frame of this thesis after the achieved damping results of the complex loads were discussed on a project management level and have been considered sufficient. Nevertheless, it remains as a possible option to be revisited once the full impact of the ongoing impedance reduction measures can be investigated with beam after the restart of the accelerator complex.

Improvement over the damping scheme proposed in the previous section can also be achieved with the pedestal coupler proposed in **[58]**. This coupler can also mitigate the high-Q HOMs of the upper TS_{31} passband like the $^{22\pi}/_{33}$-mode. To deploy this coupler, merely the pedestal of a drift tube and stem assembly needs to be machined which is less risky than machining the VPP of a full section. However, as machining of any structure parts shall ultimately be avoided, these couplers were so far not studied in further detail nor was their performance verified by RF measurements.

4.5. Resonant Posts for HOM Impedance Mitigation

As was explained before, it is highly desirable to avoid mechanical interventions on the TWSs, but nevertheless mitigate the effects of the top-bottom asymmetry discussed in the previous section. Instead of the classic HOM mitigation primarily through damping of the quality factors one could also devise a mitigation by directly targeting the geometry factor $^{R}/_{Q}$ of the HOMs. This would mean a change of the TWS geometry which in our case would be preferable in the lower part of the structure to also mitigate the asymmetry effects. Especially the $^{14\pi}/_{33}$ HOM at 630 MHz should be suppressed as it is fully synchronous with the particle beam resulting in its large $^{R}/_{Q}$.

Ideally, we would like to introduce a stop band around 630 MHz in the dispersion diagram of Fig. 3.16. The TS_{31} modes around 630 MHz are HOMs of the TS_{11} FPB and therefore the equivalent circuit of Fig. 3.12 for multi-stem drift tube structures can also serve as a basis for describing the HOMs. A stop frequency can be introduced in the stem passband represented by C_s and L_s by placing a series resonant circuit in parallel to the stem resonator in every cell. This series resonator behaves as a short circuit between drift tube and outer cylinder at its resonance frequency ω_p, separating the passband of the stem resonance in two. At frequencies below ω_p the series resonance behaves capacitively, lowering the stem resonance ω_s. At frequencies above ω_p the series resonance is inductive, increasing ω_s.

The introduction of such an additional resonator is well known from drift tube LINACs operated in the 0-mode; refer back to Fig. 1.4. Such LINACs are very susceptible to manufacturing tolerances and suffer from poor field stability due to the zero group velocity in the lossless limit. By placing so-called post couplers in all cells, an additional post-coupler passband is created which can be tuned into confluence with the accelerating mode band. This effectively turns the sensitive

0-mode LINAC into a stable $\pi/2$-mode like structure with non-zero group velocity at the operating mode [7, 64]. Refer also back to the end of Section 1.1 in this regard.

In our case, we would like to use such post resonators not for a stabilisation of the FPB, but for the suppression of HOMs **[58]**. In the lower part of the structure we merely have access to three VPPs per 11-cell section, see Fig. 3.7. A relatively broadband post passband can therefore not be created as the coupling between the posts is very weak. Each VPP features a honeycomb grid in the inner copper layer of the cavity with a hole diameter of 18.5 mm as shown in Fig. 4.23a and which is impenetrable for the 200 MHz fundamental mode. As a suitable resonator the electric

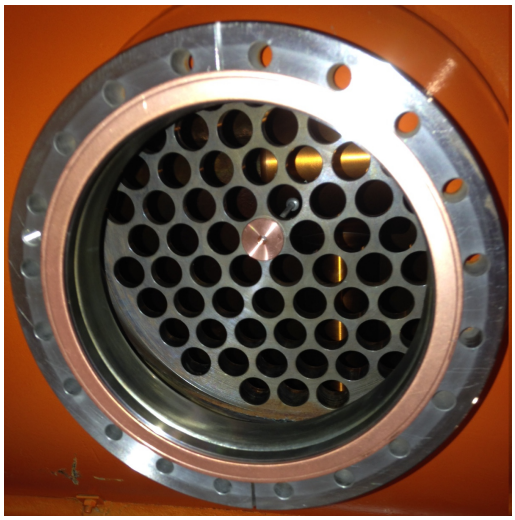

(a) VPP with honeycomb grid in the copper layer of the TWS. View through the VPP's flange opening. A resonant post is installed close to the centre of the grid below the drift tube of the cell.



(b) Resonant post assembly for installation in the honeycomb grid of VPPs. Left: Post assembled on a copper base with RF spring contact.

Figure 4.23.: HOM coupler pickups used as resonant posts in some VPPs of the TWS. The posts contribute to the mitigation of the high-R/Q HOMs and can act as a counter-weight to the numerous HOM couplers on top of the cavity. Machining of the accelerating structure to create additional access ports for HOMs is not required.

pickup of the TS_{31} HOM coupler can be reused which is already known to be resonant at 630 MHz from Section 4.3. The electric pickup can directly be placed in the honeycomb grid with good RF contact to the outer envelope by mounting it on a base which is equipped with an RF spring contact, see Figs. 4.23a and 4.23b.

The effect of the resonant posts on the TS_{31} HOMs is best demonstrated by loading a long piece of the TWS envelope with a single drift tube and stem assembly **[58]**. Figure 4.24a shows the typical field profile of the stem resonator which is not supported by the bare circular waveguide. With the resonant post in place as shown in Fig. 4.24b, energy can not be stored in the bottom part of the cell as the electric field is short-circuited to the cavity envelope. The surface current on the post again

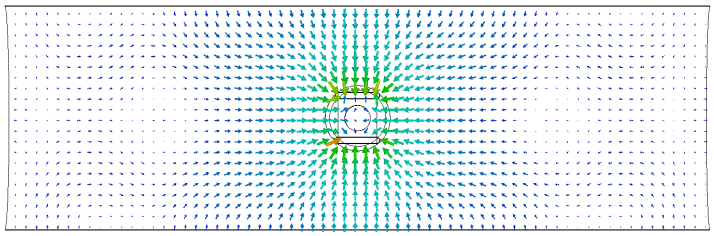

(a) TS_{31} stem resonance at 629.8 MHz.

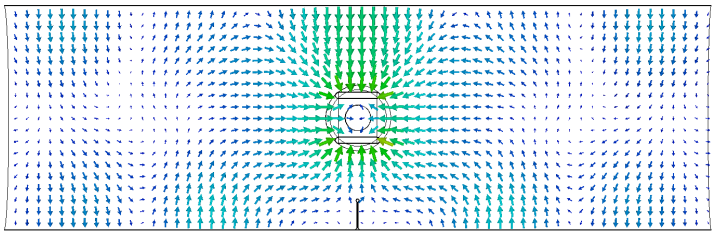

(b) TS_{31} stem resonance perturbed by a resonant post.

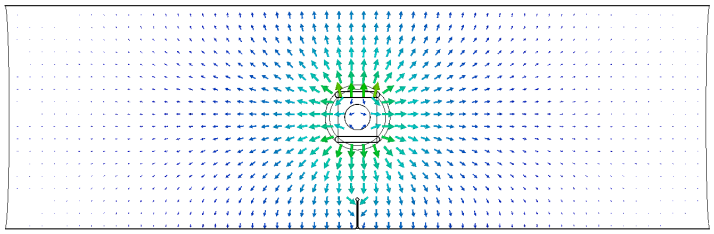

(c) Fundamental TS_{11} stem resonance at 205.2 MHz unaffected by post resonant at 630 MHz.

Figure 4.24.: Electric field profiles in a long piece of circular envelope loaded by a single drift tube and stem assembly. Field magnitudes are color coded on a logarithmic scale.

shows the $\lambda/4$-distribution. The R/Q of the stem resonance in Fig. 4.24 calculated over the length of the cell is reduced from 18 Ω for the unperturbed case to 13.5 Ω for the case with resonant post in place; a reduction by 25 %. In addition, the electric field strength increased above the drift tube in the place of the access ports for HOM couplers, cf. Figs. 4.24a and 4.24b. In the equipped 33-cell structure the posts avoid EM fields from being pushed into the lower half of the structure making them inaccessible to the HOM couplers. Thereby, the resonant posts act as a counter weight to the numerous couplers on top of the structure making these also more effective. The above described effects can be explained by the fact that the displacement current picked up by the resonant post is shorted to the outer envelope of the cavity. For the case of multi-cell structures also the coupling mechanism to the neighbouring cells is partially suppressed in this manner. Resonant posts may not perturb the fundamental accelerating mode significantly. The field profile of the FPB under the influence of a resonant post is shown in Fig. 4.24c. As the post is not resonant at 200 MHz, it does not have a significant impact on its field profile. A more in-depth analysis by RF measurements on how resonant posts influence the FPB follows in Section 5.6.

Note that the resonant posts are most effective in cells with relatively strong electric field whereas VPPs are only available in cells 3, 6 and 9 of each 11-cell section. Adequate cells for deployment of resonant posts in 33-cells were manually determined by inspection of the simulated $^{14\pi}/_{33}$ and $^{5\pi}/_{11}$ electric field profiles. The total number of resonant posts was limited to three to keep the impact on the fundamental mode at an acceptable level. Consequently, the posts are deployed in cells 9, 17 and 25 as illustrated in Fig. 4.25. Figures 4.26 and 4.27 show the beam im-

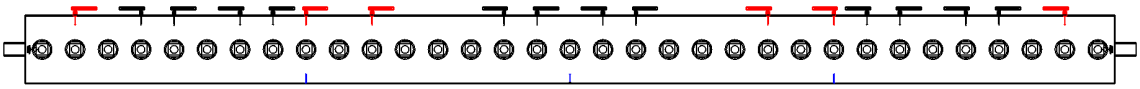

Figure 4.25.: Illustration of 33-cell structure with the proposed, new damping scheme for the TS_{31}-HOMs. Six HOM couplers (red) and three resonant posts (blue) are added to the existing, pre-LS 2 damping scheme. On all HOM couplers 25 Ω-equivalent complex loads are deployed.

pedance results obtained from eigenmode and wakefield simulations for the new damping scheme including the three resonant posts. Both solvers show a strong impedance reduction in a narrow

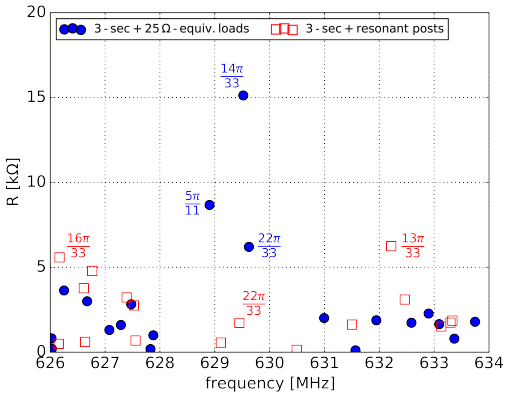

Figure 4.26.: Mitigation of shunt impedance R in the 630 MHz frequency range of 33-cells due to the addition of three resonant posts to the HOM damping scheme as illustrated in Fig. 4.25. Results obtained from eigenmode simulations.

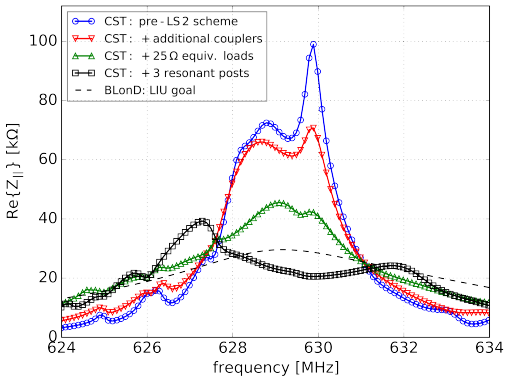

Figure 4.27.: Real part of longitudinal beam coupling impedance $Z_{||}$ in the 630 MHz frequency range of 33-cells for different damping configurations. The impedance for the newly proposed damping scheme illustrated in Fig. 4.25 is shown in black. Results obtained from wakefield simulations.

band around 630 MHz at which the posts are resonant. The two former high-$^{R}/_{Q}$ $^{14\pi}/_{33}$ and $^{5\pi}/_{11}$ HOMs are effectively mitigated. However, the resonant posts alter the boundary conditions and other mode profiles become favourable for energy storage. Some of the impedance is therefore merely distributed to lower and higher frequencies at 627 and 632 MHz. The impedance especially in the $^{16\pi}/_{33}$ and $^{13\pi}/_{33}$ HOMs is slightly increased, cf. Fig. 4.26. The resonant posts are not effective on these modes as they feature weak electric field in the three cells equipped with posts.

The distribution of impedance over a wider frequency range is again beneficial for mitigating the multi-bunch instability. Although the peak impedance is only slightly reduced by the resonant posts, see Fig. 4.27, comparing the area under the impedance curves with and without posts shows a reduction of overall impedance in the frequency range around 630 MHz. It is also interesting to compare the performance of the three resonant posts with that of HOM couplers placed in the same positions, refer back to Fig. 4.22. The resonant effect of the electric pickup (used as resonant post and as pickup on the HOM coupler) in the 628 to 630 MHz range is more pronounced in case of the posts. Merely for the impedance peak at 627 MHz the HOM couplers show a better performance due to their ability of damping the quality factors. Note that in spite of the positive effect, the LIU impedance goal still cannot be fully reached by the resonant post configuration. However, couplers for the mitigation of transverse HOMs around 938 MHz will also have to be incorporated into the damping scheme. The LIU goal is then likely to be reached by a final optimisation of the scheme using the mitigation techniques developed in the previous sections. Deployment of some coaxial HOM couplers with a 25 Ω characteristic impedance instead of using the more narrowband complex loads is also likely to improve the situation further. The possibility of impedance mitigation by resonant posts is confirmed via RF lab measurements carried out on a single section of which the results are shown in Section 5.4.

It has to be ensured that the insertion of resonant posts does not lead to an increased impedance at other frequencies relevant for beam stability. Impedance might merely be re-distributed to other frequencies, as especially the high-R/Q HOMs are targeted by the posts. The wakefield results up to 1 GHz for the proposed 33-cell damping scheme including the posts are shown in Fig. 4.28. No

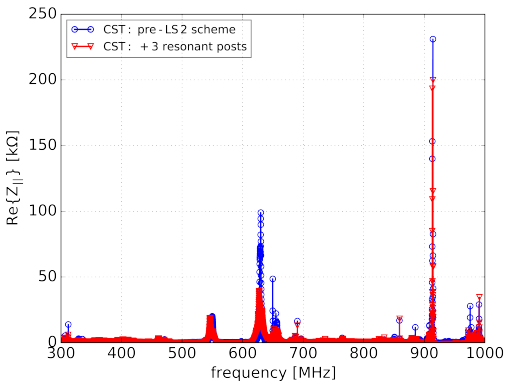

Figure 4.28.: Broadband damping performance of the newly proposed damping scheme for the TS_{31} HOMs around 630 MHz in comparison to the pre-LS 2 damping scheme. No serious increase of HOM impedance at other frequencies is observed.

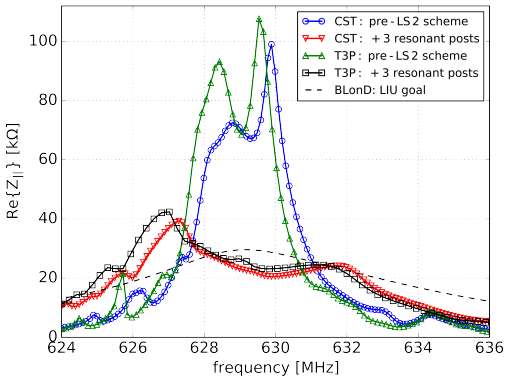

Figure 4.29.: Comparison of wakefield simulation results obtained from CST and T3P solvers for the pre-LS 2 and the newly proposed longitudinal damping schemes. Both solvers suggest a similar peak to peak factor of impedance mitigation.

serious deterioration of the impedance situation over the spectral range of interest can be observed. The different HOM coupler schemes were also simulated with the wakefield solver of ACE3P

(T3P) to confirm the achieved impedance mitigation. A comparison between the wakefield results of CST and T3P for the new damping scheme is reported in Fig. 4.29 in addition to the comparison for the pre-LS 2 damping scheme already discussed together with Fig. 3.25b. The two solvers are in good agreement for the improved damping scheme. Both codes also suggest a similar peak to peak factor for the additional impedance mitigation of the TS_{31} HOMs that is achieved by the new damping scheme.

4.5.1. Multi-Physics Considerations of Resonant Posts

Thermal Analysis

The RF and thermal contact of the resonant posts is merely ensured via the small silver plated, copper spring shown in Fig. 4.23b (torus with a 3.5 mm tube diameter and an outer diameter across of about 20 mm). Power loss occurs on all surfaces of finite conductivity in the cavity due to induced surface currents which eventually result in the generation of heat. A possible overheating of the resonant posts must be evaluated pre-emptively to ensure safe machine operation. The heating of the posts that is to be expected is analysed in the following by means of coupled EM-thermal simulations performed with CST [42]. At first, two sources of post heating can be anticipated. The RF generators will inject a large power of 1.05 MW peak into the 33-cell structures for particle acceleration. In addition, the high intensity beam induces power over a large frequency band at every pass through the TWS. It will however be clarified later on that a contribution to the heating from the beam has in fact not to be expected.

The focus is first on the power loss induced in a resonant post by the RF generators in the $\pi/2$-mode of the FPB. For best computational efficiency, the unit-cell setup with periodic boundaries is used once again also for this thermal simulation. The cell is equipped with a resonant post and the 630 MHz HOM coupler must also be included to obtain the typical operating conditions for the post in practice, see Fig. 4.30a. The thermal properties of cell, post and coupler (yellow) are those of copper. The RF window (grey) of the 630 MHz HOM coupler is made of an alumina ceramic. The filter and load part of the HOM coupler is filled with air (green).

The winding separation of the torus-like RF spring contact is 0.1 mm, refer to Fig. 4.23b. When installed, the spring is compressed between the outer cavity cylinder and the mount of the resonant post, refer to Fig. 4.23a. Exact modelling of the RF spring would be very laborious, even with a tetrahedral mesh and is not required in this case. Instead, a simplified simulation model for the RF and thermal contact is employed which is shown in Fig. 4.30b. There, the spring is modelled by a flattened torus (blue) to take the compression into account. A filler material (black) with zero electric and thermal conductivity is used to avoid decoupled computation domains during simulation and to isolate the mounting base from the inner copper layer (yellow) of the cell. The background of the simulation was given the thermal properties of the steal cavity envelope.

A conservative estimation has been chosen for the surface area at which the RF spring touches the mount and the cavity cylinder. The typical thermal conductivity for the copper spring is

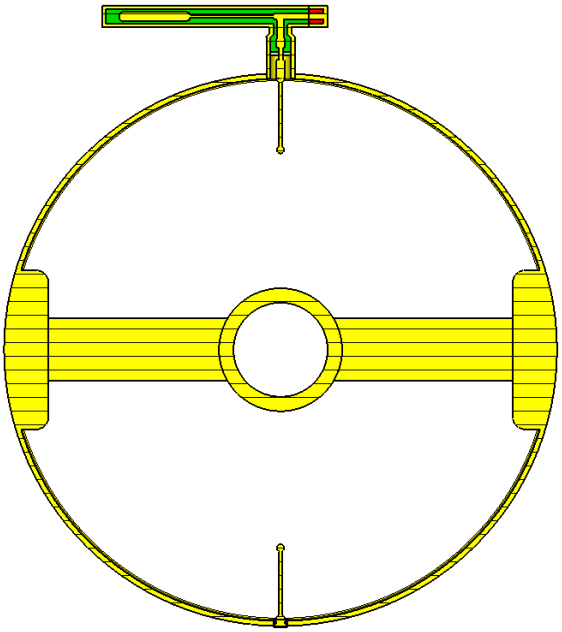

(a) Cross-section of the unit-cell model including the 630 MHz HOM coupler and resonant post. The filter part of the coupler is filled with air (green) and the RF window (grey) is made of an alumina ceramic. The 50 Ω load of the coupler (red) is implemented by the PML developed in Section 3.7.2.

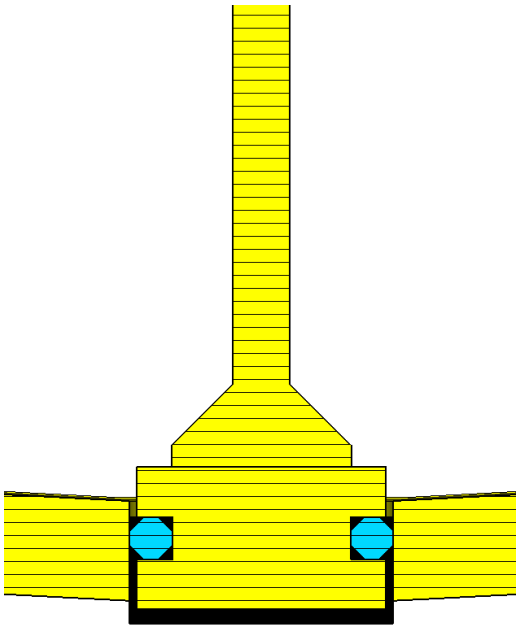

(b) Detailed view of the implementation of the RF spring contact (see Fig. 4.23b) in the simulation model. The spring is modelled by the flattened torus (blue) to take its compression into account. A filler material (black) with zero electric and thermal conductivity is used to isolate the base from the cavity.

Figure 4.30.: Simulation model for the analysis of thermal heating caused by RF losses on the copper surface (yellow) of the SPS TWS. The structure is evacuated and the simulation background is given the thermal properties of the steal cavity envelope. The ambient temperature is set to the cooling water temperature of around 20°C, however cooling circuits on the cavity envelope and in the stems are not taken into account.

401 W/K/m, however, as the spring is not solid (as modelled) and to account for the separated windings, the value is reduced to 80 W/K/m (20% of the original value). Like this, the simulated heating on the post will be too pessimistic, i.e. it will not be exact, but it is a good indicator for a possible heating issue. Figure 4.31 shows the simulated heat flow density that indicates a realistic heat transfer from three contact areas on the base of the resonant post via the RF spring to a single contact area on the copper layer of the cell. Cooling circuits on the cavity envelope and in the stems are not taken into account, but the ambient temperature in the thermal simulation is set to the temperature of around 20°C of the cooling water.

The power loss on the various surfaces with finite conductivity in the model is calculated by the eigenmode solver from the simulated magnetic field using Eq. (2.15). Note that the EM fields in any eigenmode simulation are normalised to 1 J of mean stored energy by CST. We can use Eq. (A.1) to scale the simulation results of the periodic unit-cell approach to the maximum input

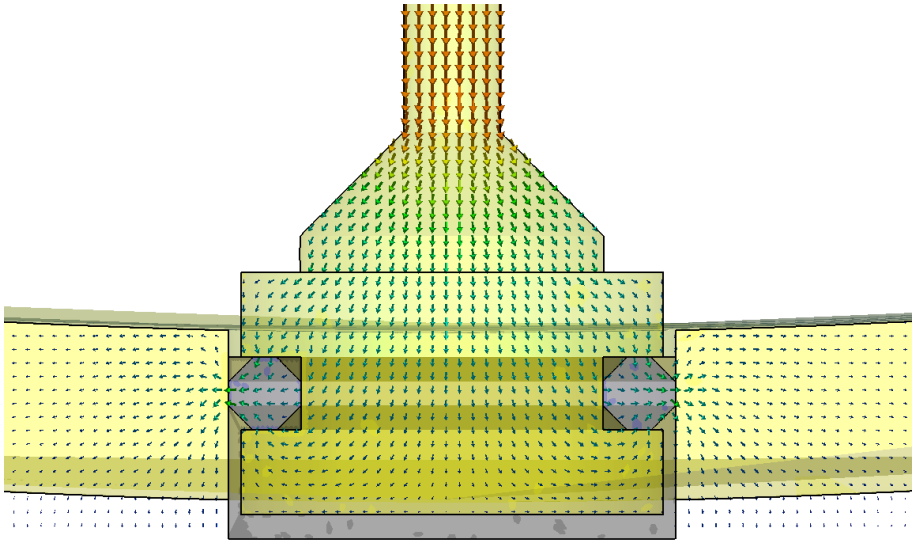

Figure 4.31.: Simulated heat flow density over the RF spring contact of the resonant post assembly in the accelerating TS_{11} $\pi/2$-mode. The heat transfer is from three contact areas on the base of the resonant post to a single contact area on the wall of the cell. Colour-coding is on a logarithmic scale.

power of 1.05 MW that is injected into the 3-section TWSs after LS 2. This travelling wave has a stored energy per unit length of 0.037 J/m. Then the energy U_c stored in one cell reads

$$U_c = \frac{P_{in} l_c}{v_g} = 0.0138\,\mathrm{J}\,, \tag{4.10}$$

which can be used to scale the power loss calculated by the eigenmode solver on different parts of the structure. The resulting values for the power loss of the TS_{11} $\pi/2$-mode are reported in Table 4.1. Note that more than 50% of the total power is lost on the surface of the stems. The power loss on the pickup of the 630 MHz HOM coupler and the resonant post is identical and of 1.1 W. This power will result in the generation of heat that needs to be diverted via thermal conduction to avoid overheating resulting in structural deformation.

For benchmarking, the results obtained via the unit-cell approach were confirmed by an S-Parameter simulation of a full, 33-cell structure at the frequency of the TS_{11} $\pi/2$-mode. In this case, the TWS was equipped with the matching networks developed and implemented in Sections 3.6.2 and 3.8.1 to ensure the travelling wave condition as well as the newly proposed damping scheme that includes the resonant posts. The EM fields were normalised to an input power of 1 W in S-Parameter simulations so that in this case scaling to the post-LS 2 input power of 1.05 MW for 33-cell structures is trivial. The results are listed in Table 4.1 as well and are in excellent agreement with the unit-cell simulation.

Table 4.1.: Power loss of the accelerating TS_{11} $\pi/2$-mode on different surfaces of the simulation models scaled to a continuous-wave input power of 1.05 MW. Individual power loss is reported for each pair of stems, the drift tube, the pickup of the 630 MHz HOM coupler and the resonant post. The results obtained from the periodic unit-cell approach and the full 33-cell structure including the newly proposed damping scheme are in excellent agreement.

	unit-cell P_{loss} [W]	**33-cells** P_{loss} [W]
stems	439	420
drift tube	39	38
pickup	1.1	1.1
post	1.1	1.1
rest	332	321

The RF loss distribution calculated by the eigenmode solver can be used in a coupled thermal simulation to generate a spatial temperature distribution. The thermal solver utilises the heat equation [16] to calculate heat transfer by conduction based on an initial temperature distribution and boundary conditions. For the case studied here, merely the steady state distribution was considered for a continuous-wave input power of 1.05 MW. But actually, for the LHC proton beam, the RF generators can be switched off for large parts of the 23 μs revolution period as only a fraction of the SPS ring is filled, cf. Table 1.1, and the cavity filling time is relatively small. The temperature distribution shown in Fig. 4.32 is therefore rather overestimated for this type of beam. Empirically and as a rule of thumb, the temperature of any cavity parts should stay below 80°C to avoid additional outgassing, even after previous bake-outs, and a deformation of cavity parts under their own weight [63]. In addition, it is known that the resonant frequency of the TS_{11} $\pi/2$-mode is very susceptible to changes in the stem diameter, cf. Section 3.5. Cooling of the stems via internal water pipes (not modelled) is therefore especially important to avoid a detuning of the structure due to heating. Compared to the drift tubes, the outer cavity cylinder stays relatively cool at values around 30°C except in the areas of the pedestals. The peak temperature on the HOM coupler pickup is calculated to 42°C and on parts of the 200 MHz notch filter values up to 47°C are reached. The tip of the resonant post heats up to 37°C whereas the base of the post assembly is at the same temperature as the cavity wall. Comparing also to the temperature distribution on the identical pickup of the HOM coupler, it can be seen that the heat transfer via the RF spring contact is sufficient for the given input power of 1.05 MW. The temperature distribution for an input power of 1.6 MW, which will be used for the post-LS 2 44-cell TWSs, is reported in Appendix E.

An additional heating due to the beam induced power in the frequency range of the FPB has in fact not to be expected. This is due to the peculiar property of the TWS in which the power loss of the beam merely reduces the RF power that would otherwise be terminated in the load. More details on this were given in Section 3.1. The power dissipated in the TWSs increases only slightly with beam loading [27].

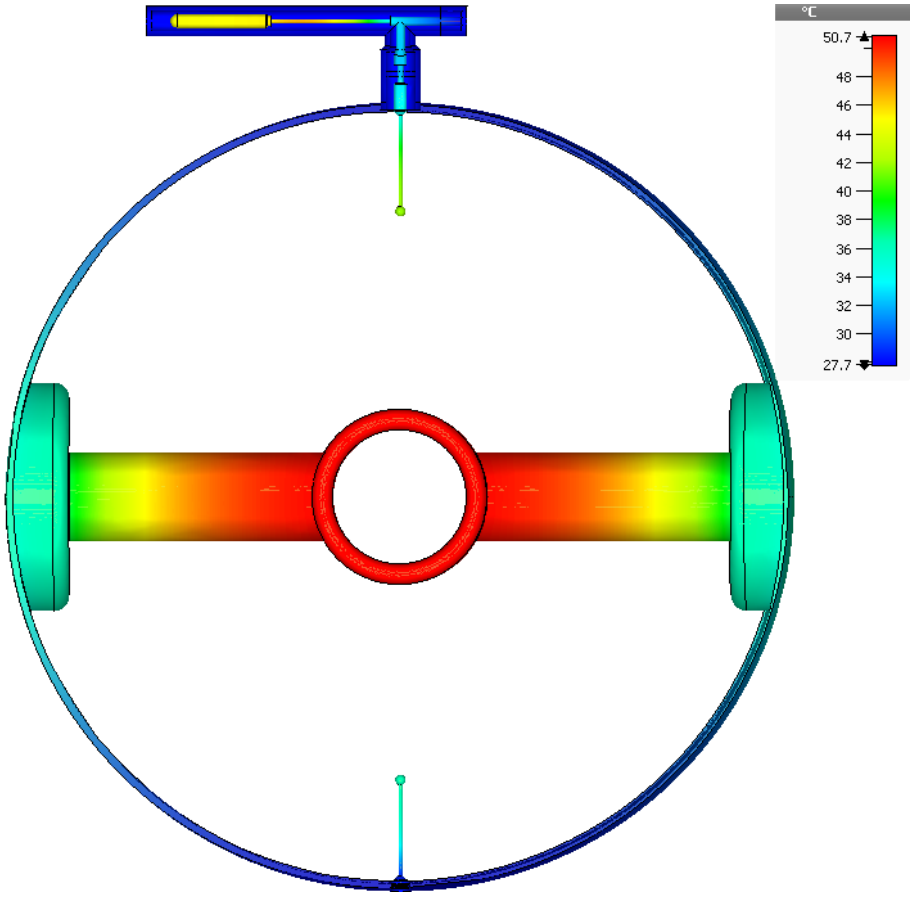

Figure 4.32.: Simulated, steady state temperature distribution in the SPS TWS as a result of a travelling wave in the TS_{11} $\pi/2$-mode with a continuous input power of 1.05 MW. The simulation setup is detailed in Fig. 4.30. Cooling pipes in the stems and on the cavity cylinder are not considered.

The TS_{31} HOMs are standing wave modes which are not terminated in the water load of the structure. The beam power loss around 630 MHz in the damped 33-cell structures is calculated to around 20 W using BLonD (refer back to Section 1.5), which in addition to the longitudinal impedance also takes into account the complicated spectrum of the LHC beam in the SPS, cf. Table 1.1. This contribution is small compared to the power injected into the fundamental mode by the RF generators. Eigenmode simulations show that at least 97% of the RF losses of all HOMs around 630 MHz are volume losses, meaning that the HOMs are damped almost entirely by the resistive load of the HOM couplers[1]. In addition, only a fraction of the remaining surface losses occurs on the resonant posts. Additional heating of the posts due to the HOMs is therefore not to be expected and the peak temperature of around 37°C on the tip of the resonant posts for a continuous-wave input power of 1.05 MW can be considered a valid estimate. No risks coming from an overheating

[1] apart from negligible volume losses in the RF windows of the HOM couplers

of the resonant posts is to be expected and safe machine operation can be ensured with a large margin.

RF Breakdown Analysis

Vacuum arcs forming a plasma can occur in accelerator structures operated at very high field gradients. This is also called RF breakdown. Arching in cavities is an entire field of studies of its own and, without going into greater detail, it is widely accepted that one critical factor for this phenomenon is the peak surface electric field as a cause for emission of electrons. Interaction of these electrons with residual gas molecules can lead to a sudden discharge of stored energy with deteriorating effects on the beam and the cavity surface itself. Refer to [13, 65] for more details on the breakdown process.

The peak surface electric field on the resonant posts is to be studied to ensure safe machine operation with the newly developed posts. The resonant posts also reduce the minimum gap size in the TWS which is however still large with around 20 cm. An empirical criterion for the maximum allowed field gradient to avoid sparking was established by W. D. Kilpatrick based on experimental observations [65]. The results were later recast into the more convenient formula

$$f[MHz] = 1.64 E_s^2 e^{-8.5/E_s}, \tag{4.11}$$

where E_s is the peak surface electric field [13, 66]. Above equation is known as the Kilpatrick

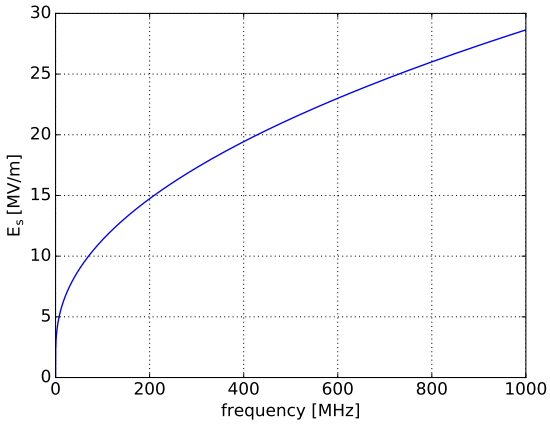

Figure 4.33.: Kilpatrick limit for RF breakdown with the peak surface electric field E_s as a function of frequency.

limit below which no RF breakdown is to be expected. The expression is merely limited by RF frequency, but not gap size, and visualised in Fig. 4.33. The peak surface electric field on the tip of the resonant post in the accelerating TS_{11} $\pi/2$-mode is simulated to 2.9 MV/m for an input power of 1.6 MW. This is far below 1 kilpatrick which is also considered quite conservative nowadays. In

comparison to standing wave cavities, TWSs typically have a lower gradient due to the relatively low stored energy. To conclude, the resonant posts are not expected to increase the risk of RF breakdown in the SPS TWSs.

5. RF Measurements on the Parallel Stem Structure

The results of the two simulation codes CST and ACE3P for the performance of the new HOM mitigation scheme developed in Chapter 4 are in good agreement. Further confidence in the damping performance of the newly proposed mitigation solutions can be obtained by confirming the simulation results with RF measurements. As a fully equipped 33-cell structure was not available, the measurements were carried out on 11-cell sections. Most notably, the complex impedance loads are designed and tested in Section 5.3 and the performance of the resonant posts is verified in Section 5.4. A method to measure the impact of HOM mitigation devices on the accelerating mode is proposed in Section 5.5 and applied to the TWSs used in the SPS before LS 2 in Section 5.6.

5.1. Resonant Perturbation Measurements of Axial Electric Field

The three independent parameters resonance frequency f_0, quality factor Q and geometry factor R/Q are required to fully describe a standing wave resonator, cf. Eq. (2.8). These parameters can be determined for each cavity resonance from RF measurements. To determine the R/Q, the on-axis electric field needs to be measured, cf. Eq. (2.12). This is possible by using perturbation techniques in which a small perturbing object is moved along the beam path inside the cavity while the position dependent shift in resonance frequency is recorded [67, 68]. From this shift the electric field strength at each position of the perturber can be determined. This measurement method is also known as bead pulling. In the following, merely the perturbation theory for measuring a resonant cavity is shown and later on applied to the SPS TWS for verification of the EM simulation models. Non-resonant perturbation measurements to determine the electric field of a travelling wave, as e.g. described in [69], are also possible and especially interesting for the fundamental mode of TWSs. Application to the full SPS 200 MHz TWS is however very cumbersome if not infeasible due to the extreme length of this structure and was hence not carried out.

5.1.1. Perturbation Theory

A perturbing object in a resonant cavity is polarised by the EM fields in the structure. This causes an unbalance in the electric and magnetic stored energies and therefore a shift in the resonance frequency of the cavity which restores this balance. The dimensions of the perturber should be

small compared to the wavelength as in this case the field close to the perturber can be assumed in good precision as uniform and static. This allows to solve for the EM fields of the polarised perturber that modifies the cavity fields. The frequency shift $\Delta\omega$ of a cavity resonance due to a perturbing object is given by

$$\frac{\Delta\omega}{\omega_0} = \frac{1}{U}(-K_1\varepsilon_0 E_\parallel^2 - K_2\varepsilon_0 E_\perp^2 + K_3\mu_0 H_\parallel^2 + K_4\mu_0 H_\perp^2), \tag{5.1}$$

where U is the stored energy and E and H the peak electric and magnetic field components parallel and perpendicular to the perturber [10, 70]. The coefficients K_1 to K_4 are proportional to the geometry and the electric or magnetic polarisability of the perturber respectively. For a perturbing object that impacts mostly the longitudinal $E_\parallel$ field component, Eq. (5.1) simplifies to

$$\frac{\Delta\omega}{\omega_0} \approx \frac{1}{U}(-K_1\varepsilon_0 E_\parallel^2). \tag{5.2}$$

In general, such an object can be a long, dielectric cylinder that interacts only with the electric field. However, in the case that the longitudinal magnetic field of the mode is weak, also a metallic cylinder can be used as the resonance frequency is not significantly perturbed by the magnetic field. The coefficient K_1 can be related to the electric polarisability $P_\parallel/(\varepsilon_0 E_\parallel)$ of the perturbing object of length $2l$ via

$$K_1 = \frac{1}{4}\frac{P_\parallel}{\varepsilon_0 E_\parallel} = \frac{\pi}{3} l^3 G, \tag{5.3}$$

where $P_\parallel$ is the electric dipole moment induced by the external electric field [71]. The dimensionless form factor G depends on the shape of the perturber. For a hollow, metallic cylinder with radius a the appropriate form factor was deduced in [70] to

$$G_{cyl} = \sinh^{-1}\left(\frac{2}{3\pi}\frac{l}{a}\right). \tag{5.4}$$

The frequency shift at each position of the perturbing object inside the cavity could be measured directly by tracking the peak of the resonance curve obtained from the transmission measurement S_{21}. For small perturbations however this can be impractical so that usually the more sensitive phase shift $\Delta\phi$ of the transmitted signal is measured instead. The frequency shift is then indirectly obtained from the relation [68, 70]

$$\frac{\Delta\omega}{\omega_0} = \frac{1}{2Q_l}\tan(\Delta\phi) \tag{5.5}$$

where Q_l is the loaded quality factor of the resonance. With the axial electric field $E_\parallel$ of a cavity at hand, the R/Q and R can be determined with the respective equations given in Section 2.3.

5.1.2. Some Practical Considerations

For the perturbation measurement a Vector Network Analyser (VNA) is used to excite the cavity under test. Measurements are possible in both reflection and transmission. The setup for the more

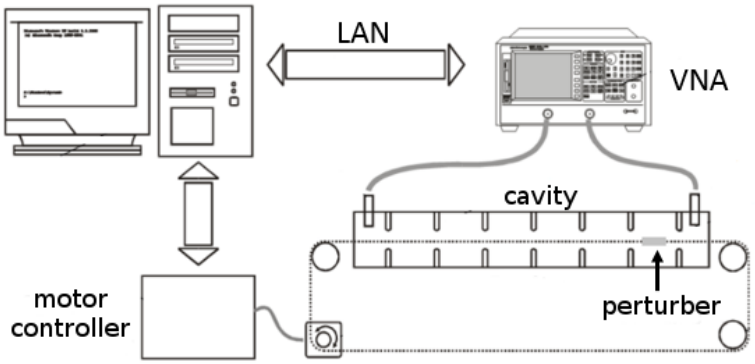

Figure 5.1.: Illustration of the setup for measuring axial fields in an EM cavity by a perturbation method.

sensitive transmission measurement is shown in Fig. 5.1. The cylindrical perturber must be pulled along the beam axis of the cavity. In case of the long SPS TWS the installation of the perturber on the axis is quite cumbersome even for a single 11-cell section. At first, common fishing line is shot through the section and the cylindrical perturber is typically obtained from an ordinary syringe cut to the appropriate length. The line is formed to a closed loop by laying it over a pulley attached to a stepping motor on one side of the cavity and a passive pulley on the other side, see Fig. 5.1. The motor is used to step the perturber through the structure and VNA and motor are controlled via a LabVIEW^{TM} program running on a separate workstation [72]. Communication between the different devices is realised via Ethernet connection. While the motor pulls the perturber through the cavity, the software constantly stores the S_{21} transmission measurement. This complex valued data must be post-processed extensively before finally Eq. (2.12) can be applied to calculate the R/Q of the resonance from the measured electric field. Measurement and post-processing have to be conducted for every cavity resonance of interest.

A trade-off is to be considered when choosing the length of the perturbing cylinder. It should be as short as possible to disturb the fields inside the cavity only slightly. After all, the field profile of the unperturbed mode shall be measured. Due to the non-linearity of the tangent in Eq. (5.5), the phase excursion $\Delta\phi$ is to be kept quite small ($\Delta\phi \lesssim 25°$) to avoid that small errors in the $\Delta\phi$ measurement result in large errors in the frequency shift. A longer perturber also means less longitudinal resolution as at every position the electric field is integrated over the whole length and results in a single measurement sample. On the other hand, the perturber length has to be long enough to achieve a sufficient so-called phase excursion. The change in phase of S_{21} must be large enough to be detected by the VNA and to not be completely superimposed by the measurement noise. The perturber length is also dependent on the Q_l and ω_0 of the cavity resonance, cf. Eq. (5.5).

Another trade-off lies in the coupling strength of the measurement antennas to the cavity resonance. The coupling should be quite weak as after all the electric field unperturbed by the antennas shall be measured, but not too weak so that the measurement trace is impaired by noise. Often, a few slight changes in antenna positions are necessary to achieve an acceptable compromise. The

perturbation method is foremost applied to high-Q resonances. For the above mentioned reasons, measurement of heavily damped modes, achieved e.g. by the deployment of HOM couplers, is difficult.

5.2. Verification of Simulation Models and Evaluation of the Three Available 11-Cell Spare Sections

Three spare sections of the SPS 200 MHz structure are available which were not in use before LS 2. Two of these will be required for the post LS 2 configuration in which two 5-section structures will be rearranged to four 3-sections. RF measurements were conducted on the three spares as a benchmark of the simulation models used throughout this thesis and to verify their validity. The results have also been used to select two of the three spare sections to be used post LS 2.

For lab measurements, a section is usually excited by electric probes placed on the longitudinal axis at both end-plates as this allows to excite all longitudinal modes of interest, see also Eq. (3.6). The protrusion of the measurement probes into the cavity is adjusted such that weak coupling to the resonances is ensured. The transmission measurement S_{21} in the FPB of the three former spares shows the 11 cavity resonances, see Fig. 5.2. The resonances of spares 1 and 2 coincide well,

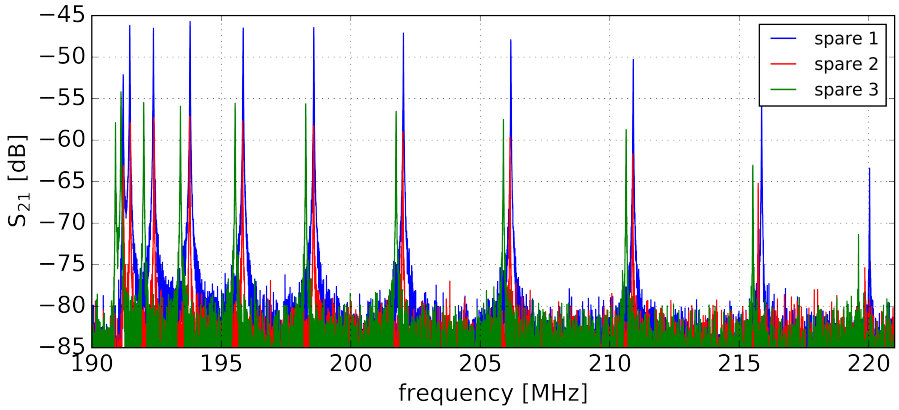

Figure 5.2.: On-axis transmission measurement S_{21} in the frequency range of the FPB of the three 11-cell spare sections.

whereas a significant frequency shift can be observed in spare 3 [1]. It is easy to associate the measured resonances with their appropriate wavenumber or phase advance per cell respectively. The dispersion curve for the three spares is then interpolated over the frequency range of the FPB using a cubic spline interpolation, see Fig. 5.3. It is planned to also measure the resonant frequencies in the TM_{01} passbands once the sections become available for measurements again, so that instead

[1] In fact, from the way spare 3 was stored it seems unlikely that it was ever used in the SPS.

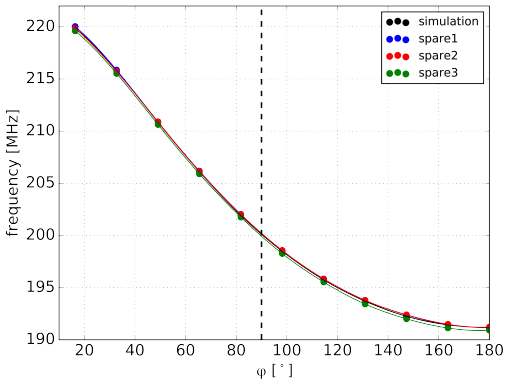

Figure 5.3.: Dispersion curves of the three spare sections interpolated from the measurement of their 11 resonant frequencies in the fundamental TS_{11} passband.

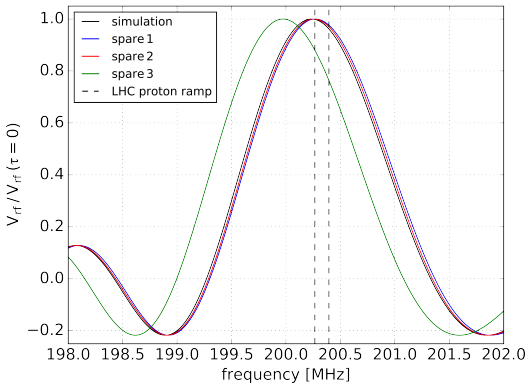

Figure 5.4.: Transit time factors (TTFs) of the three spare sections obtained from their dispersion curves in Fig. 5.3 and Eqs. (2.20) and (2.21).

Eq. (3.7) can be used as an interpolation function for the FPB. With Eqs. (2.20) and (2.21) we obtain the TTFs of the three spare sections shown in Fig. 5.4. Eq. (3.11) was used to obtain the frequency dependence of the structures under vacuum so that it is immediately possible to read the tuning of each section from the peak of its TTF. All sections are expected to be fixed-tuned close to 200.222 MHz, cf. Section 3.5, and spares 1 to 3 deliver peak voltage at 200.270, 200.254 and 199.974 MHz respectively. The frequency range required for the acceleration of the LHC proton beam from injection to top energy in the SPS is also shown in Fig. 5.4, dashed lines. The beam is injected at an energy of 24 GeV and an RF frequency of 200.265 MHz, cf. Eq. (3.1). The harmonic number is 4620. The beam is then accelerated and extracted to the LHC at 450 GeV corresponding to an RF frequency of 200.394 MHz. It is quite obvious from Fig. 5.4 that the TWSs are tuned slightly too low for today's LHC beam. Especially at extraction the structures are operated below their peak impedance. Spare 3 should undergo a tuning procedure to become a valid spare for the HL-LHC era. The simulation of an 11-cell tank configuration with stem lengths of 321 mm shows peak voltage at 200.235 MHz and is in good agreement with spares 1 and 2.

The geometry factors of the three spare sections were measured with the perturbation technique introduced in Section 5.1. By observation of Eq. (5.2) it is clear that the sign of the electric field in the individual cells can not be measured unambiguously. Comparing to the simulated electric field profile of the respective mode can therefore often be of great help to correctly reconstruct the sign of the field. As an example of a perturbation measurement, the simulated and measured longitudinal, on axis electric field E_z of the TS_{11} $5\pi/11$ resonance in the fundamental passband of an 11-cell section is compared in Fig. 5.5. The overall agreement between simulation and measurement is excellent, with the measured field strength being slightly larger along the whole length of the structure. The positions of the drift tubes in which the perturber is shielded from the EM fields are easily recognised by the noise on the measured electric field.

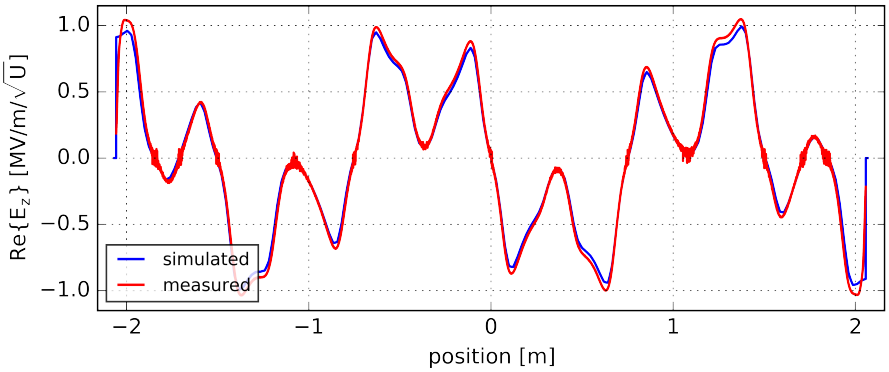

Figure 5.5.: Simulated and measured longitudinal, on axis electric field E_z of the TS_{11} $^{5\pi}/_{11}$ resonance in the FPB of an 11-cell section. Both, simulation and measurement are normalised to the respective stored energy U.

The measured geometry factors for spare 2 are compared to values obtained from eigenmode simulations in Fig. 5.6. More detailed results for all three spare sections are reported in **[44]**. Three measurement traces were taken for each resonance and the data points shown in Fig. 5.6 are the average of these three runs. The error bars presented in **[44]** are based on these three samples only. The overall agreement between simulation and measurement is good. Careful study of the data however shows a systematic error. The measured geometry factors are around 15 % larger than the corresponding simulated values and this error is independent of frequency. The discrepancy can be explained by an incorrect form factor G_{cyl} used in the data post-processing and also gives a good impression of the sensitivity to the size of the perturber. Eq. (5.4) is the form factor for a metallic cylinder, however in practice the cylinder is threaded onto the fishing line and fixed by small amounts of glue at both ends. It is conceivable that the charge distribution on the cylinder is modified and its polarisability slightly altered so that is does not correspond exactly to Eq. (5.4). The physical length of the cylinder was 15 mm for the measurements reported in Fig. 5.6 and **[44]**. If the length is increased by only 0.7 mm in the post-processing, e.g. an $^{R}/_{Q}$ of 50 Ω is obtained for the $^{5\pi}/_{11}$-mode. The measured and simulated electric field profiles shown in Fig. 5.5 for a cylinder length of 15 mm are then quasi-identical. With the adapted form factor G_{cyl}, simulated and measured geometry factors are in very good agreement across the frequency range shown in Fig. 5.6.

The simulated unloaded quality factors in the FPB of an 11-cell section are compared to the measured quality factors of spare 2 in Fig. 5.7. Each TS_{11} cavity resonance was measured separately in transmission S_{21} and extremely weak coupling was ensured on the Smith chart. The transmission was below -70 dB in all cases so that the measured quality factors can be considered unloaded. The distribution of the quality factors in the frequency range of the FPB shows increasing RF losses in going from the $^{\pi}/_{11}$- to the π-mode. These losses are mainly caused by the stem currents and with increasing phase advance per cell a larger number of stems is subject to strong currents. Refer also to Eq. (3.5) in this regard.

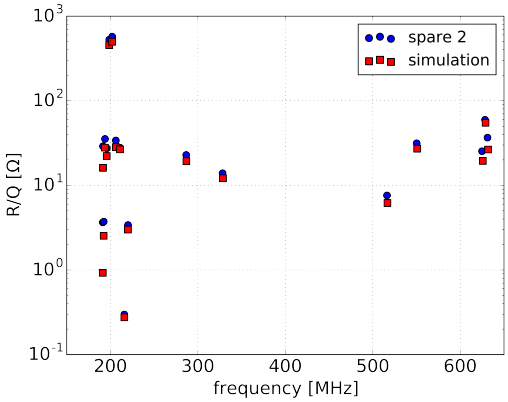

Figure 5.6.: Comparison of measured and simulated geometry factors R/Q of select longitudinal modes in an 11-cell resonant section.

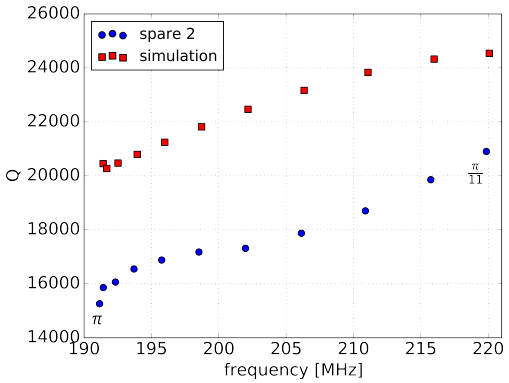

Figure 5.7.: Comparison of measured and simulated (unloaded) quality factors Q in the FPB of an 11-cell section. Very weak coupling to the resonances was ensured throughout the measurements.

The measured quality factors are lower than the simulated values obtained with a copper conductivity of $5.8{\cdot}10^7\ S/m$. There are numerous possible reasons for this discrepancy. The spare sections were exposed to the atmosphere for extended periods of time and oxidation or other deteriorations of the inner copper layer can lower the quality factors. Before installation in the SPS tunnel, the cavities will undergo a surface treatment that removes such defects. Other possible reasons are leakage via the grids in the VPPs or additional losses in the HOM access ports which are not modelled in order to keep the mesh size at acceptable levels. The situation is similar for undamped HOMs, however, most notably for heavily damped TS_{31} modes in the 630 MHz frequency range, simulated and measured loaded quality factors are very close (not explicitly shown here).

5.3. Verification of 25 Ω-Equivalent Complex Impedance Loads

The theoretical analysis and the simulations in Section 4.3 suggest optimum HOM mitigation of the $5\pi/11$ and $14\pi/33$ high-R/Q TS_{31}-modes by 35 Ω and 25 Ω HOM coupler impedances respectively. These impedances could be realised by changing the characteristic impedance of the coaxial coupler, which would lead to a modification of the inner conductor since the outer pipe diameter is constrained due to the size of the access ports. This would require a design change of the existing HOM coupler and fabrication of a large number of coupler parts which comes at high costs. An alternative approach was therefore developed in this thesis. The desired impedances can also be realised by loads with complex impedance connected to the output ports of the couplers. Provided these are designed correctly, such complex loads are then transformed by the 50 Ω transmission line of the existing HOM coupler to the desired impedance at the base of the electric pickup. Like

so, the couplers can effectively present a 35 or 25 Ω impedance to the HOMs around 630 MHz. For this type of implementation the existing HOM couplers do not need to be modified and in comparison the procurement of complex loads is fairly economical.

The improved damping of the TS_{31}-HOMs with the 25 Ω-equivalent complex loads suggested by the simulations in Fig. 4.17 shall be verified by RF measurements. This requires knowledge of the electrical length of the 50 Ω coaxial line in the HOM coupler around 630 MHz. For this purpose, reflection measurements were performed on the load port of the coupler with the electric pickup detached as shown in Fig. 5.8. At 628 MHz the measured reflection in the 'open' configuration

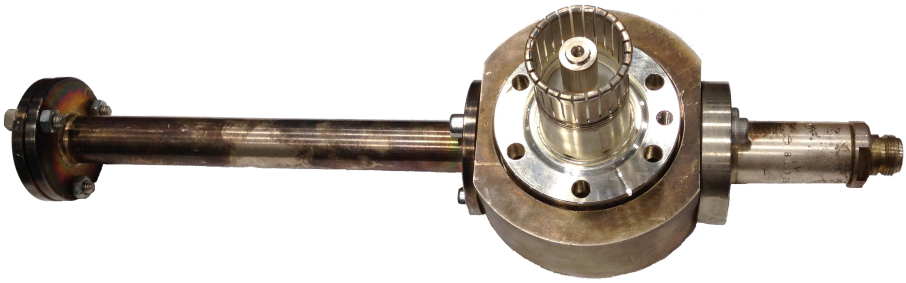

Figure 5.8.: The 630 MHz HOM coupler without the electric pickup. The electrical length of the 50 Ω transmission line from the N-standard connector on the right to the mounting point of the pickup at the top is measured in the open configuration shown and for verification also with a short in the plane of the mounting point. The coaxial air line contains different dielectrics like e.g. the ceramic RF window.

is 0.9965∠36.3°. To test consistency, one can also measure the 'shorted' configuration in which the transmission line is electrically shorted in the plane of the mounting point of the pickup. The reflection then is 0.9958∠-143.5°. The two reflections are also recorded in the Smith chart [73] of Fig. 5.9 for illustration (■ and ▲ respectively). The reflection coefficient Γ(0) at the end of a transmission line of length l is transformed to its input according to

$$\Gamma(l) = \Gamma(0)\, e^{-2\gamma l} \tag{5.6}$$

with the propagation constant γ. The electrical length of the transmission line in the HOM coupler is hereby determined to 162° at 628 MHz. Its mechanical length is slightly shorter with roughly 19.5 cm due to the dielectrics like e.g. the ceramic RF window.

The desired impedance that is to be presented to the HOMs must now simply be transformed via the coupler line to determine the appropriate impedance of the complex loads. This is illustrated for the case of the 25 Ω-equivalent impedance in Fig. 5.9. The start of the transmission line is at the base of the electric pickup and the desired input impedance is (25+j0)Ω. This impedance is transformed in the direction of the load following Eq. (5.6) in the lossless case. The input im-

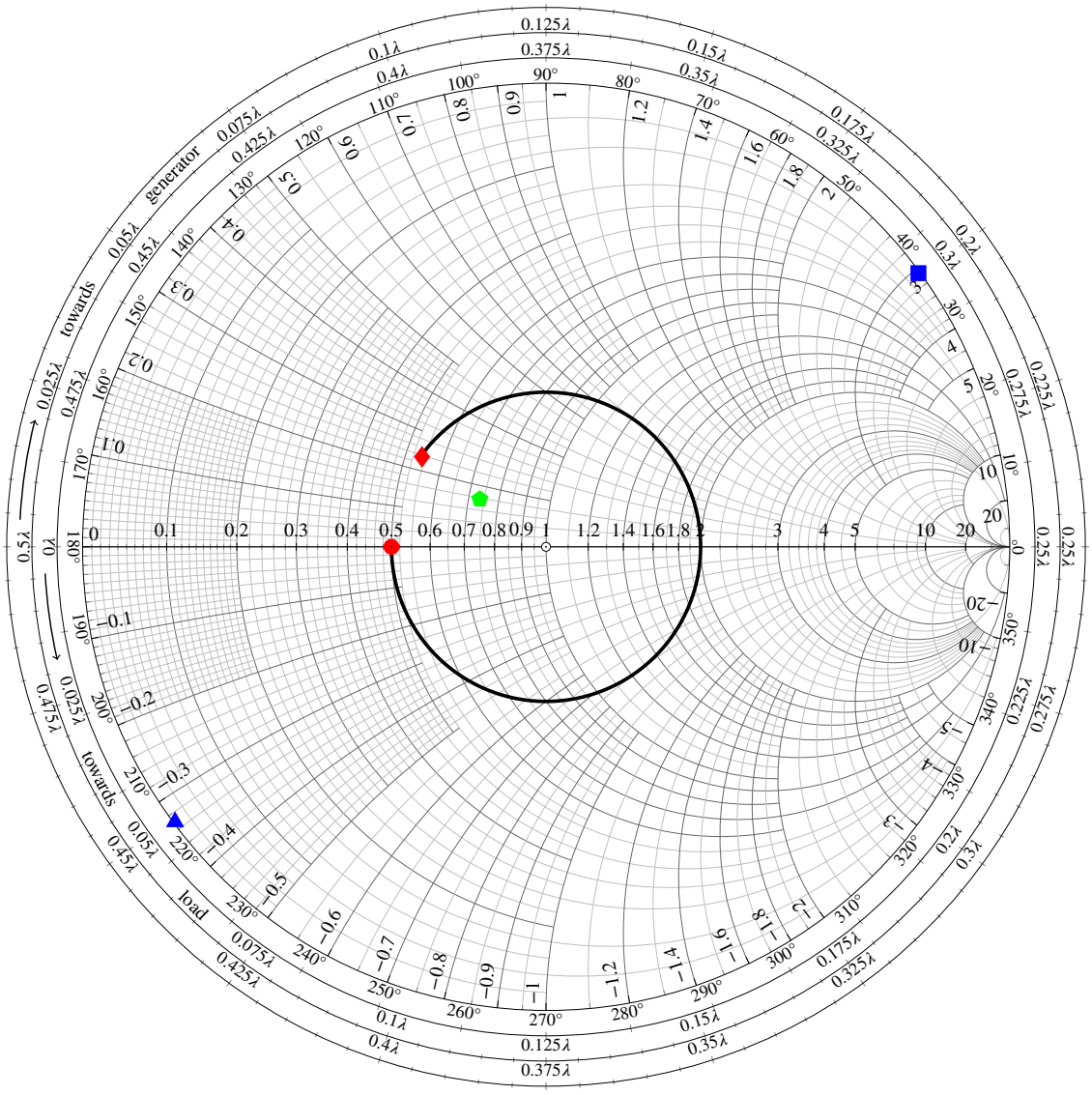

Figure 5.9.: Smith chart [73] illustrating the development of complex loads for the TS_{31} HOM coupler. The chart is normalised to the 50 Ω characteristic impedance of the coupler and all entries are at the frequency of 628 MHz. The electrical length of the coupler transmission line is measured in reflection for an open (■) and a shorted (▲) configuration. The complex load impedance at ⧫ is required to obtain the desired 25 Ω (●) at the base of the electric pickup of the HOM coupler.

pedance or corresponding reflection coefficient of 25 Ω-equivalent complex loads (♦ in Fig. 5.9) must be

$$\begin{aligned} \underline{Z}_{25\,\Omega} &= (26.9 + j11.8)\,\Omega \\ \underline{\Gamma}_{25\,\Omega} &= 0.333\angle 144.3^\circ\,. \end{aligned} \tag{5.7}$$

For a 35 Ω-equivalent complex load (⬟ in Fig. 5.9)

$$\begin{aligned} \underline{Z}_{35\,\Omega} &= (36.7 + j7.8)\,\Omega \\ \underline{\Gamma}_{35\,\Omega} &= 0.176\angle 144.3^\circ \end{aligned} \tag{5.8}$$

is required.

The improved HOM damping across the 630 MHz frequency range with complex loads is demonstrated on an 11-cell section equipped with the longitudinal, pre-LS 2 damping scheme illustrated in Fig. 5.10. The complex load impedances of Eqs. (5.7) and (5.8) were realised with

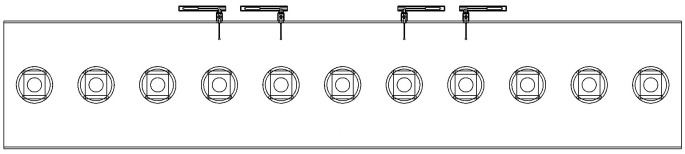

Figure 5.10.: Cavity configuration used for the verification of complex loads. Transmission measurements are performed for four cases of load impedances on the HOM couplers: no loads, the 50 Ω standard as well as 35 Ω- and 25 Ω-equivalent complex loads. Only the two couplers in cells four and eight contribute to damping of the TS_{31} $5\pi/11$-mode, cf. Fig. 4.3.

adjustable triple stub tuners for these measurements. A more practical implementation of the 25 Ω-equivalent complex load for large scale deployment in the SPS would e.g. be a 25 Ω resistive load in series with a coaxial line of 18° (+ n·360°, n=0,1,2,…) electrical length.

Figure 5.11a shows the on-axis transmission for the different HOM coupler loads **[74]**. For this type of excitation, a measurement of the loaded quality factor Q_l of the $5\pi/11$-HOM at ≈627 MHz is not possible for any of the three loads. The installation of 35 and 25 Ω-equivalent complex loads results however in reduced transmission over the whole frequency range compared to the 50 Ω standard loads, indicating overall increased mode damping. The $5\pi/11$-mode shows strong field in cells six and ten of an 11-cell section, cf. Fig. 4.3. The cavity was therefore excited via electric probes installed in the HOM-ports on top of these cells to measure the quality factor of the $5\pi/11$-mode for the different loads. The transmission S_{21} for this excitation is shown in Fig. 5.11b and the $5\pi/11$ resonance is now visible at ≈627 MHz. The position and coupling of the excitation probes was left untouched during all measurements. The results of the Q_l measurements are shown in Table 5.1. The best damping is achieved with a coupler impedance of around 35 Ω for the $5\pi/11$-mode as suggested by the simulation results reported in Fig. 4.17. Compared to the 50 Ω standard load the Q_l is reduced by 27 %. Additional mitigation might be expected due to a reduction in R/Q, however, as was already explained in Section 5.1.2, measurement of R/Q with a perturbation method of heavily damped modes is difficult. The pre-LS 2 damping scheme used here on a single

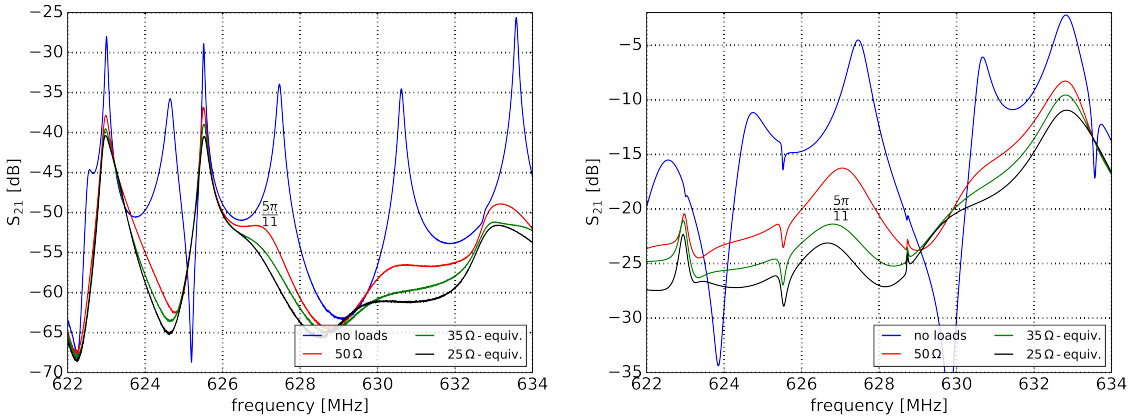

(a) On-axis excitation via electric probes at both ends of the structure.

(b) Excitation via electric probes in the HOM-ports on cells six and ten that feature strong electric field of the $^{5\pi}/_{11}$-mode, cf. Fig. 4.3.

Figure 5.11.: Measured transmission S_{21} for different HOM coupler loads in the cavity setup of Fig. 5.10. Adjustable triple stub tuners implementing the impedances of Eqs. (5.7) and (5.8) result in 35 and 25 Ω equivalent coupler input impedances at the base of the HOM coupler pickups.

section is not optimal for damping the $^{5\pi}/_{11}$-mode and the HOM couplers in cells five and seven are ineffective on this mode, cf. Fig. 4.3. Even larger improvement due to the complex loads can therefore be expected on an optimised damping scheme, like e.g. the one proposed for the 33-cell structure in Section 4.3.

Simulations suggest that the HOM with the largest impedance in 33-cells has a $^{14\pi}/_{33}$ phase advance and the optimal HOM coupler impedance for this mode is around 25 Ω, cf. Fig. 4.17a. The $^{14\pi}/_{33}$-mode does not exist on an 11-cell section due to the boundary conditions and could therefore not be measured, but agreement between simulation and measurement for the $^{5\pi}/_{11}$-mode is excellent and is considered sufficient for a proof-of-principle. These measurements give confidence in the simulation results obtained for a 33-cell structure. A 25 Ω-equivalent load is not optimal for the

Table 5.1.: Measurement of the loaded quality factor Q_l of the TS_{31} $^{5\pi}/_{11}$-mode for different HOM coupler loads in the cavity setup of Fig. 5.10. The improved damping for the 35 and 25 Ω-equivalent loads is given with respect to the 50 Ω standard load. Note that the damping scheme is not optimal for the mitigation of the $^{5\pi}/_{11}$-mode and the improvements are likely to be larger for the optimised damping scheme on the 33-cell structure.

	f [MHz]	Q_l	$\Delta Q_{50\,\Omega}$ [%]
50 Ω	626.98	397	-
35 Ω-equiv.	626.78	290	27
25 Ω-equiv.	626.70	329	17

$5\pi/11$-mode, but still results in a considerable damping improvement compared to the 50 Ω load. The use of 25 Ω-equivalent loads on all 630 MHz HOM couplers in the SPS tunnel has therefore been suggested to the LIU management to maximise mitigation of the $14\pi/33$-mode that has largest impedance, but keep the complex load implementation and the new damping scheme relatively straightforward at the same time.

5.4. Verification of Resonant Posts

The main purpose of the resonant posts in the new damping scheme proposed for the 33-cells (illustrated in Fig. 4.25) is the mitigation of the two high-R/Q HOMs with $14\pi/33$ and $5\pi/11$ phase advance. The improved HOM mitigation suggested by the simulation results reported in Section 4.5 shall be demonstrated by RF measurements. A fully equipped 33-cell structure is not available, which is why the measurements were carried out on a resonant 11-cell section in the setup illustrated in Fig. 5.12. VPPs are available below cells three, six and nine of each section, cf. Fig. 3.7, but from

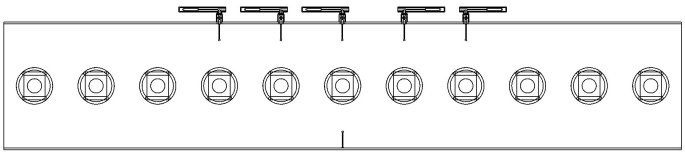

Figure 5.12.: Cavity configuration used for the verification of resonant posts by RF measurements. A resonant post is placed in the VPP of cell six in which the TS_{31} $5\pi/11$-mode features strong electric field, cf. Figs. 4.3 and 4.4.

inspection of Figs. 4.3 and 4.4 it is clear that a resonant post is effective on the $5\pi/11$ HOM only in cell six. Note that the $14\pi/33$-mode does not exist in 11-cells. It was already described in Section 4.4 that the installation of numerous HOM couplers in the upper half of the section creates a structural asymmetry such that a large portion of the resonant fields are pushed into the lower half of the structure where they are inaccessible via the top access ports. The use of resonant posts can also attenuate these effects.

The on-axis transmission between electric pickups placed at the two end-plates without and with the resonant post in cell six is shown in Fig. 5.13. The $5\pi/11$ HOM is at the frequency of ≈ 626.5 MHz, refer back to Fig. 5.11. In the case that the resonant post is installed, the transmission around this frequency is heavily reduced, indicating a mitigation of the $5\pi/11$-mode. The mitigation is even larger than the one achieved with complex loads, compare to Fig. 5.11a. Other resonances visible in this frequency range are impacted less as their electric field is comparatively weak at the position of the post in cell six. Slightly larger transmission can be observed around 633 MHz. This is in very good agreement with the impedance simulations of Figs. 4.26 and 4.27 as well which show slightly increased impedance below and above the resonant frequency of the post. In the measurements of Fig. 5.13, larger transmission can not be observed at lower frequencies, however no statement can be made on the $16\pi/33$-mode indicated in Fig. 4.26 as it does not exist in an 11-cell

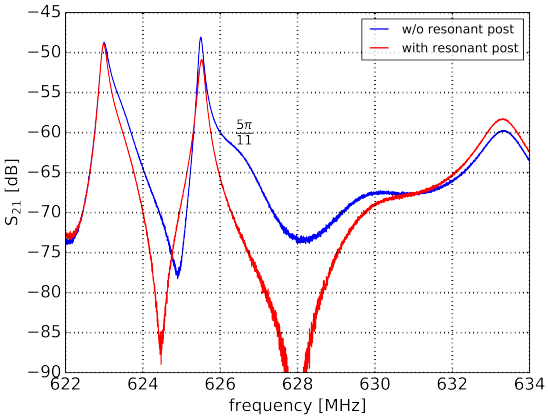

Figure 5.13.: Measured transmission S_{21} in an 11-cell section with the HOM coupler configuration illustrated in Fig. 5.12 and without and with the resonant post in the bottom of cell six.

section. Overall, a clear mitigation of the high-R/Q mode is demonstrated and agreement with EM simulations is given. The performance of the resonant posts on the 33-cell structure as suggested by simulations is therefore considered trustworthy.

5.5. Measurement of Transit Time Factor of Travelling Wave Structures

The installation of HOM mitigation devices in the TWSs leads to an unavoidable influence on the fundamental accelerating mode. It is unknown if detailed investigations of this parasitic impact were ever conducted, e.g. in terms of a loss in the accelerating voltage delivered by the TWSs equipped with the HOM damping scheme deployed so far. In comparison, the newly proposed, improved HOM damping scheme uses an even higher number of HOM mitigation devices. During its development phase, the decision was therefore taken to properly quantify and assess the impact on the accelerating voltage. One such influence is a detuning of the TWSs which were originally tuned without the presence of any HOM couplers, cf. Section 3.5. The frequency dependence of the RF voltage is entirely contained in the transit time factor (TTF) and eventually in the phase slip τ of the TWS, cf. Eqs. (2.20) and (2.21). The $\sin(x)/x$-behaviour of the TTF and thereby also the tuning of the TWS could in theory be reconstructed by sampling the frequency range of its fundamental passband with non-resonant perturbation measurements of the accelerating voltage (bead pull method). Application to the 200 MHz acceleration system in the SPS is however infeasible due to the extreme mechanical length of the TWSs with up to 21 m. Therefore, an alternative method was conceived. As will be shown in the following, the TTF can also be obtained from measurement samples in each accelerating gap. Opposed to perturbation techniques, the RF voltage can however certainly not be measured in absolute terms as in practice measurement probes must be positioned off-axis.

5.5.1. Theory

We start our analysis similar to Section 3.6.1 by describing the travelling wave injected by the generator with

$$E^{+}(z,t) = E_0\, e^{-jkz}\, e^{j\omega t}\,,$$

for once also explicitly writing the time harmonic dependence. We can measure this travelling wave at N off-axis sampling points in the gap centres at $z = np$, i.e. via the lateral ports on each section of the SPS structure, see Fig. 3.7. Like this, we obtain field strength readings proportional to the on-axis values in the respective gaps. The situation is illustrated in the schematic of Fig. 5.14. In

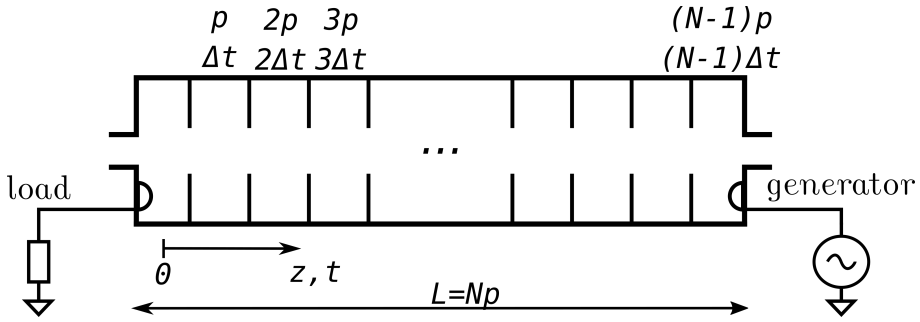

Figure 5.14.: Schematic view of a TWS providing access ports for RF measurements in each accelerating gap at the positions $z = np$, $n = 0, 1, ...N - 1$. The beam passes the centre of each gap at $t = n\Delta t$.

passing through all gaps, the beam experiences merely time-shifted versions of our measurement samples and so we write the measured voltage $V_{rf,m}$ as

$$V_{rf,m} \propto \sum_{n=0}^{N-1} E_0\, p\, e^{-jknp}\, e^{j\omega n\Delta t}\,. \tag{5.9}$$

Here we assumed a constant electric field across each gap and $\Delta t = {}^{p}/_{v_p}$ is the time it takes the beam to pass from one gap to the next. We use a linear expansion around the synchronous point (ω_0, k_0) of the dispersion curve

$$\begin{aligned} \omega &= \omega_0 + \Delta\omega \\ k &= k_0 + \frac{dk}{d\omega}\Delta\omega = k_0 + \frac{\Delta\omega}{v_g} \end{aligned}$$

to express the exponent in Eq. (5.9) via the phase slip τ defined in Eq. (2.20). The time shift for the backward $\pi/2$-mode at synchronism is $\Delta t = \pi/2\omega_0$. We reformulate the exponent in Eq. (5.9) to

$$\begin{aligned} knp - \omega n\frac{\pi/2}{\omega_0} &= n\left(\frac{\Delta\omega}{v_g}p - \frac{\pi}{2}\frac{\Delta\omega}{\omega_0}\right) \\ &= \frac{np}{v_g}\Delta\omega\left(1 - \frac{\pi/2}{p}\frac{v_g}{\omega_0}\right) \\ &=: \frac{n\tau}{N}\,. \end{aligned}$$

The geometric series becomes

$$V_{rf,m} \propto E_0\, p \sum_{n=0}^{N-1} e^{-j\frac{n\tau}{N}} = E_0\, p\, \frac{1 - e^{-j\tau}}{1 - e^{-j\frac{\tau}{N}}}\,. \tag{5.10}$$

We now separate modulus and phase and obtain for what we measure

$$V_{rf,m} \propto E_0\, L\, e^{j\Phi}\, \frac{\sin(\tau/2)}{N\sin(\tau/2N)}\,. \tag{5.11}$$

When comparing to the RF voltage

$$V_{rf} = E_0\, e^{j\Phi}\, L\, \underbrace{\frac{\sin(\tau/2)}{\tau/2}}_{\text{TTF}} \qquad \text{(Eq. (2.21) revisited)}$$

actually seen by the beam, we notice that the TTF differs only in the denominator. The difference will become significant for $\tau/2N > \pi/4$, so for $\tau > N\pi/2$. This is merely the case for very large $\Delta\omega$, e.g. $\tau(\Delta\omega{=}1\,\text{MHz}) = 0.53\,\text{rad}$ only. The error manifests itself in amplitude. We can therefore measure the TTF of a TWS by summing time shifted measurement samples taken in its accelerating gaps. The synchronous frequency to which the TWS is tuned is easily obtained via the peak of the TTF. It should be mentioned that an RF feedback system implementing the summation of cell signals similar to Eq. (5.9) was first proposed in [75] for compensation of beam loading.

5.5.2. Application to the TWSs in Use Until Long Shutdown 2 in the SPS

The previously described measurement method is now applied to the four TWSs that were used in the SPS until LS 2. The setup for the measurement of the TTF is illustrated in Fig. 5.15. A VNA is used to inject a travelling wave while sweeping the frequency range of the FPB. The coaxial feeder lines connecting the RF generators to the input matching network are replaced by adaptors to the type N connector standard. The two input ports of the structure are driven simultaneously via a 3 dB combiner. The travelling wave is probed with the second port of the VNA in each gap of the structure via the lateral access ports. Modulus and phase of the transmission S_{21} across the frequency range of the FPB are recorded in each cell for data post-processing later on.

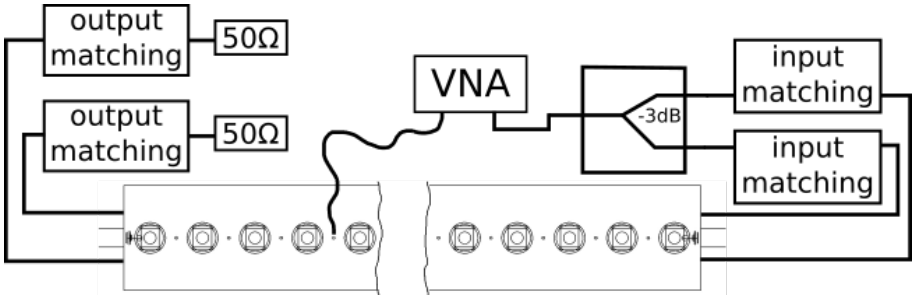

Figure 5.15.: Setup for measurement of the RF voltage in the SPS TWS. One port of the VNA is used to inject a travelling wave and the second port to probe the wave in each gap. The coaxial lines in front of the input matching network are equipped with adaptors to the type N connector standard. A 3 dB combiner is used to simultaneously drive the two input ports of the structure.

Most precise results would be obtained by using the same measurement probe in each lateral port or a set of previously calibrated probes. Even probes of the same type might differ slightly in their RF characteristic, i.e. falsifying the phase advance per cell of the travelling wave measured in consecutive cells. For economical reasons[2] the lateral loop couplers already in place on the TWSs are used. Prior to this, the transmission to a small number of lateral loops was measured in the same cell. This showed a phase difference within less than a degree so that the precision of measurements with non-calibrated pickups should be appreciable.

The measurement data is time-shifted and summed according to Eq. (5.9). The results for the four SPS TWSs that were in operation until LS 2 and of which two consist of four and two of five 11-cell sections are shown in Fig. 5.16. The $|{}^{\sin x}/_{x}|$ characteristic of the TTF is easily recognised as well as the smaller bandwidth of the longer 55-cell structures. The structures were measured under atmospheric pressure, but Eq. (3.11) was used to calculate the frequency dependence under vacuum. The TWSs were originally fixed-tuned to 200.222 MHz, cf. Section 3.5 and [27]. However, from the measurements we observe the peak impedance of all four structures at significantly lower frequencies. A possible explanation for this detuning are the numerous HOM couplers of the longitudinal and transverse damping schemes added after the original tuning to 200.222 MHz. This is further supported by the fact that a significant difference in synchronous frequencies of TWSs 1 and 2 of 26 kHz is measured that could be attributed to the TWS 1 being equipped with two additional transverse HOM couplers compared to TWS 2. TWSs 3 and 4 are equipped with identical numbers and types of HOM couplers and show peak impedance at almost identical frequencies (3 kHz apart). The impact of the HOM couplers on the frequency dependence of the accelerating voltage is investigated in further detail in the following section. The amplitude difference visible in Fig. 5.16a is most likely due to lateral loops with slightly different RF characteristics installed on the TWSs. The field magnitudes measured in all gaps show the characteristic π-pattern due to the slight mismatch of the structures [76], which was predicted by the theory in Section 3.6.1 and also already observed in simulations, see Fig. 3.23a.

[2]Demounting of the lateral pickups would later on require a costly replacement of their vacuum gaskets.

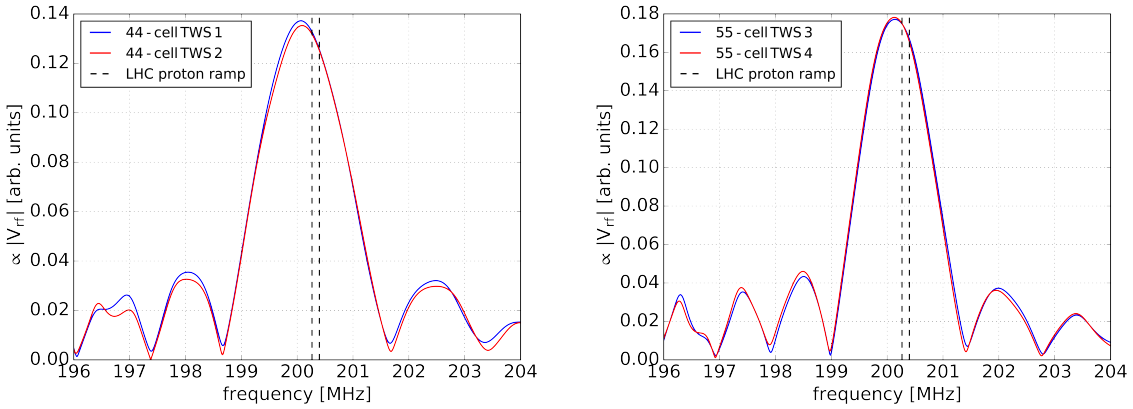

(a) 44-cell TWSs.

(b) 55-cell TWSs.

Figure 5.16.: Measurement of frequency dependence of the RF voltage in the four SPS TWSs in operation until LS 2 with the longitudinal and transverse HOM couplers in place. The frequency dependence shown is for evacuated structures and was derived from the one under atmospheric pressure using Eq. (3.11). The synchronous frequencies of the TWSs 1 to 4 are 200.063 MHz, 200.089 MHz, 200.136 MHz and 200.133 MHz respectively. The dashed, vertical lines highlight the frequency range required for ramping the LHC proton beam in the SPS.

5.6. Impact of HOM Couplers and Resonant Posts on the Accelerating Passband

Impairment of the fundamental accelerating mode by HOM couplers inserted into a TWS is conceivable in many ways of which the following three are considered here. The couplers can introduce a detuning as well as a mismatch to the RF generator and terminating load. An unwanted damping of the FPB is possible as well in case that coupling occurs also to the accelerating mode. It is envisaged to perform the matching procedure for the post-LS 2 TWSs with the new HOM damping schemes in place so that no deterioration is to be expected in this regard. In the following, we first study the detuning and later on the possible damping of the accelerating mode.

Eight HOM couplers were added on the 4-section TWS 2 to allow a detailed study of the detuning by measurements. Figure 5.17 compares the TTF of this structure before and after the addition of the eight couplers and suggests a detuning to lower frequencies by 85 kHz. This is to be expected since the couplers are placed in regions with strong electric field of the fundamental mode. Recall that the TWSs are fixed-tuned to the frequency of 200.222 MHz which is below the frequency range of the ramp of the LHC proton beam in the SPS. The situation is further aggravated by the numerous HOM couplers placed on the structures in the existing and especially also the future, improved mitigation schemes. Figure 5.18 shows the additional loss in RF voltage which is provided by the 4-section TWS 2 in the frequency range required for the ramp of the LHC proton beam due to a further detuning by -85 kHz. The loss in RF voltage amounts to roughly 2.5%

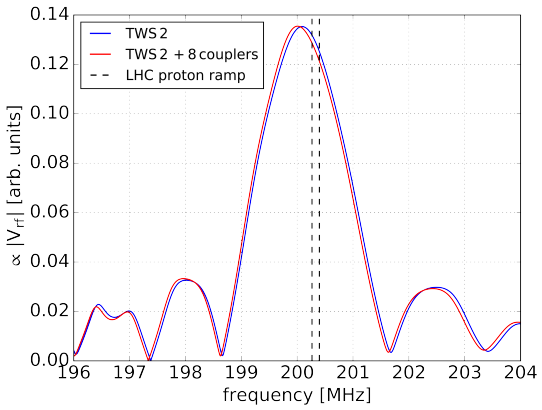

Figure 5.17.: Measurement of frequency dependence of the RF voltage in the SPS 44-cell TWS 2 with and without eight additional HOM couplers. The frequency dependence shown is for evacuated structures and was derived from the one under atmospheric pressure using Eq. (3.11). The synchronous frequency is shifted due to the additional HOM couplers by -85 kHz to 200.004 MHz. The dashed, vertical lines highlight the frequency range required for ramping the LHC proton beam in the SPS.

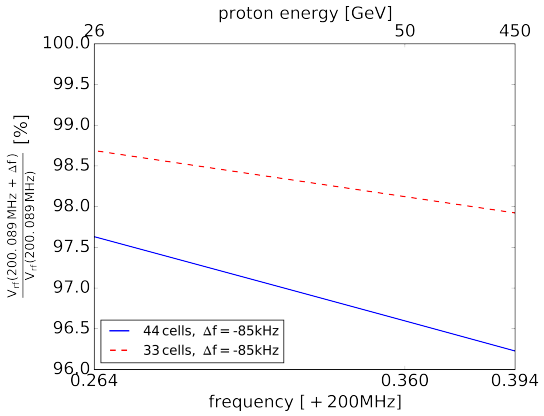

Figure 5.18.: RF voltage drop ΔV_{rf} in 44- and 33-cell TWSs detuned by -85 kHz with respect to structures tuned to 200.089 MHz in the frequency range required for the ramp of the LHC proton beam from 26 GeV to 450 GeV in the SPS.

at injection and 3.5% after acceleration to 450 GeV. This figure does not show the amount of RF voltage which is already lost due to the existing HOM damping scheme nor due to the fact that the structures are intrinsically tuned below the frequency range of the ramp.

The $\pi/2$-mode in the centre of the FPB has a large group velocity. A perturbation of the phase advance over individual cells that are equipped with HOM couplers can therefore not be observed [76]. The frequency of the $\pi/2$-mode rather shifts by the same amount in all cells, also in those not equipped with HOM couplers. The shape of the dispersion curve around the $\pi/2$-mode is therefore not altered by the presence of the HOM couplers and is merely shifted to lower frequencies.

The three spare sections evaluated in Section 5.2 were grouped into a 33-cell structure to measure the detuning for this configuration. The simultaneous complex conjugate matching (SCM) procedure of Section 3.6.2 was implemented via adjustable coaxial lines ('trombones') to ensure a proper travelling wave fundamental mode in this setup. The measurement results should however be taken with care as spare section 3 is severely detuned, cf. Fig. 5.4. In addition, measurement of the phase advance per cell confirmed that reused stem-assemblies hosting the FPCs in the two end-cells were detuned as well. Due to delays in the production of the 630 MHz HOM couplers, the

33-cells could not be fully equipped with the newly proposed damping scheme yet. From the impact on the TTF of the 33-cell test setup, the frequency shift due to the six additional 630 MHz couplers of the newly proposed damping scheme is estimated to -40 kHz and due to the three resonant posts to -40 kHz as well [76]. The frequency shift of a resonant post is about twice as large as that of a 630 MHz HOM coupler. The more broadband 33-cell structures are less susceptible to detuning compared to 44-cells as is illustrated in Fig. 5.18. The additional loss in RF voltage that has to be expected due to the proposed damping scheme is around 2% at the extraction frequency when the 33-cell structure is assumed to be tuned to 200.089 MHz beforehand. The improved stability of the LHC proton beam obtained from the increased HOM damping outweighs however the effects of the reduced accelerating voltage, cf. [77]. Note that overall the 33-cell structures are expected to be tuned 420 kHz below the extraction frequency in the post-LS 2 configuration, including also the HOM couplers for transverse HOMs. The loss in RF voltage is then 2.5% at the beginning and 6% at the end of the ramp with respect to the peak voltage the structure could deliver at its synchronous frequency. It is planned to measure the tuning of all, fully equipped TWSs with the method proposed in Section 5.5 before the restart of the SPS after LS 2. Retuning of the TWSs to higher frequencies, e.g. the extraction frequency, by shortening all stem lengths is infeasible due to the large and complicated workload. In case a retuning becomes desirable, the protrusion of metal pins through all pedestals into the area with strong magnetic field around the stems might be feasible.

The 630 MHz HOM coupler also picks up the TS_{11} fundamental mode as its field profile is similar to that of the TS_{31} HOM. The coupler is therefore equipped with a notch filter to reject the 200 MHz accelerating mode and avoid undesired damping in the FPB. To asses the residual damping of the fundamental mode, the transmission of the travelling wave to the terminating load of a number of couplers was measured. The measurement setup illustrated in Fig. 5.15 can also be used for these measurements when the receiving port of the VNA is connected to the load ports of the HOM couplers. The transmission S_{21} of the injected travelling wave to three couplers randomly selected on the 4-section TWSs 1 and 2 are reported in Fig. 5.19. The typical notch characteristic of low transmission is visible around 198 to 199 MHz in the measurements. From the samples taken, the filters seem to be tuned slightly too low. Analysis of the filter characteristics by transmission line theory shows that the heating of the filter during operation (see Fig. 4.32) and the possibly resulting expansion of the inner conductor will rather aggravate the situation. However, if we assume a worst case transmission to the loads of -50 dB, a power of 10 W is terminated in each HOM coupler which are equipped with resistive loads of a 25 W maximum power rating. Overall, the tuning of the notch filters and the residual damping of the fundamental mode by the 630 MHz HOM couplers is presently considered acceptable.

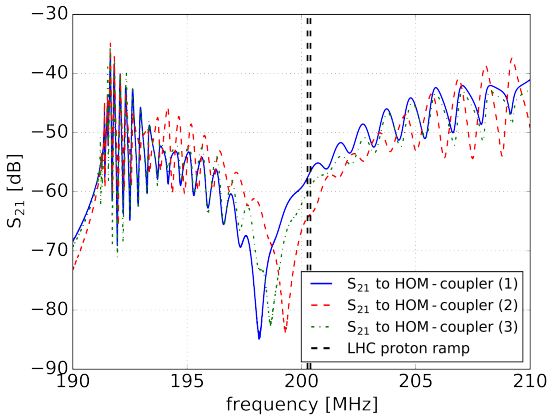

Figure 5.19.: Measured transmission S_{21} from the RF input in the measurement setup of Fig. 5.15 to the load ports of three different 630 MHz HOM couplers installed on the two 4-section TWSs.

6. Conclusions and Outlook

The main goal of this thesis was to develop an improved impedance mitigation of HOMs around 630 MHz in the SPS 200 MHz acceleration system. The source of these HOMs was identified as transverse stem resonances in the first higher order passband of the fundamental accelerating mode. The most deteriorating, high impedance HOMs were identified via their phase advance per cell and the existing damping scheme was systematically improved to target these specific modes. The theory of critical coupling between two resonators had been applied to single gap cavities in the past to achieve optimum mode damping with a resonant coupler. This thesis showed that the theory can also readily be applied to multi-cell cavities and by applying this technique a significant and practical improvement of the existing HOM coupler was proposed. The effectiveness of implementing the critical coupling via complex impedance loads was demonstrated in simulations as well as measurements and this method also significantly reduces the workload and costs for the upgrade.

The feasibility of solutions for the HOM impedance mitigation was constantly taken into account throughout the thesis. For even further improvement of the HOM mitigation, this led to the development of resonant posts, which are the most practical solution that can take both the field distribution of the HOMs as well as the available access ports on the SPS TWS into account. Due to their innovative character, the resonant posts underwent additional studies regarding possible issues like thermal heating, RF breakdown and the impact on the accelerating mode. No significant restrictions were identified that would exclude resonant posts from being deployed in the SPS acceleration system.

The development of a new HOM mitigation scheme focused on the new 33-cell configuration of the accelerating structure, but the process of step-by-step mitigation can also readily be applied to any number of cells and to multi-cell standing wave structures in general. The new HOM mitigation scheme for the 33-cell structures proposed in this thesis reduces the peak impedance around 630 MHz by a factor of 2.5 with respect to the existing damping scheme. On the 44-cell structures the peak impedance can even be reduced by a factor of 2.8 by deploying complex impedance loads on the existing damping scheme alone. Keeping in mind that the HOMs were already heavily damped before, this is a considerable improvement that will significantly increase the multi-bunch instability threshold of the SPS. The results were thoroughly verified by applying two simulation codes that use different solver methods as well as by RF measurements on an 11-cell section. Both, simulation and measurement are in good agreement. The developed technical solutions were proposed to the CERN management and at present, it is planned to equip the existing 630 MHz HOM-couplers on both the 33- and 44-cell structures with complex impedance loads for the restart of the SPS after LS 2. In the case that additional impedance reduction of the TS_{31} HOMs is later on

considered necessary in order to reach the required beam intensity for the HL-LHC, it is envisaged to install also the resonant posts.

This thesis also showed by an analytical approach that the transit time factor of a TWS can be obtained by summing time-shifted measurement samples taken in each gap of the structure. Application of this measurement method to the long TWSs of the SPS revealed that the synchronous frequencies, for which the phase slip between particles and travelling wave vanishes, are significantly lower than the expected 200.222 MHz to which the structures were originally fixed-tuned. The consequence is that the TWSs deliver significantly less than their peak RF voltage in the frequency range required for the ramp of the LHC proton beam, especially at extraction. This is a valuable input given by this thesis to particle-tracking simulations, which already resulted in better agreement between measured and simulated beam phenomena [78].

Besides the theoretical work, the measurement methods were also used to study the detuning effect of HOM couplers and resonant posts on the FPB in unprecedented detail. It was shown that the detuning of the TWSs is in fact due to the numerous installed HOM couplers and that the situation is further aggravated if additional HOM impedance mitigation shall be implemented. Preliminary measurements on a 3-section test setup determined the additional detuning that must be expected due to the newly proposed damping scheme consisting of additional HOM couplers, complex impedance loads and resonant posts. From these findings it can be concluded that the improved HOM impedance mitigation provided by the new scheme outweighs the effects of the loss in RF voltage [77]. It is also planned to measure with the method proposed in this thesis the tuning of the six TWSs that will be used after LS 2 once these are fully equipped with their new HOM mitigation schemes. The RF voltage delivered by the SPS acceleration system is then known across its full bandwidth, which is also an important contribution of this thesis to the operation of the SPS in the HL-LHC era.

In connection with this thesis, further insight could be gained regarding the matching of TWSs. The effectiveness of the non-iterative simultaneous complex conjugate matching (SCM) procedure for obtaining a proper travelling wave was successfully demonstrated in simulations as well as in a 3-section measurement setup. This not only enabled the detuning study of the HOM couplers already discussed above, but also the measurement of the phase advance per cell. The latter showed a detuning of the TS_{11} $\pi/2$-mode frequency of the stem assemblies in the end-cells of the 3-section measurement setup that are housing the fundamental coupling loops. New end-cell stem assemblies will have to be manufactured for the post-LS 2 TWS configurations and the thesis demonstrated that measuring the phase advance is a practicable tuning procedure. The two additional sections which are required for the post-LS 2 configuration of the SPS acceleration system were chosen based on measurements of the three available spare sections reported in this thesis. Most of the simulation results presented in this thesis would not have been feasible without the extensive use of the computationally efficient unit-cell approach with periodic boundaries. This required however the implementation of a lossy perfectly matched layer (PML) for the simulation of the resistive loads of HOM couplers. The implementation via the PML significantly facilitated the improvement of the HOM mitigation scheme and this technique is of interest for the design of HOM couplers in general.

A. Some Details on Travelling Wave Structures

Consider a constant impedance TWS that is used for particle acceleration only in the frequency range for which its dispersion is linear. The group velocity $v_g = {}^{d\omega}/_{dk}$ is then constant with frequency and along the structure. With the stored energy per unit length $U(z)$ and the power flow $P(z)$ follows

$$P(z) = v_g\, U(z). \tag{A.1}$$

Designating the power dissipated per unit length by ${}^{\partial P}/_{\partial z}$, the quality factor is

$$Q = \frac{\omega U}{{}^{\partial P}/_{\partial z}} \tag{A.2}$$

and the first order differential equation

$$P(z) = \frac{v_g Q}{\omega}\,\frac{\partial P}{\partial z} \tag{A.3}$$

is obtained. We make the usual ansatz to model exponential decay

$$P(z) = P_0\, e^{-\frac{z}{l_0}} \tag{A.4}$$

where P_0 is the (rms) power injected at $z = 0$ and

$$l_0 = \frac{v_g Q}{\omega} \tag{A.5}$$

is the attenuation length for which the power flow decayed to e^{-1} of its initial value.

Let the accelerating field be designated by $E(z)$, then the geometry factor per unit length is (see also Eq. (2.12))

$$\frac{R}{Q}\left[{}^{\Omega}/_{m}\right] = \frac{E^2}{\omega U} \tag{A.6}$$

from which with Eq. (A.1) the so-called series impedance

$$R_2[{}^{\Omega}/_{m^2}] = \frac{E^2}{P(z)} = \frac{\omega}{v_g}\frac{R}{Q} = \frac{R}{l_0} \tag{A.7}$$

is obtained. R is the shunt impedance per unit length. Eqs. (A.5) and (A.7) describe important parameters of a TWS and the results obtained here are given in [27, 36].

We would now like to relate the accelerating voltage to the power required to obtain this voltage in a TWS at the edges of the usable frequency band $\pm\Delta f/2$. At these frequencies the particles acquire a phase slip $\pm\tau$ along the length of the structure L in relation to the accelerating wave, see Section 2.4 and [36]. The group velocity can be expressed for this purpose by

$$v_g = \frac{d\omega}{dk} = 2\pi \frac{\Delta f}{2} \frac{L}{\tau}. \tag{A.8}$$

The peak accelerating voltage is seen by a particle that enters the structure at such a phase so that it is at the crest of the wave in the middle of the structure

$$V = E\,L\,\frac{\sin(\tau/2)}{\tau/2}, \tag{A.9}$$

see Eq. (2.21). The expression we are looking for can then be derived by squaring Eq. (A.9) and substituting with Eqs. (A.7) and (A.8) to

$$\frac{V^2}{P} = 8\,\frac{R}{Q}\frac{f}{\Delta f}\frac{(\sin(\tau/2))^2}{\tau}\,L. \tag{A.10}$$

This shunt impedance has its maximum at

$$\tau_{opt} = 2.34\,\text{rad} = 134° \tag{A.11}$$

so that the quantity V^2/P becomes [36]

$$\frac{V^2}{P} = 2.9\,\frac{R}{Q}\frac{f}{\Delta f}\,L \tag{A.12}$$

at the edges of the usable frequency band. The optimum length of one travelling-wave guide for which the phase slip at the edges of the band accumulates to $\pm\tau_{opt}$ then follows from Eq. (A.8) to

$$l_{opt} = 2.34\frac{v_g}{\pi\Delta f}. \tag{A.13}$$

Any desired length can be chosen by adjusting the group velocity of the TWS. A small number of longer guides is preferable over a large number of shorter guides due to the individual power sources, feeder lines and loads. In the case of a synchrotron the maximum length is limited by the length of the straight sections of the accelerator ring. However, the group velocity influences also other important parameters like the series impedance and the filling time. Following Eq. (A.7), the power required to obtain a given accelerating field E(z) is inverse-proportional to v_g, which should therefore be chosen as small as possible. The filling time of a TWS is

$$t_f = \frac{L}{v_g}. \tag{A.14}$$

As an example we consider the TWS used in the SPS with 44 cells and an active length of roughly 16.1 m. The group velocity at center frequency is $0.0946\,c$ resulting in a filling time of $0.567\mu s$.

The revolution period in the SPS with a circumference of 6912 km is roughly 23 μs for the ultra-relativistic case. The fact that the filling time is only a fraction of the revolution period means that the RF system can be operated in pulsed mode despite the fact that the common type of beam is composed of several hundreds of bunches. Furthermore, this means that the beam loading of the fundamental accelerating passband is of transient type (opposed to steady state).

We can relate the optimum physical length of the guide to its attenuation length by using Eqs. (A.5) and (A.13) as done in [36] and obtain

$$\frac{l_{opt}}{l_0} = 4.68 \, \frac{f}{Q\Delta f}. \tag{A.15}$$

A typical normal-conducting accelerating structure operated at 200 MHz has a quality factor of around 20000. If as an example the relative frequency swing of 0.44 % required for acceleration in the SPS (see Eq. (3.2), injection at 10 GeV) is used then $l_{opt} \approx 0.053 \, l_0$. This means that in practice the guide length is very small compared to the attenuation length and that therefore the structure itself can assumed to be lossless or equivalently that the accelerating field is constant along the structure.

B. Equivalent Circuit and Dispersion Relation for Multi-Stem Drift Tube Structures

A waveguide which is periodically loaded by stems behaves as an array of coupled circuits. The coupling is of resonant type, as the stems are resonant elements that create an associated passband. The circuit in Fig. 1.11 can therefore serve as a basis to describe the behaviour of such a structure. We modify the circuit as shown in Fig. B.1 to also include the mutual couplings that occur in the actual structure. Figure B.1 shows two cells of the periodic structure and each cell includes

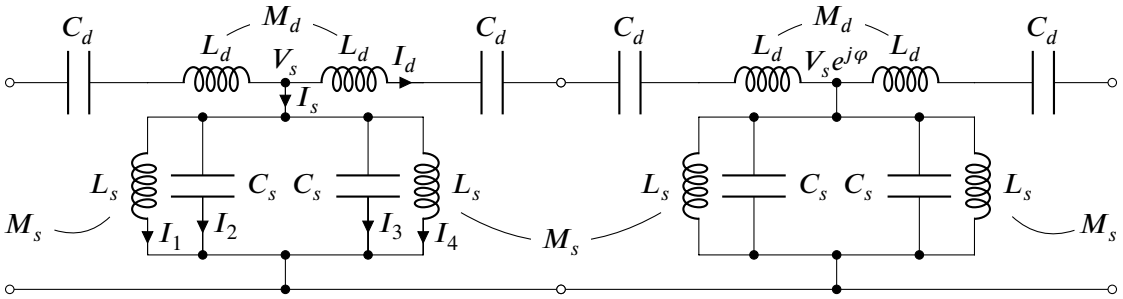

Figure B.1.: Equivalent circuit for multi-stem drift tube structure.

two resonators. The drift tube resonator consists of the series capacitance $C_d/2$, representing the gap capacity between drift tubes, and the inductance $2L_d$, representing the magnetic energy stored around the drift tubes and the gap. The shunt inductors L_s model the stem inductances, e.g. the inductance of one stem in the SPS parallel-stem structure. The capacitors C_s represent the capacitance between the drift tube and the outer cylinder. The resonant frequencies of the drift tube and stem resonators are $\omega_d = 1/\sqrt{L_d C_d}$ and $\omega_s = 1/\sqrt{L_s C_s}$ respectively. Some of the magnetic flux surrounding the stems will also couple to those of the adjacent cells. This inter-cell coupling is modelled by the mutual inductance M_s. A single drift tube is modelled by two separate inductors in successive cells, see Fig. B.1. In the actual structure these inductances share the same core, which is why the mutual inductance M_d needs to be included to properly model the EM behaviour of the structure.

To derive the dispersion relation of this circuit, we assume a lossless structure as well as the steady state and use Kirchhoff's circuit laws and Floquet's theorem. Let V_s be the potential on the centre of the left drift tube in Fig. B.1 with respect to the outer cylinder. The current I_s is flowing

via the stems to the outer cylinder and the current I_d through the drift tubes and the gaps. We know from Floquet's theorem that all currents and voltages are simply multiplied by the factor $e^{j\varphi}$ when moving down the structure by one cell, cf. Eq. (1.6). For further current notations see Fig. B.1. Let us derive the dispersion equation with $M_d = 0$ at first, as this mutual inductance can be easily added to the relation later on. We set up the equations

$$V_s\left(1 - e^{j\varphi}\right) = 2I_d\left(j\omega L_d + \frac{1}{j\omega C_d}\right) \tag{B.1}$$

$$V_s = j\omega L_s I_1 + j\omega M_s I_4 e^{-j\varphi} \tag{B.2}$$

$$= j\omega L_s I_4 + j\omega M_s I_1 e^{j\varphi} \tag{B.3}$$

$$= \frac{1}{j\omega C_s} I_2 = \frac{1}{j\omega C_s} I_3 \tag{B.4}$$

$$I_s = I_d\left(e^{-j\varphi} - 1\right) \tag{B.5}$$

$$I_s = \sum_{i=1}^{4} I_i\,. \tag{B.6}$$

From Eqs. (B.5) and (B.6) we get

$$I_d\left(e^{-j\varphi} - 1\right) = j\frac{2C_s}{\omega} V_s\left[\omega^2 - \frac{\omega_s^2}{1 - k_s^2}(1 - k_s\cos\varphi)\right], \tag{B.7}$$

when introducing the typical definition of coupling factor $k_s = {}^{M_s}/_{L_s}$. We rearrange and set into Eq. (B.1) to eliminate I_d and V_s

$$(1 - \cos\varphi) = \frac{2L_d}{L_s}\frac{1}{\omega^2\omega_s^2}\left(\omega^2 - \frac{\omega_s^2}{1 - k_s^2}\left(1 - k_s\cos\varphi\right)\right)(\omega^2 - \omega_d^2)\,. \tag{B.8}$$

Adding the mutual inductance M_d to this relation is easy, as merely the additional term $\omega M_d \cos\varphi$ must be added to the right hand side of Eq. (B.1). After minor adjustments, the full dispersion equation for the equivalent circuit in Fig. B.1 reads

$$\boxed{\sin^2\frac{\varphi}{2} = \frac{L_d}{L_s}\left(\frac{\omega^2}{\omega_s^2} - \frac{1 - k_s\cos\varphi}{1 - k_s^2}\right)\left(1 - \frac{\omega_d^2}{\omega^2} + k_d\cos\varphi\right)}, \tag{B.9}$$

with

$$\omega_d = \frac{1}{\sqrt{L_d C_d}} \qquad \omega_s = \frac{1}{\sqrt{L_s C_s}} \qquad k_d = \frac{M_d}{L_d} \qquad k_s = \frac{M_s}{L_s}\,. \tag{B.10}$$

The dispersion equation has two solutions corresponding to the TS_{11}- and TM_{01}-passbands and with φ=0 we find their 0-mode frequencies as

$$\omega_{d,0} = \frac{\omega_d}{\sqrt{1 + k_d}} \qquad \omega_{s,0} = \frac{\omega_s}{\sqrt{1 + k_s}}\,. \tag{B.11}$$

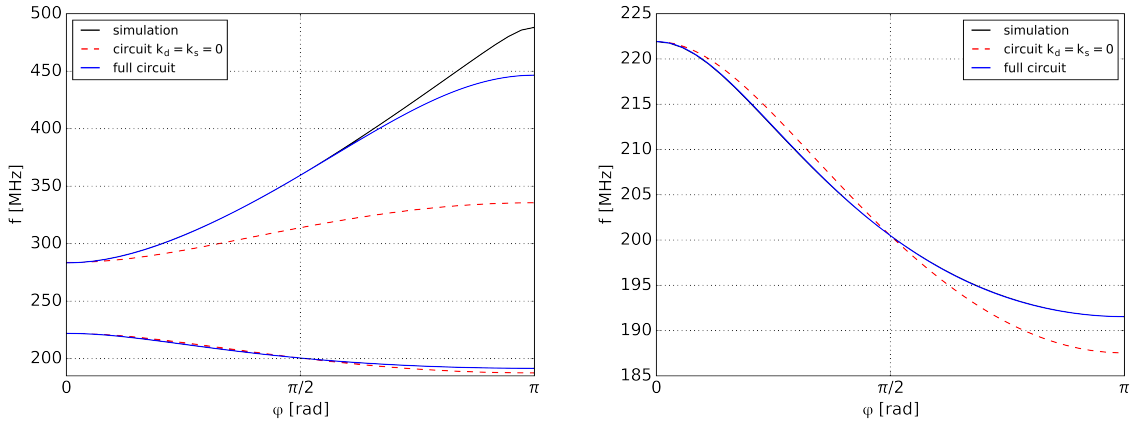

(a) TS_{11}- and TM_{01}-passbands.

(b) TS_{11}-passband (zoom).

Figure B.2.: The TS_{11}- and TM_{01}-passbands of the SPS 200 MHz TWS modelled by the equivalent circuit in Fig. B.1.

The parameters of the dispersion equation can e.g. be obtained by requiring that the two curves pass through a number of selected phase-frequency pairs obtained from simulation or measurement. Figure B.2 shows a comparison between the simulated and calculated dispersion curves. For the case that both mutual couplings are zero we have $\omega_{d,0} = \omega_d$ and $\omega_{s,0} = \omega_s$ and we use three phase-frequency pairs to calculate three unknown parameters of the dispersion equation (we are only interested in the ratio $r = {}^{L_d}/_{L_s}$). The two 0-modes and the ${}^{\pi}/_{2}$-mode of the stem-band were used in this case. In the case of the full circuit model, the 0- and ${}^{\pi}/_{2}$-modes of both passbands were used in addition to the π-mode of the stem-band to determine five parameters of the dispersion equation. The agreement between simulation and equivalent circuit for the stem-band is excellent in the case with mutual couplings, see Fig. B.2b.

C. Electromagnetic Field Profiles of Modes of Interest

EM characteristics and field profiles obtained with CST are reported here for the analysis in Section 3.4.3.

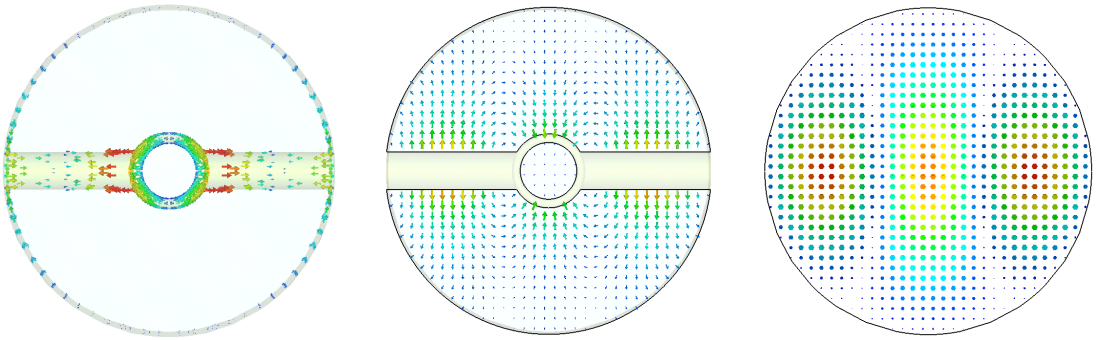

(a) Surface currents of 0-mode. (b) E-field of 0-mode in stem-plane. (c) E-field of π-mode in gap-plane.

Figure C.1.: EM characteristics of the TS_{31}-passband in the TWS **without pedestals**. Color-coding of field-strength is on a linear scale.

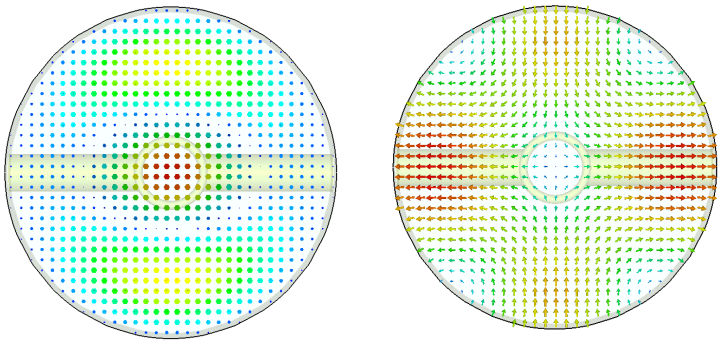

(a) E-field of 0-mode in gap-plane (TM-type).

(b) E-field of π-mode in gap-plane (TE-type).

Figure C.2.: EM characteristics of the upper HOM-band in Fig. 3.16 in the TWS **without pedestals**. Color-coding of field-strength is on a linear scale.

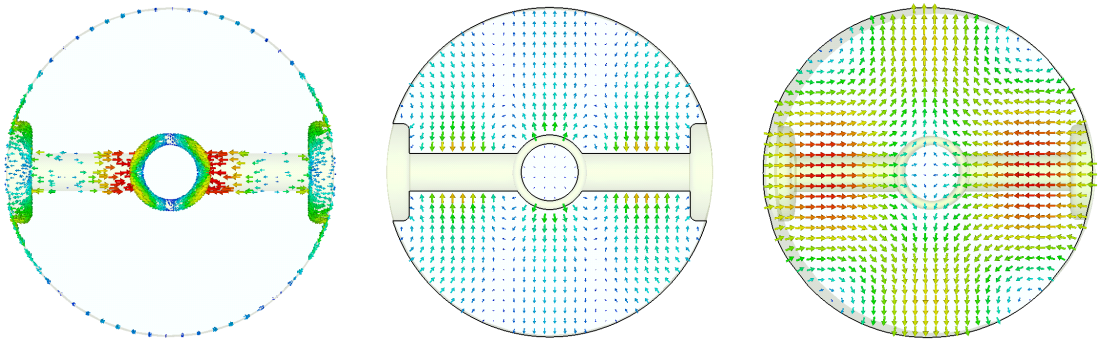

(a) Surface currents of 0-mode.

(b) E-field of 0-mode in stem-plane ($TS_{31,0}$-mode).

(c) E-field of π-mode in gap-plane (TE-type).

Figure C.3.: EM characteristics of the lower HOM-band in Fig. 3.16 in the full TWS. Color-coding of field-strength is on a linear scale.

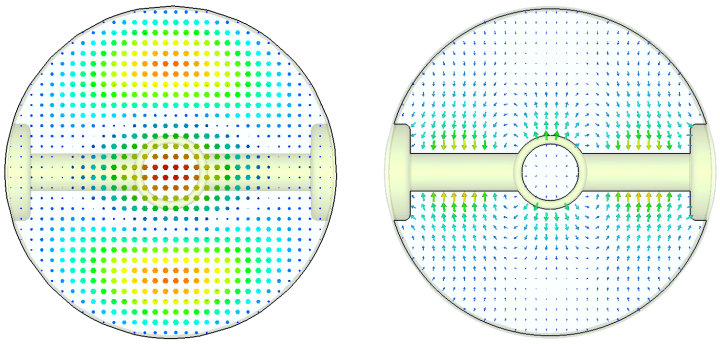

(a) E-field of 0-mode in gap-plane (TM-type).

(b) E-field of π-mode in stem-plane ($TS_{31,\pi}$-mode).

Figure C.4.: EM characteristics of the upper HOM-band in Fig. 3.16 in the full TWS. Color-coding of field-strength is on a linear scale.

D. Performance of 25 Ω-Equivalent Complex Impedance Loads on 44-Cells

Two 4-section TWSs were in use before LS 2 and they will remain in the machine after the LIU upgrade. In a 44-cell configuration, the most deteriorating HOMs in the 630 MHz frequency range are as well of the TS_{31}-type and they also have a very similar phase advance per cell compared to those in 33-cells. The complex loads can therefore immediately be deployed on the 4-section structures as well. Figure D.1 shows the damping performance of the 25 Ω-equivalent complex impedance loads on the pre-LS 2 44-cell TWS 2 configuration which included also six 938 MHz transverse HOM couplers. The complex loads are deployed on the 16 TS_{31}-couplers of the pre-

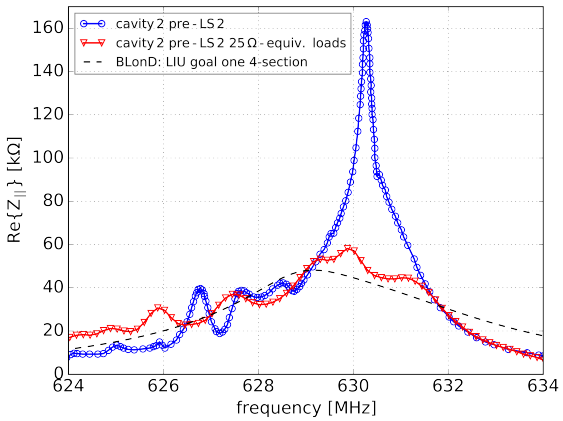

Figure D.1.: Damping performance of the 25 Ω-equivalent complex loads on the pre-LS 2 44-cell TWS 2 configuration.

LS 2 longitudinal damping configuration shown in Fig. 3.26b for the 33-cells. Additional couplers were not yet placed in the simulation model. Still, the improved damping due to the complex loads is excellent and the LIU goal can almost be reached by the complex loads alone. This would avoid further detuning of the accelerating mode due to additional HOM mitigation devices.

E. Temperature Distribution in the SPS TWS for an Input Power of 1.6 MW

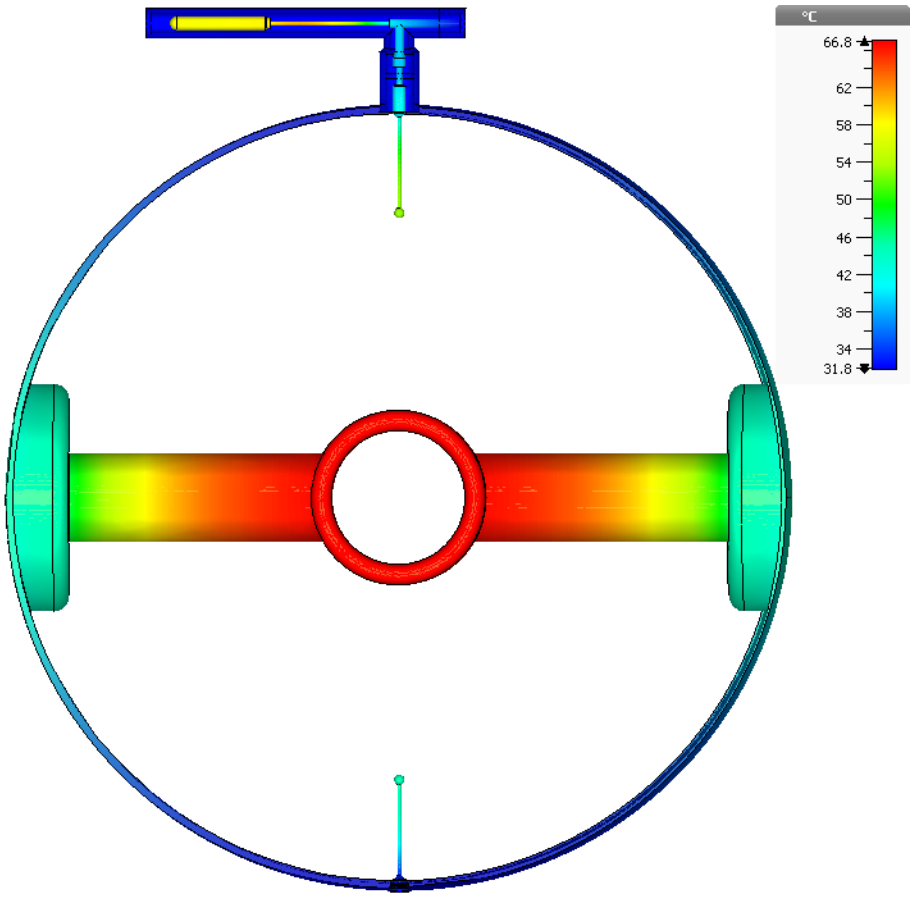

Figure E.1.: Simulated, steady state temperature distribution in the SPS TWS for a travelling wave in the TS_{11} $\pi/2$-mode with a continuous input power of 1.6 MW. The simulation setup is detailed in Fig. 4.30. Cooling pipes in the stems and on the cavity cylinder are not taken into account.

The temperature distribution on the SPS 200 MHz TWS as well as on the 630 MHz HOM-coupler and on the resonant post for the post-LS 2 input power into 44-cell structures is shown in Fig. E.1. For a travelling wave with a continuous power flow of 1.6 MW, the scaling factor for the losses in the eigenmode simulation is 0.0211, refer to Eq. (4.10). Most notably, the peak temperature on the

resonant post is 45°C, on the HOM coupler pickup 54°C and on parts of the 200 MHz rejection filter up to 62°C. Note that for the LHC type beam in the SPS the maximum input power of 1.6 MW is required merely for small fractions of the revolution period and the acceleration cycle. As the peak temperature on the post stays significantly below the empirical limit of 80°C (refer back to Section 4.5.1 and [63]), the heating of the resonant posts is still considered acceptable even for this large input power.

Bibliography

[1] M. Barnier, M. Calmy-Rey, H. Curien, and R. Aymar. *Infinitely CERN: memories of fifty years of research. 1954-2004*. Sciences et histoire. Hurter, Geneva, 2004.

[2] K. Wille. *The Physics of Particle Accelerators: An Introduction*. Oxford University Press, 2000.

[3] R. Wideröe. *Über ein neues Prinzip zur Herstellung hoher Spannungen*. PhD thesis, Techn. Hochsch. Aachen, Aachen, 1928.

[4] F. Gerigk. Cavity types. (arXiv:1111.4897):23 p, Nov 2011. Comments: presented at the CERN Accelerator School CAS 2010: RF for accelerators, Ebeltoft, 8-17 June 2010; CERN-2011-007, pp. 277-298.

[5] L. W. Alvarez. The design of a proton linear accelerator. *Phys. Rev.*, 70:799–800, July 1946.

[6] F. Grespan, G. De Michele, F. Gerigk, and S. Ramberger. Linac4 DTL Prototype: Theoretical Model, Simulation and Low Energy Measurements. (sLHC-PROJECT-Report-0028. CERN-sLHC-PROJECT-Report-0028):4 p, May 2009.

[7] D. A. Swenson, E. A. Knapp, J. M. Potter, and E. J. Schneider. Stabilization of the drift tube linac by operation in the pi/2 cavity mode. In *Proceedings, 6th International Conference on High-Energy Accelerators*, Sept 1967.

[8] J. D. Jackson. *Classical electrodynamics*. Wiley, New York, NY, 2 edition, 1975.

[9] C. A. Balanis. *Advanced Engineering Electromagnetics*. Wiley, 1989.

[10] J. C. Slater. *Microwave Electronics*. D. van Nostrand Company, New York City, 1950.

[11] G. Floquet. Sur les équations différentielles linéaires à coefficients périodiques. *Ann. Ecole Normale Sup. Palaiseau*, 12:47–82, 1883.

[12] K. Zhang and L. Dejie. *Electromagnetic Theory for Microwave and Optoelectronics*. Springer-Verlag, 2nd edition, 2008.

[13] T. P. Wangler. *RF Linear Accelerators*. Wiley-VCH, 2nd edition, 2008.

[14] G. Dôme and I. White. A general theory of multistem drift tube structures proposed for proton linacs. (CERN-ISR-300-LI-67-62. ISR-300-LI-67-62):11, Nov 1967.

[15] W. Hillert. *Transverse Linear Beam Dynamics*. CERN Accelerator School, Constanta, Romania, Sept 2018.

[16] A. W. Chao, K. H. Mess, M. Tigner, and F. Zimmermann. *Handbook of Accelerator Physics and Engineering*. World Scientific, 2nd edition, 2013.

[17] G. Apollinari, I. Béjar Alonso, O. Brüning, P. Fessia, M. Lamont, L. Rossi, and L. Tavian. *High-Luminosity Large Hadron Collider (HL-LHC): Technical Design Report V. 0.1*. CERN Yellow Reports: Monographs. CERN, Geneva, 2017.

[18] H. Damerau, A. Funken, R. Garoby, S. Gilardoni, B. Goddard, K. Hanke, A. Lombardi, D. Manglunki, M. Meddahi, B. Mikulec, G. Rumolo, E. Shaposhnikova, M. Vretenar, and J. Coupard. LHC Injectors Upgrade, Technical Design Report, Vol. I: Protons. Technical Report CERN-ACC-2014-0337, Dec 2014.

[19] A. Lasheen. *Beam Measurements of the Longitudinal Impedance of the CERN Super Proton Synchrotron*. CERN-THESIS-2017-068, Mar 2017.

[20] E. Shaposhnikova et al. Removing Known SPS Intensity Limitations for High Luminosity LHC Goals. (CERN-ACC-2016-289):MOPOY058. 3 p, 2016.

[21] E. Shaposhnikova, E. Ciapala, and E. Montesinos. Upgrade of the 200 MHZ RF System in the CERN SPS. (CERN-ATS-2011-042), Aug 2011.

[22] M. Montesinos. CERN LIU-SPS 200 MHz RF Upgrade SSPA Amplifiers, June 2016.

[23] J. Repond. *Possible mitigations of longitudinal intensity limitations for HL-LHC beam in the CERN SPS*. CERN-THESIS, 2019.

[24] CERN Beam Longitudinal Dynamics code BLonD. http://blond.web.cern.ch.

[25] C. Vollinger. Overview on the impedance Reduction in View of LIU-SPS Project. URL: `https://indico.cern.ch/event/714284/contributions/2935028/attachments/1620533/2578062/CVollinger_LIU_SPS_21Mar2018.pdf`, 3 2018.

[26] D. Boussard, T. Linnecar, and A. Millich. Damping of longitudinal instability at high energy. Technical Report CERN-SPS-COMMISSIONING-REPORT-20, CERN, Geneva, Aug 1976.

[27] G. Dôme. The SPS acceleration system travelling wave drift-tube structure for the CERN SPS. *CERN-SPS-ARF-77-11*, May 1977.

[28] F. Caspers and M. Wendt. JUAS 2017 RF Engineering course, 2017.

[29] B. W. Zotter and S. A. Kheifets. *Impedances and Wakes in High-Energy Particle Accelerators*. World Scientific, 1998.

[30] S. Heifets, A. Wagner, and B. Zotter. Generalized Impedances and Wakes in Asymmetric Structures. *SLAC/AP110*, January 1998.

[31] ACE3P. Advanced Computational Electromagnetic Simulation Suite 3D Parallel. URL: `https://portal.slac.Stanford.edu/sites/ard{_}public/acd/`.

[32] P. B. Wilson. Transient Beam Loading in Electron-Positron Storage Rings. *CERN-ISR-TH/78-23*, Oct 1978.

[33] E. Argence and T. Kahan. *Theory of Waveguides and Cavity Resonators*. Hart Publishing Company, New York City, 1967.

[34] D. Boussard. Beam loading. (CERN-1987-003-V-2.626), Sept 1985.

[35] D. Boussard. Travelling-Wave Structures. In *Proceedings of Joint US-CERN-Japan Accelerator School on Frontiers of Accelerator Technology*, pages 322–338, Sept. 1996.

[36] *The design study of a 300 GeV proton synchrotron*. CERN, Geneva, 1964. French version available.

[37] W. Schnell. An RF system for a 300 GeV proton synchrotron with mechanically tuned cavities. (CERN-AR-Int-SG-63-19):4 p, 1963.

[38] D. E. Nagle, E. A. Knapp, and B. C. Knapp. Coupled resonator model for standing wave accelerator tanks. *Review of Scientific Instruments*, 38(11):1583–1587, 1967.

[39] W. Schnell. A wide band travelling wave accelerating method for a 300 GeV proton synchrotron. (CERN-AR-Int-SG-65-16):4 p, 1965.

[40] P. Baudrenghien and G. A. Lambert. Reducing the impedance of the travelling wave cavities: feed-forward and one turn delay feed-back. 2000.

[41] F. Caspers and G. Dôme. The 938 MHz resonant damping loops for the 200 MHz SPS travelling wave cavities. Aug 2012. reprint.

[42] Computer Simulation Technology (CST) AG. Darmstadt, Germany. URL: `http://www.cst.com/`.

[43] Parallel stem structure prototype for installation in the Proton Synchrotron (PS). CERN drawings 8021-1049-0 and 8021-1065-0.

[44] P. Kramer and C. Vollinger. Studies for the SPS Travelling Wave Cavities Upgrade. In *CERN Yellow Reports: Conference Proceedings* [79], pages 57–62.

[45] G. Dôme. RF systems: waveguides and cavities. *AIP Conf. Proc.*, 153(CERN-SPS-86-24-ARF):1296. 116 p, Nov 1986.

[46] R. M. Jones, C. E. Adolphsen, J. W. Wang, and Z. Li. Wakefield damping in a pair of X-band accelerators for linear colliders. *Phys. Rev. ST Accel. Beams*, 9:102001, 2006.

[47] A. Corstanje et. al. The effect of the atmospheric refractive index on the radio signal of extensive air showers. *Astropart. Phys.*, 89:23–29, 2017.

[48] J. R. Davis, editor. *ASM International Metals Handbook*. ASM International, 2nd edition, 1998.

[49] D. M. Pozar. *Microwave engineering*. Wiley, Hoboken, NJ, 4th edition, 2012.

[50] R. E. Collin. *Foundations for microwave engineering*. McGraw-Hill series in electrical engineering. McGraw-Hill, New York, NY, 2nd edition, 1992.

[51] J. M. Jin. *Finite Element Method in Electromagnetics*. Wiley, New York, 1993.

[52] K. S. Kunz and R. J. Luebbers. *Finite Difference Time Domain Method for Electromagnetics*. FL: CRC Press. Boca Raton, 1993.

[53] National Energy Research Scientific Computing Center (NERSC), a U.S. Department of Energy Office of Science User Facility operated under Contract No. DE-AC02-05CH11231. URL: `https://www.nersc.gov/`.

[54] A. Candel, A. Kabel, L. Lee, Z. Li, G. Ng, G. Schussman, and K. Ko. State of the art in electromagnetic modeling for the Compact Linear Collider. In *Proc. J. Phys.*, 180 012004, 2009.

[55] J. B. Schneider. Understanding the Finite-Difference Time-Domain Method. Technical report, www.eecs.wsu.edu/%7Eschneidj/ufdtd, 2010.

[56] M. Schwarz. Effect of the 915MHz HOM on multi-batch stability. URL: `https://indico.cern.ch/event/839348/`, 8 2019.

[57] J. Repond and E. Shaposhnikova. Effect of HOM Frequency Shift on Bunch Train Stability. In *CERN Yellow Reports: Conference Proceedings* [79], pages 93–97.

[58] P. Kramer and C. Vollinger. Improved HOM-mitigation for future SPS 33-Cell 200 MHz traveling-wave accelerating structures. *International Journal of Modern Physics A*, 34(36), 2019.

[59] E. Haebel. Couplers for cavities. In *CAS, CERN Accelerator School, Superconductivity in Particle Accelerators*, number CERN 96-03, pages 231–264, 1996.

[60] O. Zinke and H. Brunswig. *Hochfrequenztechnik 1*. Springer-Verlag, 6th edition, 2000.

[61] F. E. Terman. *Radio engineer's handbook*. McGraw-Hill, New York, NY, 1943.

[62] W. Schminke. Strong damping of single-cell accelerator cavities by resonant loops. Technical Report SPS/ARF/WS/gs/81-68, CERN, Geneva, 1981.

[63] E. Montesinos. private communication.

[64] S. Ramberger and M. R. Khalvati. The DTL post coupler - An ingenious invention turns 50. *28th Linear Accelerator Conference*, 2017.

[65] W. D. Kilpatrick. Criterion for vacuum sparking designed to include both rf and dc. *Rev. Sci. Instrum.*, 28:824–826, 1957.

[66] T. J. Jr. Boyd. Kilpatrick's Criterion. *Los Alamos Group AT-1 report AT-1:82-28*, 1982.

[67] L. C. Maier and J. C. Slater. Field strength measurements in resonant cavities. *Journal of Applied Physics*, 23(1):68–77, 1952.

[68] E. L Ginzton. *Microwave measurements*. International series in pure and applied physics. McGraw-Hill, New York, NY, 1957.

[69] C. Steele. A Nonresonant Perturbation Theory. 1964.

[70] F. Caspers and G. Dôme. Precise perturbation measurements of resonant cavities and higher order mode identification. Technical Report CERN-SPS-85-46-ARF, CERN, Geneva, Nov 1985.

[71] H. Hahn and H. J. Halama. Perturbation Measurement of Transverse R/Q in Iris-Loaded Waveguides. *IEEE Transactions on Microwave Theory and Techniques*, 16(1):20–29, Jan. 1968.

[72] C. Elliott, V. Vijayakumar, W. Zink, and R. Hansen. National Instruments LabVIEW: A Programming Environment for Laboratory Automation and Measurement. *JALA: Journal of the Association for Laboratory Automation*, 12(1):17–24, 2007.

[73] P. H. Smith. An Improved Transmission Line Calculator. *Electronics*, 12(1):29–31, 1939.

[74] P. Kramer, A. Farricker, and C. Vollinger. Verification by RF Measurements of New HOM Mitigation Scheme Developed for Future SPS 33-Cell Accelerating Structures. In *Proc. 10th International Particle Accelerator Conference (IPAC'19), Melbourne, Australia, 19-24 May 2019*, number 10 in International Particle Accelerator Conference, pages 274–276, Geneva, Switzerland, Jun. 2019. JACoW Publishing. https://doi.org/10.18429/JACoW-IPAC2019-MOPGW076.

[75] D. Boussard. Possible ways of improving the longitudinal behaviour of the high intensity beam at injection in the SPS. Technical Report SPS-ARF-Technical-Report-DB-gs-81-2. CERN-SPS-ARF-81-2, CERN, Geneva, Jan 1981.

[76] P. Kramer. Impact of HOM-couplers on pi/2-mode tuning and accelerating voltage. URL: `https://indico.cern.ch/event/781287/contributions/3251878/attachments/1778919/3120301/20181217_tuning_meas.pdf`, 12 2018.

[77] J. Repond and E. Shaposhnikova. Effect on beam stability of 200 MHz voltage reduction. URL: `https://indico.cern.ch/event/788200/`, 1 2019.

[78] M. Schwarz. Effect of 200 MHz TWC frequency shift on instabilities. URL: `https://indico.cern.ch/event/808003/`, 3 2019.

[79] CERN, Geneva. *Proceedings of the ICFA Mini-Workshop on Impedances and Beam Instabilities*, volume 1/2018 of *CERN-2018-003-CP*, Benevento, Italy.

[80] P. Kramer and C. Vollinger. Measurement of rf voltage in long traveling wave accelerating structures with application to the CERN Super Proton Synchrotron. *Physical Review Accelerators and Beams*, 22:101002, Oct 2019.

[81] B. Salvant, D. Amorim, S. Antipov, S. Arsenyev, M. Beck, N. Biancacci, O. Brüning, J. E. Campelo, E. Carideo, F. Caspers, T. Dalascu, A. Farricker, A. Grudiev, T. Kaltenbacher, E. Koukovini-Platia, P. Kramer, A. Lasheen, M. Migliorati, N. Mounet, E. Métral, R. Nagaoka, N. Nasr Esfahani, S. Persichelli, B. Popovic, T. Rijoff, G. Rumolo, E. Shaposhnikova, V. Smaluk, B. Spataro, V. Vaccaro, C. Vollinger, N. Wang, S. White, C. Zannini, and B. Zotter. Building the impedance model of a real machine. page WEYPLS1. 6 p, 2019.

[82] P. Kramer and C. Vollinger. HOM-Mitigation for Future SPS 33-Cell 200 MHz Accelerating Structures. In *Proc. 13th International Computational Accelerator Physics Conference (ICAP'18), Key West, FL, USA, 20-24 Oct 2018*, number 13 in International Computational

Accelerator Physics Conference, pages 35–41, Geneva, Switzerland, Jan. 2019. JACoW Publishing. https://doi.org/10.18429/JACoW-ICAP2018-SAPAG04.

[83] A. Farricker, P. Kramer, B. Popovic, E. Sunar, C. Vollinger, and M. Wendt. Identification of Imperfections in Impedance Shields on the SPS-QF Flanges via Non-Intrusive Measurements. (CERN-ACC-2018-179):THPAF063. 4 p, 2018.

[84] N. Nasresfahani, P. Kramer, and C. Vollinger. Equivalent circuit modelling of travelling wave accelerating structures and its applications. In *2017 47th European Microwave Conference (EuMC)*, pages 572–575, Oct 2017.

[85] C. Vollinger, A. Farricker, T. R. Kaltenbacher, P. Kramer, and B. K. Popovic. Needs and Solutions for Machine Impedance Reduction. In *CERN Yellow Reports: Conference Proceedings* [79], pages 125–131.

[86] C. Vollinger, T. R. Kaltenbacher, and P. Kramer. Measurement Report for the PS-booster Wire Scanner. (CERN-ACC-NOTE-2017-0022), Mar 2017.

[87] P. Kramer, J. Varela Campelo, F. Caspers, C. Vollinger, and E. Montesinos. In situ Measurements of the SPS 200 MHz Accelerating Cavity III. (CERN-ACC-NOTE-2015-0021), Aug 2015.

List of author's publications

1. P. Kramer and C. Vollinger. Measurement of rf voltage in long traveling wave accelerating structures with application to the CERN Super Proton Synchrotron. *Physical Review Accelerators and Beams*, 22:101002, Oct 2019.

2. P. Kramer, A. Farricker, and C. Vollinger. Verification by RF Measurements of New HOM Mitigation Scheme Developed for Future SPS 33-Cell Accelerating Structures. In *Proc. 10th International Particle Accelerator Conference (IPAC'19), Melbourne, Australia, 19-24 May 2019*, number 10 in International Particle Accelerator Conference, pages 274–276, Geneva, Switzerland, Jun. 2019. JACoW Publishing. https://doi.org/10.18429/JACoW-IPAC2019-MOPGW076.

3. B. Salvant, D. Amorim, S. Antipov, S. Arsenyev, M. Beck, N. Biancacci, O. Brüning, J. E. Campelo, E. Carideo, F. Caspers, T. Dalascu, A. Farricker, A. Grudiev, T. Kaltenbacher, E. Koukovini-Platia, P. Kramer, A. Lasheen, M. Migliorati, N. Mounet, E. Métral, R. Nagaoka, N. Nasr Esfahani, S. Persichelli, B. Popovic, T. Rijoff, G. Rumolo, E. Shaposhnikova, V. Smaluk, B. Spataro, V. Vaccaro, C. Vollinger, N. Wang, S. White, C. Zannini, and B. Zotter. Building the impedance model of a real machine. page WEYPLS1. 6 p, 2019.

4. P. Kramer and C. Vollinger. Improved HOM-mitigation for future SPS 33-Cell 200 MHz traveling-wave accelerating structures. *International Journal of Modern Physics A*, 34(36), 2019.

5. P. Kramer and C. Vollinger. HOM-Mitigation for Future SPS 33-Cell 200 MHz Accelerating Structures. In *Proc. 13th International Computational Accelerator Physics Conference (ICAP'18), Key West, FL, USA, 20-24 Oct 2018*, number 13 in International Computational Accelerator Physics Conference, pages 35–41, Geneva, Switzerland, Jan. 2019. JACoW Publishing. https://doi.org/10.18429/JACoW-ICAP2018-SAPAG04.

6. A. Farricker, P. Kramer, B. Popovic, E. Sunar, C. Vollinger, and M. Wendt. Identification of Imperfections in Impedance Shields on the SPS-QF Flanges via Non-Intrusive Measurements. (CERN-ACC-2018-179):THPAF063. 4 p, 2018.

7. N. Nasresfahani, P. Kramer, and C. Vollinger. Equivalent circuit modelling of travelling wave accelerating structures and its applications. In *2017 47th European Microwave Conference (EuMC)*, pages 572–575, Oct 2017.

8. C. Vollinger, A. Farricker, T. R. Kaltenbacher, P. Kramer, and B. K. Popovic. Needs and Solutions for Machine Impedance Reduction. In *CERN Yellow Reports: Conference Proceedings* [79], pages 125–131.

9. P. Kramer and C. Vollinger. Studies for the SPS Travelling Wave Cavities Upgrade. In *CERN Yellow Reports: Conference Proceedings* [79], pages 57–62.

10. C. Vollinger, T. R. Kaltenbacher, and P. Kramer. Measurement Report for the PS-booster Wire Scanner. (CERN-ACC-NOTE-2017-0022), Mar 2017.

11. P. Kramer, J. Varela Campelo, F. Caspers, C. Vollinger, and E. Montesinos. In situ Measurements of the SPS 200 MHz Accelerating Cavity III. (CERN-ACC-NOTE-2015-0021), Aug 2015.